UNIVERSIDADE DE SÃO PAULO
Instituto de Ciências Matemáticas e de Computação

Enhanced multiscale mixed methods for two-phase flows in high-contrast porous media

Franciane Fracalossi Rocha

Tese de Doutorado do Programa de Pós-Graduação em Ciências de Computação e Matemática Computacional (PPG-CCMC)

ICMC USP SÃO CARLOS

Franciane Fracalossi Rocha

Enhanced multiscale mixed methods for two-phase flows in high-contrast porous media

Thesis submitted to the Institute of Mathematics and Computer Sciences – ICMC-USP – in accordance with the requirements of the Computer and Mathematical Sciences Graduate Program, for the degree of Doctor in Science. *FINAL VERSION*

Concentration Area: Computer Science and Computational Mathematics

Advisor: Prof. Dr. Fabricio Simeoni de Sousa
Co-advisor: Prof. Dr. Luis Felipe Feres Pereira

USP – São Carlos
September 2020

Ficha catalográfica elaborada pela Biblioteca Prof. Achille Bassi
e Seção Técnica de Informática, ICMC/USP,
com os dados inseridos pelo(a) autor(a)

R672e

Rocha, Franciane Fracalossi
Enhanced multiscale mixed methods for two-phase flows in high-contrast porous media / Franciane Fracalossi Rocha; orientador Fabricio S. Sousa; coorientador Felipe Pereira. -- São Carlos, 2020.
150 p.

Tese (Doutorado - Programa de Pós-Graduação em Ciências de Computação e Matemática Computacional) -- Instituto de Ciências Matemáticas e de Computação, Universidade de São Paulo, 2020.

1. Multiscale mixed methods. 2. Two-phase flows. 3. High-contrast porous media. 4. Multiscale Robin Coupled Method . 5. Reservoir simulation. I. Sousa, Fabricio S., orient. II. Pereira, Felipe, coorient. III. Título.

Bibliotecários responsáveis pela estrutura de catalogação da publicação de acordo com a AACR2:
Gláucia Maria Saia Cristianini - CRB - 8/4938
Juliana de Souza Moraes - CRB - 8/6176

Franciane Fracalossi Rocha

Métodos mistos multiescala aprimorados para escoamentos bifásicos em meios porosos de alto contraste

Tese apresentada ao Instituto de Ciências Matemáticas e de Computação – ICMC-USP, como parte dos requisitos para obtenção do título de Doutora em Ciências – Ciências de Computação e Matemática Computacional. *VERSÃO REVISADA*

Área de Concentração: Ciências de Computação e Matemática Computacional

Orientador: Prof. Dr. Fabricio Simeoni de Sousa
Coorientador: Prof. Dr. Luis Felipe Feres Pereira

USP – São Carlos
Setembro de 2020

To my parents.

ACKNOWLEDGEMENTS

Agradeço ao Programa de Pós-Graduação em Ciências de Computação e Matemática Computacional do ICMC/USP pela oportunidade do desenvolvimento deste trabalho e pela excelente formação. Agradeço ao Departamento de Ciências Matemáticas da Universidade do Texas em Dallas (UT-Dallas) pela oportunidade de realização do estágio no exterior, que muito contribuiu para minha formação. Agradeço ao apoio do Centro de Ciências Matemáticas Aplicadas à Industria (CEPID-CeMEAI, financiado pela FAPESP proc. 2013/07375-0). O presente trabalho foi realizado com apoio financeiro da Petrobras (código de financiamento 2015/00400-4) e da Coordenação de Aperfeiçoamento de Pessoal de Nível Superior (CAPES, código de financiamento 001).

Agradeço ao meu orientador Prof. Fabricio S. de Sousa por aceitar me orientar e por conduzir minha formação acadêmica com empenho e dedicação, sempre buscando as melhores oportunidades para o desenvolvimento deste projeto e confiando no meu trabalho. Agradeço ao meu co-orientador Prof. Felipe Pereira por supervisionar meu estágio no exterior, oferecendo todo o suporte necessário para a realização do mesmo, além de compartilhar o seu conhecimento e experiência na pesquisa científica com muita paciência e disponibilidade. Agradeço aos professores do grupo de pesquisa Prof. Gustavo C. Buscaglia e Prof. Roberto F. Ausas por contribuírem durante todo o desenvolvimento deste projeto. A oportunidade de trabalhar neste grupo de pesquisa em colaboração com os professores Fabricio S. de Sousa, Felipe Pereira, Gustavo C. Buscaglia e Roberto F. Ausas foi uma experiência muito gratificante e fundamental para o meu desenvolvimento como pesquisadora. Todos os conselhos, sugestões e dicas valiosas foram de grande importância. Agradeço também aos colegas do grupo de pesquisa, em especial ao Rafael T. Guiraldello por fornecer o código do MRCM e por me auxiliar no entendimento do método. Agradeço aos colegas do Laboratório de Matemática Aplicada e Computação Científica (LMACC/USP) por proporcionarem um agradável ambiente de trabalho.

Agradeço a todos os meus amigos que de alguma maneira contribuíram para o desenvolvimento deste trabalho. Agradeço à toda minha família pelo apoio incondicional, especialmente ao meu querido pai Ademar Rocha por sempre me motivar. Registro também o agradecimento à minha mãe Eneide, que infelizmente não está presente em vida neste momento, mas que sempre confiou na minha capacidade e me ensinou a nunca desistir dos meus sonhos. Por fim, agradeço ao meu noivo Mateus A. Mendes pelo companheirismo, incentivo e suporte incrível durante todo esse período. Sem ele nada disso seria possível.

“I am a great believer in luck.
The harder I work, the more of it I seem to have.”
(Coleman Cox)

RESUMO

ROCHA, F. F. **Métodos mistos multiescala aprimorados para escoamentos bifásicos em meios porosos de alto contraste**. 2020. 150 p. Tese (Doutorado em Ciências – Ciências de Computação e Matemática Computacional) – Instituto de Ciências Matemáticas e de Computação, Universidade de São Paulo, São Carlos – SP, 2020.

Esta tese propõe novos métodos para a solução numérica de escoamentos bifásicos em meios porosos de alto contraste, típicos em reservatórios de petróleo. Utiliza-se uma técnica de segregação de operadores, onde a saturação de uma das fases e o campo de velocidades são atualizados sequencialmente. Nosso objetivo é aproximar o campo de velocidades através de métodos multiescala, permitindo que a solução global seja calculada em malhas grosseiras (escala grossa), enquanto funções de base detalhadas são definidas localmente (geralmente em paralelo) em uma malha mais fina (escala fina). Os métodos aqui desenvolvidos são baseados no *Multiscale Robin Coupled Method (MRCM)*, um método de decomposição de domínio que generaliza outros métodos mistos multiescala da literatura e adiciona grande flexibilidade à escolha dos espaços de interface e às condições de contorno do acoplamento das soluções locais. Identificamos que o acoplamento de subdomínios através da imposição de uma pressão contínua (respectivamente, fluxos normais) é a melhor estratégia em termos de precisão para escoamentos bifásicos na presença de canais (resp., regiões) de alta (resp., baixa) permeabilidade. Assim, introduzimos uma técnica adaptativa para definir o parâmetro algorítmico de Robin do MRCM, que controla a importância relativa das condições de contorno de Dirichlet e Neumann no acoplamento dos subdomínios. A nova estratégia apresenta soluções precisas em campos de permeabilidade desafiadores. Essa técnica é então utilizada para melhorar a precisão do MRCM, considerando escolhas alternativas para os espaços de interface que não sejam os clássicos polinômios, uma vez que esses não são adequados para representar estruturas de alto contraste como canais de alta permeabilidade e barreiras (baixa permeabilidade). Introduzimos novos espaços de interface, baseados na física, para lidar com campos de permeabilidade contendo simultaneamente canais altamente permeáveis e barreiras, acomodadas respectivamente, pelos espaços de pressão e fluxo. Mostramos que os espaços de interface propostos produzem soluções significativamente mais precisas do que espaços polinomiais para problemas com coeficientes de permeabilidade de alto contraste. Diferentes técnicas para aprimorar a solução de escoamentos bifásicos em termos de eficiência computacional são estudadas. Formulamos o *Multiscale Perturbation Method for Two-Phase Flows (MPM-2P)* para acelerar a solução de escoamentos bifásicos. Neste contexto, apresentamos um método de segregação de operadores modificado, onde reutilizamos funções de base calculadas pelo MRCM em um tempo anterior da simulação ao invés de calcular atualizações completas das soluções locais. Mostramos que o MPM-2P reduz drasticamente o custo computacional das simulações de escoamentos bifásicos, sem apresentar perdas de precisão. O MRCM também foi estudado em um esquema sequencial implícito

para escoamentos bifásicos, que possibilita passos de tempo arbitrariamente grandes quando comparado à métodos explícitos no tempo, melhorando a eficiência da simulação. Mostramos que o MRCM produz aproximações precisas e robustas quando combinado com diferentes esquemas para leis de conservação hiperbólicas, incluindo técnicas implícitas. Nossas simulações de escoamentos bifásicos mostram que o MRCM apresenta uma precisão sem precedentes para problemas realistas quando comparado com alguns métodos multiescala da literatura. Além disso, o MRCM pode tirar proveito de supercomputadores de última geração para simular eficientemente escoamentos bifásicos em meios porosos de alto contraste.

Palavras-chave: Métodos mistos multiescala, Escoamentos bifásicos, Meios porosos de alto contraste, Multiscale Robin Coupled Method, Simulação de reservatórios.

ABSTRACT

ROCHA, F. F. **Enhanced multiscale mixed methods for two-phase flows in high-contrast porous media**. 2020. 150 p. Tese (Doutorado em Ciências – Ciências de Computação e Matemática Computacional) – Instituto de Ciências Matemáticas e de Computação, Universidade de São Paulo, São Carlos – SP, 2020.

This thesis proposes new methods for the numerical solution of two-phase flows in high-contrast porous media typical of petroleum reservoirs. An operator splitting strategy is used, where the saturation of one of the phases and the velocity field are updated sequentially. We focus on approximating the velocity field by multiscale methods, which allow for the global solution to be computed on coarse meshes (large scale), while detailed basis functions are defined locally (usually in parallel) in a much finer grid (small scale). The methods developed here are based on the Multiscale Robin Coupled Method (MRCM), a domain decomposition method that generalizes other well-established multiscale mixed methods and adds great flexibility to the choice of interface spaces as well as in the boundary conditions for coupling of local solutions. We find that the coupling of nearest neighbor subdomains through the imposition of a continuous pressure (respectively, normal fluxes) is the best strategy in terms of accuracy to approximate two-phase flows in the presence of high (resp., low) permeability channels (resp., regions). Thus, we introduce a new adaptivity strategy for setting the Robin algorithmic parameter of the MRCM, that controls the relative importance of Dirichlet and Neumann boundary conditions in the coupling of subdomains. The new strategy presents accurate approximations in challenging, high-contrast permeability fields. Then, it is used to improve the accuracy of the MRCM by considering alternative choices for the interface spaces other than the classical polynomials since they are not optimal for high-contrast features such as high permeability channels and barriers (low permeability). We introduce new interface spaces, which are based on physics, to deal with permeability fields in the simultaneous presence of high permeability channels and barriers, accommodated respectively, by the pressure and flux spaces. We show that the proposed interface spaces produce solutions significantly more accurate than polynomial spaces for problems with high-contrast permeability coefficients. We investigate different techniques to enhance the approximation of two-phase flows in terms of computational efficiency. We formulate a new procedure, the Multiscale Perturbation Method for Two-Phase Flows (MPM-2P), to speed-up the solution of two-phase flows. A modified operator splitting method is presented, where we replace full updates of local solutions by reusing basis functions computed by the MRCM at an earlier time of the simulation. We show that the MPM-2P reduces drastically the computational cost of two-phase flow simulations, without loss of accuracy. The MRCM is also investigated in a sequential implicit scheme for two-phase flows, that allows for the use of arbitrarily large time steps when compared to explicit time integration methods, improving the efficiency of the simulation. We show that the MRCM produces accurate and robust approximations when

combined with different hyperbolic solvers, including implicit techniques. Our numerical simulations of two-phase flows with the MRCM present an unprecedented accuracy for realistic problems when compared to some standard multiscale methods. Moreover, the MRCM can take advantage of state-of-the-art supercomputers to efficiently simulate two-phase flows in high-contrast porous media.

Keywords: Multiscale mixed methods, Two-phase flows, High-contrast porous media, Multiscale Robin Coupled Method, Reservoir simulation.

LIST OF FIGURES

LIST OF CHARTS

LIST OF ALGORITHMS

LIST OF ABBREVIATIONS AND ACRONYMS

*a*MRCM	Adaptive MRCM
BFs	Basis Functions
CFL	Courant-Friedrichs-Lewy
DFM	Discrete Fracture Model
GMsFEM	Generalized Multiscale Finite Element Method
IMPES	Implicit Pressure Explicit Saturation
KT	Kurganov-Tadmor
MHM	Multiscale Hybrid-Mixed Finite Element Method
MMMFEM	Multiscale Mortar Mixed Finite Element Method
MPM	Multiscale Perturbation Method
MPM-2P	Multiscale Perturbation Method for Two-Phase Flows
MRCM	Multiscale Robin Coupled Method
MRST	MATLAB Reservoir Simulation Toolbox
MsFEM	Multiscale Finite Element Method
MSFV	Multiscale Finite Volume Method
MsMFEM	Multiscale Mixed Finite Element Method
MuMM	Multiscale Mixed Method
PBS	Physics-Based Spaces
POL	Polynomial Spaces
PVI	Pore Volume Injected
REVs	Representative Elementary Volumes
SFI	Sequential Fully Implicit
SI	Sequential Implicit

CONTENTS

CHAPTER

1

INTRODUCTION

Petroleum reservoirs are sedimentary rock formations that contain several void spaces between their mineral grains. The void spaces establish interconnected pore networks that can store and transmit fluids derived from hydrocarbons, as oil (AZIZ; SETTARI, 1979).

Techniques to displace the oil towards production wells are usually applied to extract it from the reservoirs (EWING, 1983; LIE, 2019). The natural type of oil recover, referred to *primary recovery*, consists of the displacement of the oil by drilling through the naturally pressurized reservoir. However, this process can leave a significant amount of oil into the reservoir. The called *secondary recovery* is used to recover part of the remaining oil through the injection of a fluid (typically water) into injection wells while oil is produced through production wells. Nevertheless, some oil is left into the reservoir even with this strategy. In order to recover more of the residual oil, *tertiary recovery* techniques, that involve chemical and thermal effects are considered. These techniques aim to make the oil flow more readily, for example through the injection of solvent, gases, or other chemical species to mix with the oil, the injection of polymers to increase the water viscosity, and the use of thermal effects to reduce the oil viscosity. The different recovery methods are considered by several computational models for multiphase flows in porous media to estimate production aspects (CHEN; HUAN; MA, 2006; LIE, 2019).

The simulation models of petroleum reservoirs deal with highly heterogeneous permeability fields with multiple scales and high-contrast. The representation of the solution must capture the heterogeneity of the porous medium. Depending on the level of details required and the size of the problem, the reservoir characterization can lead to a model with several billion cells and thousands of time steps, making the numerical simulations extremely expensive (CHEN; HUAN; MA, 2006).

The multiscale methods have been introduced to exploit the multiscale structure of the problem and provide efficient approximations at a reduced computational cost by decomposing large computational tasks in a family of smaller problems. They allow the global solution to be

computed in coarse meshes (large scale), while detailed basis functions are produced locally in a much finer grid (small scale). The local problems can be solved simultaneously in state-of-the-art parallel machines making possible the simulation of huge problems as opposed to traditional simulation techniques developed for serial calculations that cannot handle effectively problems of the same magnitude. These methods have received considerable attention from several groups. See (KIPPE; AARNES; LIE, 2008) for a very comprehensive comparison of procedures of this type.

Typical models for multiphase flows in porous media include an elliptic equation for pressure and velocity coupled with a hyperbolic conservation law for the saturation transport problem (PEACEMAN, 2000; EWING, 1983). Several multiscale methods have been proposed to approximate the velocity fields whereas different schemes have been used for the transport equation. In this thesis, we investigate the simulation of two-phase (oil-water) flows using multiscale methods for the elliptic equation and finite volume schemes to approximate the transport problem.

In section 1.1, we present a literature review on the multiscale methods related to the one that we investigate, namely the Multiscale Robin Coupled Method (GUIRALDELLO *et al.*, 2018). Then, in section 1.2 we show how the thesis is organized.

1.1 Multiscale methods

The past years have seen remarkable advances in the multiscale methods research for modeling of flows in heterogeneous porous media. Multiscale methods have been developed in the framework of finite volume (JENNY; LEE; TCHELEPI, 2003; JENNY; LEE; TCHELEPI, 2005; WANG; HAJIBEYGI; TCHELEPI, 2016; CORTINOVIS; JENNY, 2017), finite element (HOU; WU, 1997; AARNES; HOU, 2002; EFENDIEV; GALVIS; HOU, 2013), and mixed finite element methods (CHEN; HOU, 2003; AARNES, 2006; ARBOGAST *et al.*, 2007a; HARDER; PAREDES; VALENTIN, 2013; FRANCISCO *et al.*, 2014; CHUNG; EFENDIEV; LEE, 2015). Many applications to two-phase flows can be found, for example, in (EFENDIEV *et al.*, 2006; AARNES; KROGSTAD; LIE, 2006; GANIS *et al.*, 2014c; MØYNER; LIE, 2016; PRESHO; GALVIS, 2016; DURÁN *et al.*, 2020) and references therein. The coupling of the multiscale flow and transport problem has already been treated by operator splitting techniques (DOUGLAS; FURTADO; PEREIRA, 1997; FURTADO *et al.*, 2011; PRESHO; HILL, 2020) and implicit formulations (JENNY; LEE; TCHELEPI, 2006; JIANG; TCHELEPI, 2019; GANIS *et al.*, 2014c).

In this thesis, we focus on approximating two-phase flows using multiscale mixed finite element methods. A literature review on this class of multiscale methods can be found in subsection 1.1.1 followed by subsection 1.1.2, where we recall the main features of the multiscale method that we are interested in.

1.1.1 Developments on multiscale mixed finite element methods applied to flows in heterogeneous porous media

To show the advances in the multiscale mixed finite element methods research area we present a list of the articles that apply them to flows in porous media. The articles can be classified into the following five groups according to the multiscale procedure:

1. Multiscale Mixed Finite Element Method (MsMFEM);
2. Multiscale Mortar Mixed Finite Element Method (MMMFEM);
3. Multiscale Hybrid-Mixed Finite Element Method (MHM);
4. Multiscale mixed methods based on Robin interface conditions: the Multiscale Mixed Method (MuMM) and the Multiscale Robin Coupled Method (MRCM);
5. Mixed Generalized Multiscale Finite Element Method (mixed-GMsFEM).

A summary of each group is given below.

The Multiscale Finite Element Method (MsFEM) (HOU; WU, 1997) and the Multiscale Mixed Finite Element Method (MsMFEM) (CHEN; HOU, 2003) were developed for solving second order elliptic equations with oscillating coefficients. However, the original MsFEM is not mass conservative, and the MsMFEM produces a globally (but not necessarily locally) mass conservative velocity field. To deal with this issue a modified MsMFEM that produces a velocity field (globally and locally mass conservative) was proposed (AARNES, 2004). The modified MsMFEM was later combined with streamline methods (AARNES; KIPPE; LIE, 2005); extended to nonuniform, unstructured coarse grids (AARNES; KROGSTAD; LIE, 2006); and used in adaptive simulations (AARNES; EFENDIEV, 2006). Another extension of the MsMFEM considers the corner-point grid geometry using a mimetic discretization (AARNES; KROGSTAD; LIE, 2008), which was also applied in unstructured grids (AARNES; EFENDIEV, 2008b) and used as a basis for the development of an adaptive local-global method (ALPAK; PAL; LIE, 2012). The MsMFEM was applied to a coupled wellbore-reservoir flow model (KROGSTAD; DURLOFSKY, 2007); three-phase black oil problems (KROGSTAD *et al.*, 2009); and compressible flows (KROGSTAD, 2011; KROGSTAD; LIE; SKAFLESTAD, 2012). It was considered in an adjoint formulation that uses coarse-grid mappings for the optimization of waterflooding computations (KROGSTAD; HAUGE; GULBRANSEN, 2011), and also used to speed up the computations within multilevel Monte Carlo techniques (EFENDIEV; ILIEV; KRONSBEIN, 2013). Another mixed framework for the MsMFEM that uses limited global information from the heterogeneities was presented by (AARNES; EFENDIEV; JIANG, 2008) and (AARNES *et al.*, 2010), the last for unstructured grids. The MsMFEM is also closely related to the sub-grid upscaling techniques (ARBOGAST; BOYD, 2006; JIANG; EFENDIEV; MISHEV, 2010; ARBOGAST, 2011). In (JIANG; EFENDIEV; MISHEV, 2010), for example,

the authors investigate the use of the approximated global information by computing a partial upscaling. More improvements for the MsMFEM include the development of the expanded MsMFEM (JIANG; COPELAND; MOULTON, 2012); the extension to a coarse grid with subdivided faces (LIE *et al.*, 2014); and the dynamically adaptive computation of fluid transport equations in highly heterogeneous porous media (ZHANG *et al.*, 2017). Other studies on the MsMFEM comprise the validation for two-phase flows in challenging and geologically realistic corner-point grids (PAL *et al.*, 2015); its performance investigation in parallel simulations of two-phase flows (PUSCAS; ENCHÉRY; DESROZIERS, 2018); some numerical tests using the MATLAB Reservoir Simulation Toolbox (MRST) (ABDULLAH *et al.*, 2019); and the simulation of gas flow in shale porous media (ZHANG *et al.*, 2020).

Next, we present a classification of the articles concerning the type of flow (single-phase or multiphase/black-oil) and porous medium (low-contrast, high-contrast, and fractured). The difference between the articles that are classified for a medium of low or high-contrast considers only if this information was highlighted by the authors in the articles. It means that the objective of applying the method for highly heterogeneous media was pointed out by the authors in the articles of the high-contrast group, while no mention of it was made in the articles of the low-contrast category.

Chart 1 – Classification of the articles related to the MsMFEM.

Flow	Medium	Articles
Single-phase	Low-contrast	(ARBOGAST; BOYD, 2006)
	High-contrast	(ARBOGAST, 2011; LIE *et al.*, 2014)
	Fractured	(ZHANG *et al.*, 2020)
Multi-phase or black-oil	Low-contrast	(AARNES, 2004; AARNES; KIPPE; LIE, 2005; AARNES; EFENDIEV, 2006; KROGSTAD; DURLOFSKY, 2007; AARNES; EFENDIEV, 2008b; AARNES; EFENDIEV; JIANG, 2008; KROGSTAD *et al.*, 2009; JIANG; EFENDIEV; MISHEV, 2010; KROGSTAD; HAUGE; GULBRANSEN, 2011; EFENDIEV; ILIEV; KRONSBEIN, 2013; PUSCAS; ENCHÉRY; DESROZIERS, 2018; ABDULLAH *et al.*, 2019)
	High-contrast	(CHEN; HOU, 2003; AARNES; KROGSTAD; LIE, 2006; AARNES; KROGSTAD; LIE, 2008; AARNES *et al.*, 2010; KROGSTAD, 2011; ALPAK; PAL; LIE, 2012; KROGSTAD; LIE; SKAFLESTAD, 2012; JIANG; COPELAND; MOULTON, 2012; PAL *et al.*, 2015; ZHANG *et al.*, 2017)

Source: Research data.

The Multiscale Mortar Mixed Finite Element Method (MMMFEM) (ARBOGAST *et al.*, 2007b) was introduced as a more flexible formulation to the existing multiscale finite element

methods. This approach imposes the continuity of the flux via a mortar finite element space on a coarse grid scale. A computationally efficient implementation for the method was proposed by defining a multiscale flux basis (GANIS; YOTOV, 2009). The MMMFEM was applied to slightly compressible Darcy flows (KIM *et al.*, 2007), and combined with the multipoint flux mixed finite element method (WHEELER; XUE; YOTOV, 2012). The framework of the MMMFEM was considered in (GANIS *et al.*, 2012) to introduce an approach for preconditioning systems arising in multiphase flows, where a global nonlinear interface problem was solved. A linearization of the global system in both subdomain and interface variables simultaneously to yield a single Newton iteration was addressed to the single-phase slightly compressible flows model (GANIS *et al.*, 2014a). Then, the algorithm was extended to fully-implicit two-phase flows in three dimensions considering a porous medium with capillarity, gravity, and compressibility (GANIS *et al.*, 2014c). Afterward, an efficient parallel two-stage preconditioner using the linear system obtained as a result of the global approach was proposed (GANIS *et al.*, 2014b). The multiscale mixed finite element space based on homogenization theory to avoid the problems with anisotropy (ARBOGAST, 2011) was adapted to a multiscale mortar space that incorporates local information from homogenization (ARBOGAST; XIAO, 2013). These spaces were firstly tested with a formally first order mortar space and then a formally second-order mortar space was considered (ARBOGAST; TAO; XIAO, 2013). Other developments on the MMMFEM include a general framework for a posteriori error estimation in the multiscale, multinumerics, and mortar coupling (PENCHEVA *et al.*, 2013); a flux basis algorithm developed for the Stokes–Darcy flow problems (GANIS *et al.*, 2017); the unique solvability and optimal convergence error for nonlinear elliptic problems, besides the prove of quadratic convergence for the Newton's method to solve the nonlinear algebraic system (ARSHAD; PARK; SHIN, 2018); a local-global mortar multiscale space with basis functions that can capture global information (FU; CHUNG, 2019); and the multiscale mortar expanded mixed method (ARSHAD; PARK, 2020). In Chart 2 we show the classification of the articles related to the MMMFEM.

The Multiscale Hybrid-Mixed Finite Element Method (MHM) for solving the Darcy equation was presented by (HARDER; PAREDES; VALENTIN, 2013). This method relaxes the continuity of the pressure to a coarse grid while assuring the strong continuity of the normal component of flux in a fine grid. An analysis of the MHM was presented (ARAYA *et al.*, 2013), providing both a priori and a posteriori error estimates and the proof of existence and uniqueness of a solution. An important extension of the procedure was presented in (HARDER; PAREDES; VALENTIN, 2015), where the authors consider the reaction-advection-diffusion equation. Then, a more general form of the method was explored in (MADUREIRA, 2015), where a connection between a dual hybrid formulation and the multiscale finite element methods was presented. An abstract setting for the construction and analysis of the MHM with emphasis on the general properties of the approximations generated by solving the local problems approximately was added in (HARDER; VALENTIN, 2016). The uniform convergence of the MHM for elliptic problems with rough periodic coefficients was also addressed (PAREDES; VALENTIN;

Chart 2 – Classification of the articles related to the MMMFEM.

Flow	Medium	Articles
Single-phase	Low-contrast	(KIM *et al.*, 2007; GANIS; YOTOV, 2009; ARBOGAST; XIAO, 2013; PENCHEVA *et al.*, 2013; GANIS *et al.*, 2014a; ARSHAD; PARK; SHIN, 2018; ARSHAD; PARK, 2020)
	High-contrast	(WHEELER; XUE; YOTOV, 2012; ARBOGAST; TAO; XIAO, 2013)
	Fractured	(GANIS *et al.*, 2017)
Multi-phase or black-oil	Low-contrast	(ARBOGAST *et al.*, 2007b)
	High-contrast	(GANIS *et al.*, 2012; GANIS *et al.*, 2014b; GANIS *et al.*, 2014c; FU; CHUNG, 2019)

Source: Research data.

VERSIEUX, 2017). High-performance computing simulations considering different simulator prototypes have been explored to evaluate the MHM (GOMES *et al.*, 2017). Recently, a variant for the MHM that considers a full mixed formulation was developed (DURÁN *et al.*, 2019). In the new formulation, mixed finite elements were considered at the local problems stage, instead of continuous finite elements as used in the previous works. The MHM was also combined with discrete fracture models by (DEVLOO; TENG; ZHANG, 2019). More extensions of the MHM formulation include the Stokes and Brinkman equations (ARAYA *et al.*, 2017); general non-conforming polygonal meshes (BARRENECHEA *et al.*, 2020); and the two-phase flows problem (DURÁN *et al.*, 2020). We remark that the MHM has also been used in other types of applications as the Maxwell equations, Helmholtz equation, and linear elasticity models. In Chart 3 we present the classification of the cited articles.

Multiscale mixed methods based on Robin interface conditions have received considerable attention. We mention the Multiscale Mixed Method (MuMM) (FRANCISCO *et al.*, 2014), which was developed to approximate the solution of elliptic problems with high contrast in their coefficients. The MuMM is based on a nonoverlapping iterative domain decomposition for mixed finite elements (DOUGLAS *et al.*, 1993). This procedure has been a basis for some improvements on multiscale methods. For example, a recursive formulation to replace multiscale global interface problems by linear combinations of the local subdomain solutions (AKBARI *et al.*, 2019), and the development of the Multiscale Perturbation Method (MPM) (ALSADIG *et al.*, 2020), a novel procedure to speed-up the parallel numerical solution of multiphase flow problems. A new multiscale method based on the MuMM has been introduced: the Multiscale Robin Coupled Method (MRCM) (GUIRALDELLO *et al.*, 2018). The MRCM generalizes the MMMFEM and MHM, which are the extreme cases for the Robin boundary conditions of subdomain coupling.

Chart 3 – Classification of the articles related to the MHM.

Flow	Medium	Articles
Single-phase	Low-contrast	(PAREDES; VALENTIN; VERSIEUX, 2017; MADUREIRA, 2015; DURÁN *et al.*, 2019)
	High-contrast	(HARDER; PAREDES; VALENTIN, 2013; ARAYA *et al.*, 2013; HARDER; PAREDES; VALENTIN, 2015; HARDER; VALENTIN, 2016; GOMES *et al.*, 2017; ARAYA *et al.*, 2017; BARRENECHEA *et al.*, 2020)
	Fractured	(DEVLOO; TENG; ZHANG, 2019)
Multi-phase or black-oil	Low-contrast	(DURÁN *et al.*, 2020)

Source: Research data.

This method adds great flexibility to the choice of independent spaces on the skeleton of the decomposition, corresponding to interface pressures and fluxes. In (GUIRALDELLO *et al.*, 2019) two types of interface spaces for the MRCM were compared: piecewise polynomial spaces and informed spaces, the latter obtained from sets of snapshots by dimensionality reduction. In (GUIRALDELLO *et al.*, 2020), the MRCM was used to assess the applicability of new post-processing procedures to recover local conservation of velocity fields produced by multiscale approximations. Later, the MRCM was extended to the approximation of two-phase flows in highly heterogeneous porous media (ROCHA *et al.*, 2020b), where a concept of adaptivity for the procedure was introduced. The most recent development is the introduction of physics-based interface spaces for multiscale mixed methods (ROCHA *et al.*, 2020a). A classification of the articles concerning multiscale mixed methods based on Robin interface conditions can be found in Chart 4.

Chart 4 – Classification of the articles concerning multiscale mixed methods based on Robin interface conditions.

Flow	Medium	Articles
Single-phase	High-contrast	(FRANCISCO *et al.*, 2014; GUIRALDELLO *et al.*, 2018; GUIRALDELLO *et al.*, 2019; AKBARI *et al.*, 2019; GUIRALDELLO *et al.*, 2020; ALSADIG *et al.*, 2020)
Multi-phase or black-oil	High-contrast	(ROCHA *et al.*, 2020b)
	Fractured	(ROCHA *et al.*, 2020a)

Source: Research data.

The Generalized Multiscale Finite Element Method (GMsFEM) (EFENDIEV; GALVIS; HOU, 2013) is another approach based on finite element methods that has been extended to the mixed context (CHUNG; EFENDIEV; LEE, 2015). The main idea of the GMsFEM is to divide the computation into an offline stage to construct a snapshot space and an online stage for computing the multiscale functions based on a spectral decomposition of the offline space. Adaptive offline and online mixed strategies have been developed to construct the basis function spaces (CHAN; CHUNG; EFENDIEV, 2016; CHUNG; EFENDIEV; HOU, 2016). An enriched multiscale mortar space approach was obtained based on the constructions of local multiscale basis functions by following the framework of the GMsFEM (CHUNG; FU; YANG, 2016). Then, the GMsFEM was extended to the mortar mixed case (YANG; CHUNG; FU, 2018), where an online basis enrichment computed using residuals with the mortar mixed finite element method and oversampling technique was proposed. Extensions of the mixed GMsFEM to adaptive online techniques include basis enrichment considering oversampling (YANG; FU; CHUNG, 2020) and the constraint energy minimizing (CHUNG; PUN, 2019). The concept of energy minimizing snapshot was also investigated in (CALO *et al.*, 2016; CHUNG; EFENDIEV; LEUNG, 2018). Furthermore, this concept was used together with oversampling as a general strategy for constructing the multiscale basis functions (CHUNG; EFENDIEV; LEUNG, 2019). The mixed GMsFEM has been applied to perforated domains (CHUNG; LEUNG; VASILYEVA, 2016) and the black oil model problem (SINGH; LEUNG; WHEELER, 2019). Other developments include the construction of multiscale basis functions based on least-squares (CHEN; CHUNG; JIANG, 2016); the goal-oriented adaptivity with different error indicators (CHUNG; POLLOCK; PUN, 2017); a two-grid preconditioner with an adaptive coarse space for flow simulations in highly heterogeneous media (YANG; FU; CHUNG, 2019); an enrichment for pressure multiscale basis functions (CHEN *et al.*, 2019); an extension to the Darcy-Forchheimer model (SPIRIDONOV *et al.*, 2019); and an application to Bayesian inverse problem of multi-term time fractional diffusion models (SONG; JIANG; ZHENG, 2020). In Chart 5 we present a classification of the above referred articles.

There are multiscale mixed methods that are derived from the variational multiscale approach (HUGHES, 1995; HUGHES *et al.*, 1998), for example (NAKSHATRALA *et al.*, 2006; JUANES; DUB, 2008; LARSON; MÅLQVIST, 2009; MÅLQVIST, 2011). Other developments on multiscale mixed methods include a proposed approach based on a localized orthogonal decomposition of Raviart-Thomas finite element spaces (MÅLQVIST; PETERSEIM, 2014), and the use of multiscale mixed methods in domain decomposition preconditioners problems (XIE; XU, 2019). Several applications of the different multiscale mixed methods are available in the literature. The use of stochastic and random porous media, for example, can be found in (WHEELER; WILDEY; YOTOV, 2011; AMBARTSUMYAN *et al.*, 2019) for single-phase flows and (AARNES; EFENDIEV, 2008a; JIANG; MISHEV; LI, 2010; MA; ZABARAS, 2011; WEI *et al.*, 2014; JIANG; MOULTON; WEI, 2014; JIANG; LI, 2017) for the multiphase case. More applications to fractured reservoirs have been addressed by (GULBRANSEN; HAUGE;

Chart 5 – Classification of the articles related to the GMsFEM.

Flow	Medium	Articles
Single-phase	Low-contrast	(SONG; JIANG; ZHENG, 2020)
	High-contrast	(CALO *et al.*, 2016; CHAN; CHUNG; EFENDIEV, 2016; CHUNG; FU; YANG, 2016; CHUNG; LEUNG; VASILYEVA, 2016; CHEN; CHUNG; JIANG, 2016; CHUNG; POLLOCK; PUN, 2017; CHUNG; PUN, 2019; CHUNG; EFENDIEV; LEUNG, 2018; CHUNG; EFENDIEV; LEUNG, 2019; SPIRIDONOV *et al.*, 2019)
Multi-phase or black-oil	High-contrast	(CHUNG; EFENDIEV; LEE, 2015; YANG; CHUNG; FU, 2018; YANG; FU; CHUNG, 2020; SINGH; LEUNG; WHEELER, 2019; YANG; FU; CHUNG, 2019)
	Fractured	(CHUNG; EFENDIEV; HOU, 2016; CHEN *et al.*, 2019)

Source: Research data.

LIE, 2010; ZHANG *et al.*, 2016; SPIRIDONOV; VASILYEVA, 2018; AHMED; FUMAGALLI; BUDIŠA, 2019) (for single-phase flows) and (NATVIG *et al.*, 2011; ZHANG *et al.*, 2017) (for multiphase flows).

One can note that it is possible to find several applications of the multiscale mixed finite element methods. This class of methods provides significant advances in the modeling of multiphase flow and transport problems in heterogeneous porous media. Another review on multiscale mixed methods for Darcy flows can be found in (ARBOGAST, 2012).

1.1.2 The Multiscale Robin Coupled Method

We are interested on studying the Multiscale Robin Coupled Method (GUIRALDELLO *et al.*, 2018; GUIRALDELLO *et al.*, 2019), which is based on the domain decomposition described in (DOUGLAS *et al.*, 1993) and on the MuMM (FRANCISCO *et al.*, 2014). The MRCM formulation can take advantage of parallel computations with a computational cost comparable to existing procedures and producing more accurate solutions than some standard multiscale mixed methods.

Different strategies to the calculation of the basis functions are adopted by the distinct multiscale methods. The MRCM allows for the independent choice of the pressure and flux interface spaces through the imposition of Robin boundary conditions. It can be seen as a generalization of the MMMFEM (ARBOGAST *et al.*, 2007a; GANIS; YOTOV, 2009) and the MHM (HARDER; PAREDES; VALENTIN, 2013; ARAYA *et al.*, 2013), which consider respectively, pressure and flux interface spaces. We expect to take advantage of the flexibility of the MRCM to improve its accuracy on simulating two-phase flows.

The first study on the MRCM for two-phase flows (ROCHA *et al.*, 2020b) has shown that

its accuracy compared to other popular methods for single-phase flows is also observed for the two-phase case. In the referred work, we find that the coupling of adjacent subdomains through the imposition of continuous pressure is the best strategy to approximate two-phase flows in the presence of high permeability channels. On the other hand, the coupling of subdomains through the imposition of continuous normal components of fluxes is an adequate strategy to handle low permeability regions. Thus, we introduced an adaptivity strategy for setting the Robin algorithmic parameter of the MRCM according to the permeability variations. With this new strategy one can control the relative importance of Dirichlet and Neumann boundary conditions in the coupling of subdomains as a function of the permeability field.

Realistic oil reservoirs contain features as channels/fractures and barriers that are challenging for the multiscale simulation. It is well known that classic multiscale interface spaces as the polynomial are not optimal for the high contrast, channelized permeability fields (CHUNG; EFENDIEV; LI, 2014; CHUNG; FU; YANG, 2016; AARNES; KROGSTAD; LIE, 2006; MØYNER; LIE, 2016; CORTINOVIS; JENNY, 2017; GUIRALDELLO *et al.*, 2019). We investigate alternative choices for the interface spaces of the MRCM based on the geometry of the heterogeneities, especially when they are relatively large as happens in fractured karst reservoirs (BAOMIN; JINGJIANG, 2009; POPOV *et al.*, 2009; HUANG; YAO; WANG, 2013; LOPES *et al.*, 2019). We proposed new interface spaces to capture the large scale features of the channelized structures (ROCHA *et al.*, 2020a). The pressure space is designed to accommodate channels whereas the flux space is built to accommodate barriers. The adaptivity of the MRCM is used to automatically select the appropriate parameters at each location.

In order to enhance the approximation of two-phase flows we introduce a new procedure, the Multiscale Perturbation Method for Two-Phase Flows (MPM-2P), which combines the MRCM with the recently proposed Multiscale Perturbation Method (MPM) (ALSADIG *et al.*, 2020). The MPM is a procedure based on classical perturbation theory that has been developed to speed-up the parallel (multi-core) numerical solution of multiphase flow problems. In (ALSADIG *et al.*, 2020), the MPM was used to approximate the velocity field by reusing multiscale basis functions computed for a distinct pressure equation (with different, but closely related coefficients), providing that the solutions of the two elliptic equations are associated. We formulate the MPM-2P, where we replace a full update of local solutions by reusing multiscale basis functions that are computed by the MRCM at an earlier time of the simulation. One can replace hundreds of fully updated multiscale solutions by inexpensive MPM-2P approximations without loss of accuracy.

In this thesis we consider finite volume schemes to approximate the transport of saturation. The MRCM can be combined with any hyperbolic solver. In most of our numerical experiments we use a classic operator splitting strategy (DOUGLAS; EWING; WHEELER, 1983; DOUGLAS; FURTADO; PEREIRA, 1997; DOUGLAS; PEREIRA; YEH, 2000), where the saturation (approximated by an explicit finite volume scheme) and the velocity are updated

sequentially. The use of implicit techniques is another possibility for the approximation of the transport problem. Thus, we propose to combine the MRCM with an implicit scheme, in a sequential fashion (WATTS, 1986). The new approach allows for the use of arbitrarily large time steps when compared to explicit time integration methods. Our numerical experiments show that the MRCM produces accurate and robust results for the simulation of two-phase flows when combined with different hyperbolic solvers.

1.2 Outline

This thesis is organized as follows:

- Chapter 2 introduces the problem of the two-phase flows. We present the governing equations and the numerical approximation, where we show the formulations of the methods that we consider.
- Chapter 3 presents the new adaptivity concept for the MRCM, as well as its numerical simulation results for two-phase flows.
- Chapter 4 describes the new interface spaces based on physics to deal with high-contrast channelized structures. We show how the physics-based interface spaces are built and present our numerical experiments for single and two-phase flows.
- Chapter 5 exhibits the formulation of the MPM-2P and the numerical tests performed.
- Chapter 6 details the sequential implicit solver and discusses the numerical results obtained by its combination with the MRCM for the approximation of two-phase flows.
- Chapter 7 summarizes the main results obtained and the plans for future work.
- Appendix A recalls the derivation of the equations for flows in porous media.

CHAPTER

2

TWO-PHASE FLOWS IN POROUS MEDIA

We consider a high-contrast heterogeneous oil reservoir through which an immiscible and incompressible two-phase flow of water and oil (denoted by w and o, respectively) takes place. The heterogeneity of the medium is represented by a space-dependent permeability coefficient in the elliptic model. This coefficient exhibits variations of many orders of magnitude over short distances, being a challenge for the numerical methods. In the next section we present the model problem for two-phase flows.

2.1 Mathematical setting

Our model consider that the reservoir contains injection wells, from which water is injected to displace the trapped oil towards production wells. The saturations of oil and water are related considering a fully saturated medium (the sum of both oil and water saturation is equal to one). Therefore the model considers only the water saturation in the transport problem.

The unknowns are the Darcy velocity $\mathbf{u}(\mathbf{x},t)$ and the fluid pressure $p(\mathbf{x},t)$, given by Darcy's law with a statement of conservation of mass

$$\begin{aligned} \mathbf{u} &= -\lambda(s)K(\mathbf{x})\nabla p && \text{in } \Omega \\ \nabla\cdot\mathbf{u} &= q && \text{in } \Omega \\ p &= g && \text{on } \partial\Omega_p \\ \mathbf{u}\cdot\mathbf{n} &= z && \text{on } \partial\Omega_u \end{aligned} \tag{2.1}$$

and the water saturation $s(\mathbf{x},t)$ given by the transport problem

$$\begin{aligned} \frac{\partial s}{\partial t} + \nabla\cdot(f(s)\mathbf{u}) &= 0 && \text{in } \Omega \\ s(\mathbf{x},t=0) &= s^0(\mathbf{x}) && \text{in } \Omega \\ s(\mathbf{x},t) &= \bar{s}(\mathbf{x},t) && \text{in } \partial\Omega^- \end{aligned} \tag{2.2}$$

where $\Omega \subset \mathbb{R}^d$, $d = 2$ or $d = 3$ is the computational domain; $K(\mathbf{x})$ is the symmetric, uniformly positive definite absolute permeability tensor; $q = q(\mathbf{x},t)$ is a source term; $g = g(\mathbf{x},t)$ is the

pressure condition specified at the boundary $\partial\Omega_p$; $z = z(\mathbf{x},t)$ is the normal velocity condition ($\mathbf{n}$ is the outward unit normal) specified at the boundary $\partial\Omega_u$; s^0 is the initial condition for the saturation and $\bar{s}$ is the saturation at the inlet boundaries $\partial\Omega^- = \{\mathbf{x} \in \partial\Omega,\ \mathbf{u}\cdot\mathbf{n} < 0\}$. The functions $\lambda(s)$ and $f(s)$ are respectively the total mobility and the fractional flow of water, given by

$$\lambda(s) = \lambda_w(s) + \lambda_o(s) = \frac{k_{rw}(s)}{\mu_w} + \frac{k_{ro}(s)}{\mu_o} \qquad \text{and} \qquad f(s) = \frac{\lambda_w(s)}{\lambda(s)}, \tag{2.3}$$

where $k_{rj}(s)$ and μ_j, $j \in \{w,o\}$, are respectively the relative permeability function and viscosity of phase j. For simplicity, the capillary pressure and gravity effects are not considered. Furthermore, we assume a constant porosity already scaled out by changing the time variable. We refer to the conductivity by $\kappa = \lambda(s(\mathbf{x}))K(\mathbf{x})$ for two-phase flows and $\kappa = K(\mathbf{x})$ for some examples on the single-phase flows context. More details about the fundamental equations for flows in porous media can be found in Appendix A.

Since both equations (2.1) and (2.2) are very different, it is natural to split their computation in time, taking advantage of the specific methods developed for each class of equations (DOUGLAS; EWING; WHEELER, 1983; DOUGLAS; FURTADO; PEREIRA, 1997; DOUGLAS; PEREIRA; YEH, 2000; COATS, 2000). We intend to combine the MRCM for the approximation of Darcy's velocity with finite volume methods to approximate the hyperbolic conservation law for the water saturation. Any hyperbolic solver can be combined with the MRCM. The numerical approximation used for the splitting is introduced in the next section. Then, the MRCM is presented in section 2.3, while the hyperbolic solvers considered in this thesis are discussed in section 2.4.

2.2 Numerical approximation

We consider a common operator splitting approach for solving the equations (2.1)-(2.2). Precisely, we solve (2.1) to compute $p(\mathbf{x},t)$ and $\mathbf{u}(\mathbf{x},t)$ and (2.2) for $s(\mathbf{x},t)$, sequentially (DOUGLAS; FURTADO; PEREIRA, 1997). This splitting procedure has the advantage of improving the computational efficiency, usually considering larger time steps for the pressure equation (2.1) compared to those used for the hyperbolic equation (2.2), where CFL-type condition is enforced to ensure numerical stability of explicit schemes (more details can be found in (DOUGLAS; EWING; WHEELER, 1983; DOUGLAS; FURTADO; PEREIRA, 1997; DOUGLAS; PEREIRA; YEH, 2000)).

Let Δt_s be the time step used in the discretization of the saturation equation, and let Δt_p be the time step for pressure (and velocity) updates. We set the relation $\Delta t_p = C\Delta t_s$, where C is a positive integer, assuming that Δt_s is constant (in practice we allow for variable Δt_s). Therefore, pressure and velocity are updated at times $t_n = n\Delta t_p$, for $n = 0,1,\ldots$, while the saturation is computed at intermediate times $t_{n,k} = t_n + k\Delta t_s$, for $k = 1,2,\ldots,C$, such that $t_n < t_{n,k} \leq t_{n+1}$.

Accuracy can be further improved by extrapolation of the last computed velocities for each time $t_{n,k}$ of the saturation transport time step. In that sense, the velocity field to be considered at time $t_{n,k}$ can be computed as

$$\mathbf{u}^e(\mathbf{x},t) = \begin{cases} \mathbf{u}^0(\mathbf{x}), & \text{if} \quad 0 \le t \le t_1, \\ \dfrac{t-t_{n-1}}{\Delta t_p}\,\mathbf{u}^n(\mathbf{x}) - \dfrac{t-t_n}{\Delta t_p}\,\mathbf{u}^{n-1}(\mathbf{x}), & \text{if} \quad t_n < t \le t_{n+1},\ n>0 \end{cases} \tag{2.4}$$

for each $t = t_{n,k}$, $k = 1,2,\ldots,C$, where $\mathbf{u}^n(\mathbf{x})$ is the velocity computed by the pressure equation (2.1) at time $t = t_n$, approximating $\mathbf{u}(\mathbf{x},t_n)$ (see (DOUGLAS; FURTADO; PEREIRA, 1997)). The algorithm to compute the approximate solutions for saturation, velocity and pressure at time t_{n+1} from the solutions at time t_n, is described in Algorithm 1.

Algorithm 1 – Solving equations (2.1)-(2.2) by operator splitting

1: Given $s^n(\mathbf{x})$, $p^n(\mathbf{x})$ and $\mathbf{u}^n(\mathbf{x})$ computed from previous time step
2: **for** $k \in \{1,\cdots,C\}$ **do**
3: $\quad t_{n,k} = t_n + k\Delta t_s$
4: $\quad$ Compute $\mathbf{u}^e(\mathbf{x},t_{n,k})$ from Eq. (2.4) ▷ The extrapolation step is optional
5: $\quad$ Solve Eq. (2.2) with $\mathbf{u} = \mathbf{u}^e$ to compute $s(\mathbf{x},t_{n,k})$ ▷ Using an explicit hyperbolic solver
6: **end for**
7: Given $s^{n+1}(\mathbf{x})$, update $\kappa = \lambda(s^{n+1}(\mathbf{x}))K(\mathbf{x})$
8: Solve Eq. (2.1) to obtain $p^{n+1}(\mathbf{x})$ and $\mathbf{u}^{n+1}(\mathbf{x})$ ▷ Using a multiscale method
9: Make $n \leftarrow n+1$ and return to step 1

2.3 Solving the elliptic equation by the MRCM

Considering the most up-to-date saturation $s^{n+1}(\mathbf{x})$, one can obtain the most recent conductivity $\kappa = \lambda(s^{n+1}(\mathbf{x}))K(\mathbf{x})$, which allows the solution of pressure equation in the whole domain Ω. From now onwards, for the sake of notation, we will drop the time dependency on these equations, keeping in mind that this dependency can only come from the source term, the boundary data (which is rather uncommon in most applications), and most importantly, from the conductivity.

The Multiscale Robin Coupled method is a non-overlapping multiscale domain decomposition method that generalizes the Multiscale Mixed Method (MuMM) (FRANCISCO *et al.*, 2014), which is based on a domain decomposition method that was first introduced by Douglas et al. (DOUGLAS *et al.*, 1993). The main idea of these methods is to subdivide the domain Ω in N non-overlapping subdomains Ω_i, $i = 1,2,\ldots,N$, such that local solutions can be computed independently for each Ω_i (which is naturally parallelizable) in a fine scale h, associated to the size of the discretization of the local problems. Continuity of the solution is enforced by compatibility conditions, that in the multiscale sense, are weakly imposed only on a coarse scale $H \gg h$ to reduce computational cost. Here H is the characteristic size of the subdomains. Let Γ be the skeleton of the decomposition, i.e., the union of all interfaces $\Gamma_{ij} = \Omega_i \cap \Omega_j$. This means

that the multiscale solution $(\mathbf{u}_h, p_h)$ obtained by the MRCM satisfies the compatibility conditions

$$\int_\Gamma (\mathbf{u}_h^+ - \mathbf{u}_h^-)\cdot \check{\mathbf{n}}\ \psi\ d\Gamma = 0 \quad \text{and} \quad \int_\Gamma (p_h^+ - p_h^-)\ \phi\ d\Gamma = 0 \tag{2.5}$$

for all $(\phi, \psi) \in \mathscr{U}_H \times \mathscr{P}_H$, which are low-dimensional spaces defined over the set of edges $\mathscr{E}_h$ of the skeleton Γ. The $+$ and $-$ superscripts denote the solution on each side of the interface Γ. In this equation we refer to a fixed (global) normal vector $\check{\mathbf{n}}$ to the skeleton Γ, pointing outwards from the subdomain with smallest index. One of the key ingredients of the MRCM is the definition of normal flux and pressure unknowns at the interfaces, namely $(U_H, P_H) \in \mathscr{U}_H \times \mathscr{P}_H$ such that these compatibility conditions can be fulfilled by imposing the Robin-type boundary conditions on the local problems, namely

$$-\frac{\alpha H}{\kappa_i(\mathbf{x})}\ \mathbf{u}_h^i \cdot \check{\mathbf{n}}^i + p_h^i = -\frac{\alpha H}{\kappa_i(\mathbf{x})}\ U_H\ \check{\mathbf{n}}\cdot\check{\mathbf{n}}^i + P_H, \quad \mathbf{x} \in \Gamma_{ij}, \tag{2.6}$$

where $\Gamma_{ij} = \Omega_i \cap \Omega_j$ stands for the interfaces between Ω_i and its nearest neighbor subdomains Ω_j, $(\mathbf{u}_h^i, p_h^i)$ denotes the multiscale solution within subdomain Ω_i, and $\check{\mathbf{n}}^i$ is the normal vector to Γ pointing outside of Ω_i.

Two observations can be drawn from equations (2.5)-(2.6). First one can note from (2.5) that in the limit case of $H = h$, the fine grid solution obtained in the undecomposed case is recovered, and continuity of both velocity and pressure is satisfied at the fine scale h. Second, the parameter appearing in equation (2.6) for the Robin boundary condition, namely

$$\beta_i(\mathbf{x}) = \frac{\alpha H}{\kappa_i(\mathbf{x})}, \tag{2.7}$$

can modify the behavior of the MRCM in such way that other popular methods can be recovered. It was demonstrated in (GUIRALDELLO *et al.*, 2018) that in the limit $\alpha \to 0$, the solution of the MMMFEM of Arbogast et al. (ARBOGAST *et al.*, 2007a) is recovered, while in the limit $\alpha \to +\infty$, the solution of the MHM of Harder et al. (HARDER; PAREDES; VALENTIN, 2013; ARAYA *et al.*, 2013) is obtained. This is intuitively controlled by the parameter α in equation (2.6): In the former (MMMFEM), only flux continuity is weakly imposed in the coarse scale, while in the latter (MHM), only pressure continuity is weakly imposed in the coarse scale.

The differential formulation of the MRCM can be written as: Find solutions $(\mathbf{u}_h^i, p_h^i)$ for each subdomain Ω_i, and global unknowns (U_H, P_H) satisfying the local problems

$$\begin{aligned}
\mathbf{u}_h^i &= -\kappa(\mathbf{x})\ \nabla p_h^i && \text{in } \Omega_i \\
\nabla\cdot\mathbf{u}_h^i &= q && \text{in } \Omega_i \\
p_h^i &= g_p && \text{on } \partial\Omega_i \cap \partial\Omega_p \\
\mathbf{u}_h^i \cdot \check{\mathbf{n}}^i &= g_u && \text{on } \partial\Omega_i \cap \partial\Omega_u \\
-\beta_i \mathbf{u}_h^i \cdot \check{\mathbf{n}}^i + p_h^i &= -\beta_i U_H \check{\mathbf{n}}\cdot\check{\mathbf{n}}^i + P_H && \text{on } \partial\Omega_i \cap \Gamma
\end{aligned} \tag{2.8}$$

and the compatibility conditions on the skeleton Γ

$$\begin{aligned} \sum_{i=1}^{N} \int_{\partial\Omega_i\cap\Gamma} (\mathbf{u}_h^i \cdot \check{\mathbf{n}}^i)\ \psi\, d\Gamma &= 0 \\ \sum_{i=1}^{N} \int_{\partial\Omega_i\cap\Gamma} \beta_i(\mathbf{u}_h^i \cdot \check{\mathbf{n}}^i - U_H\, \check{\mathbf{n}}\cdot\check{\mathbf{n}}^i)\ \phi\ (\check{\mathbf{n}}\cdot\check{\mathbf{n}}^i)\, d\Gamma &= 0 \end{aligned} \tag{2.9}$$

which must hold for all pair of functions $(\phi, \psi) \in \mathscr{U}_H \times \mathscr{P}_H$.

The choice of the coarse spaces $\mathscr{U}_H$ and $\mathscr{P}_H$ also plays an important role in the approximation, which is well explored in (GUIRALDELLO *et al.*, 2019). Also known as interface spaces, $\mathscr{U}_H$ and $\mathscr{P}_H$ are local and independently built on each interface $\Gamma_{i,j} \subset \Gamma$ as subspaces of

$$\mathfrak{F}_h(\mathscr{E}_h) = \{f : \mathscr{E}_h \to \mathbb{R};\ f|_e \in \mathbb{P}_0\ ,\ \forall e \in \mathscr{E}_h\}\,. \tag{2.10}$$

These spaces are spanned by the so-called multiscale basis functions $\{\phi_1, \phi_2, \cdots, \phi_{N_U}\}$ and $\{\psi_1, \psi_2, \cdots, \psi_{N_P}\}$, where $N_U = \dim(\mathscr{U}_H)$ and $N_P = \dim(\mathscr{P}_H)$ are the respective dimensions of the interface spaces. In terms of degrees of freedom per interface, these dimensions are given by $N_U = k_U \times N_I$ and $N_P = k_P \times N_I$, where k_U, k_P and N_I are, respectively, the flux degrees of freedom, pressure degrees of freedom and number of interfaces between subdomains (see (GUIRALDELLO *et al.*, 2018) for more details).

The implementation of the MRCM considers an additive decomposition of the local solutions $(\mathbf{u}_h^i, p_h^i)$ given by

$$\mathbf{u}_h^i = \hat{\mathbf{u}}_h^i + \bar{\mathbf{u}}_h^i, \qquad p_h^i = \hat{p}_h^i + \bar{p}_h^i, \tag{2.11}$$

that satisfies

$$\begin{aligned} \hat{\mathbf{u}}_h^i &= -\kappa(\mathbf{x})\,\nabla\hat{p}_h^i && \text{in } \Omega_i \\ \nabla\cdot\hat{\mathbf{u}}_h^i &= 0 && \text{in } \Omega_i \\ \hat{p}_h^i &= 0 && \text{on } \partial\Omega_i\cap\partial\Omega_p \\ \hat{\mathbf{u}}_h^i\cdot\check{\mathbf{n}}^i &= 0 && \text{on } \partial\Omega_i\cap\partial\Omega_u \\ -\beta_i\hat{\mathbf{u}}_h^i\cdot\check{\mathbf{n}}^i + \hat{p}_h^i &= -\beta_i U_H\check{\mathbf{n}}\cdot\check{\mathbf{n}}^i + P_H && \text{on } \partial\Omega_i\cap\Gamma \end{aligned} \tag{2.12}$$

and

$$\begin{aligned} \bar{\mathbf{u}}_h^i &= -\kappa(\mathbf{x})\,\nabla\bar{p}_h^i && \text{in } \Omega_i \\ \nabla\cdot\bar{\mathbf{u}}_h^i &= q && \text{in } \Omega_i \\ \bar{p}_h^i &= g_p && \text{on } \partial\Omega_i\cap\partial\Omega_p \\ \bar{\mathbf{u}}_h^i\cdot\check{\mathbf{n}}^i &= g_u && \text{on } \partial\Omega_i\cap\partial\Omega_u \\ -\beta_i\bar{\mathbf{u}}_h^i\cdot\check{\mathbf{n}}^i + \bar{p}_h^i &= 0 && \text{on } \partial\Omega_i\cap\Gamma. \end{aligned} \tag{2.13}$$

The local problems in Eq. (2.12) satisfy a nonzero Robin boundary condition for the subdomain coupling and have source terms as well as physics boundary conditions identically equal to zero. They correspond to the homogeneous part of the solution and are used to compute the set of multiscale basis functions. On the other hand, the local problems in Eq. (2.13) have interface Robin boundary condition for the subdomain coupling equal to zero and take into account the

contribution of the source terms as well as the physics boundary conditions. These problems generate one additional local basis function, that represents the non-homogeneous part of the solution.

The interface unknowns U_H and P_H are given by a linear combination of the multiscale basis functions

$$U_H = \sum_{l=1}^{N_U} U_l \phi_l, \qquad P_H = \sum_{l=1}^{N_P} P_l \psi_l, \tag{2.14}$$

where the coefficients U_l and P_l are the solution of the global interface system generated by the Eqs. (2.9) when tested with all basis functions of $\mathscr{U}_H$ and $\mathscr{P}_H$. The multiscale basis functions, in turn, are the solutions to the local problems in Eq. (2.12) by setting the Robin boundary data $(U_H, P_H) = (\phi_l, 0)$ and $(U_H, P_H) = (0, \psi_l)$, respectively. We remark that the local problems can be computed in parallel.

The complete variational formulation, some theoretical results about existence and uniqueness of the solution of MRCM, along with more implementation and algorithmic details can be seen in (GUIRALDELLO *et al.*, 2018; GUIRALDELLO *et al.*, 2019).

Notice that no method was specified for the discretization of (2.8). Any method such as finite volumes, finite elements or finite differences can be used, provided that edge fluxes and pressures at subdomain interfaces are available for the multiscale method when requested.

2.3.1 Cost estimation of the MRCM

To give an idea of the cost of just the elliptic solver by the MRCM in 2D, suppose we have a domain decomposition of $N = N_x \times N_y$ subdomains, each one with $n_x \times n_y$ fine grid cells. The cost is heavily dependent on the choice of the interface spaces $\mathscr{U}_H$ and $\mathscr{P}_H$, described above. The number of basis functions in each subdomain can be estimated as $N_B = 4 \times (k_U + k_P) + 1$, which corresponds to the set of homogeneous basis functions for each one of the 4 edges of the subdomain, plus one additional basis function for the inhomogeneous part of the solution. Notice that some subdomains will have less than that due to physical boundary conditions. To compute the complete set of basis functions, one has to solve approximately N_B problems for a grid of size $n_x \times n_y$ cells per each one of the N subdomains. These problems are independent and can be solved in parallel using multicore machines.

To complete the MRCM algorithm, the solution of one global problem (2.9) has to be computed to write the final solution. The size of this global problem depends on the number of interfaces between subdomains, that is exactly $N_I = N_x \times (N_y - 1) + N_y \times (N_x - 1)$. Then the size of the global interface system is estimated to be $N_I \times (k_U + k_P)$.

Let us consider as an example a domain decomposition of 11×3 subdomains discretized by 20×20 fine grid cells each, choosing the interface spaces as linear polynomials for both flux and pressure. This is a typical domain decomposition in some of our numerical experiments. In

this example, $k_U = k_P = 2$, and the total number of basis functions to be computed is roughly $N_B = 17$ per subdomain, requiring the solution of linear systems for a grid of size $20 \times 20 = 400$ cells. The total amount of work is thus (a) solving 33 local linear systems of dimension 400, each with 17 different right-hand sides, which can be solved all in parallel with no required communication between processing cores, plus (b) solving the global system (2.9) that couples the different subdomains, which has size $N_I \times (k_U + k_P) = 52 \times 4 = 208$ unknowns. Therefore the solution yielded by the MRCM for this example, computed in a parallel environment, is, in principle, cheaper than the cost of the undecomposed case, which requires the solution of a linear system for a grid of size $220 \times 60 = 13200$ cells. The gain increases when larger, three-dimensional problems are considered.

2.3.2 Velocity post-processing (downscaling)

The weak imposition of flux continuity in a coarse scale by the MRCM brings a well known problem in multiscale methods: the normal component of fluxes may not be continuous at the interfaces of the skeleton Γ. A continuous flux at the fine scale is necessary for applications involving the transport of species, such as pollutants (in single-phase flows) or saturation (in two-phase flows and more complex models). Solutions for this problem include post-processing fluxes using downscaling techniques (GUIRALDELLO *et al.*, 2020; FRANCISCO *et al.*, 2014; JENNY; LEE; TCHELEPI, 2003). Some strategies of this type have already been applied to the MRCM in (GUIRALDELLO *et al.*, 2020).

One of these approaches is by averaging fluxes on interfaces defined by

$$\bar{\mathbf{U}}_h^{ij} = \frac{1}{2}\left(\mathbf{u}_h^i|_{\Gamma_{ij}} + \mathbf{u}_h^j|_{\Gamma_{ij}}\right). \tag{2.15}$$

for each interface Γ_{ij}, which defines a unique normal flux, but unbalances masses across subdomains. A remedy is to use the averaged fluxes at the interfaces to define new Neumann local problems to recover mass conservation at the fine scale, by solving

$$\begin{aligned} \tilde{\mathbf{u}}_h^i &= -\kappa\,\nabla \tilde{p}_h^i && \text{in } \Omega_i \\ \nabla\cdot\tilde{\mathbf{u}}_h^i &= q^i && \text{in } \Omega_i \\ \tilde{\mathbf{u}}_h^i\cdot\check{\mathbf{n}}^i &= \mathbf{u}_h^i\cdot\check{\mathbf{n}}^i && \text{on } \partial\Omega_i\cap\partial\Omega \\ \tilde{\mathbf{u}}_h^i\cdot\check{\mathbf{n}}^i &= \bar{\mathbf{U}}_h^{ij}\cdot\check{\mathbf{n}}^i && \text{on } \Gamma_{ij}\ \forall j \end{aligned} \tag{2.16}$$

for all Ω_i, $i = 1, 2, \ldots, N$. Note that the local problems are undefined up to a pressure constant. In order to remove this indeterminacy, a common approach is to impose pressure at some point. After solving all these local problems, normal fluxes are ensured to be continuous and the overall solution is conservative, however, by doing that we violate Darcy's law across subdomains, which is a small price to pay for normal flux continuity. The cost of this downscaling post-processing is one extra local problem solution per subdomain.

Other two downscaling techniques, as well as comparative studies between them can be found in (GUIRALDELLO *et al.*, 2020).

2.4 The transport problem

Different explicit schemes to approximate the solution of scalar conservation laws have been used in the approximation of flows through porous media. For example, the upwind method (LEVEQUE, 2002), high order variations of the Godunov method (EDWARDS, 1996) and central schemes (ABREU; PEREIRA; RIBEIRO, 2009). We consider the central scheme Kurganov-Tadmor (KURGANOV; TADMOR, 2000; DAMIÁN; NIGRO; BUSCAGLIA, 2016) and the classic first order upwind method. Both methods are known to produce robust approximations along with accurate numerical solutions.

Let us consider the hyperbolic conservation law (2.2) in the form

$$\frac{\partial s}{\partial t} + \frac{\partial}{\partial x}(f(s)\, u^x) + \frac{\partial}{\partial y}(f(s)\, u^y) = 0, \tag{2.17}$$

where $u^x = u^x(x,y,t)$ and $u^y = u^y(x,y,t)$ denote the x and y components of the velocity field $\mathbf{u}$. The spacial finite volume semi-discretization is given by

$$\frac{d}{dt}s_{i,j}(t) = -\frac{1}{\Delta x}\Big(F_{i+1/2,j}(t) - F_{i-1/2,j}(t)\Big) - \frac{1}{\Delta y}\Big(G_{i,j+1/2}(t) - G_{i,j-1/2}(t)\Big), \tag{2.18}$$

where the variable $s_{i,j}(t) = s(x_i, y_j, t)$ is assumed to have a piecewise constant variation over each cell (i,j) at time t. The functions $F_{i+1/2,j}$ and $G_{i,j+1/2}$ are the discrete fluxes, which represent the balance of quantities at the faces of cell. Different choices for $F_{i+1/2,j}$ and $G_{i,j+1/2}$ define distinct hyperbolic solvers. In subsection 2.4.1 we present the Kurganov-Tadmor method, while the upwind method is recalled in subsection 2.4.2.

2.4.1 The Kurganov-Tadmor method

The Kurganov-Tadmor (KT) central scheme (KURGANOV; TADMOR, 2000; DAMIÁN; NIGRO; BUSCAGLIA, 2016) has discrete fluxes $F_{i-1/2,j}$ on interfaces $x_{i-1/2}$ given by

$$F_{i-1/2,j} = \left(\frac{f(s^-_{i,j}) + f(s^+_{i-1,j})}{2} - \frac{a_{i-1/2,j}}{2}\left(s^-_{i,j} - s^+_{i-1,j}\right)\right) u^x_{i-1/2,j}, \tag{2.19}$$

where $a_{i-1/2,j}$ is an estimate to local speeds of wave propagation on interfaces

$$a_{i-1/2,j} = \max_{s\in[s_{i-1,j}, s_{i,j}]} \left|f'(s)\right| \tag{2.20}$$

The discrete fluxes $G_{i,j-1/2}$ are calculated in y direction analogously to the $F_{i-1/2,j}$ in x direction.

The saturation solution considers a spatial reconstruction of the form

$$s(x,y,t) = s_{i,j}(t) + \sigma^x_i(x - x_i) + \sigma^y_j(y - y_j), \tag{2.21}$$

for $x_{i-1/2} \le x < x_{i+1/2}$ and $y_{j-1/2} \le y < y_{j+1/2}$. We consider the KT spatial reconstruction given by the limiter function *minmod* (LEVEQUE, 2002):

$$\sigma^x_i = \text{minmod}\left(\frac{s_{i+1,j} - s_{i,j}}{\Delta x}, \frac{s_{i,j} - s_{i-1,j}}{\Delta x}\right) \tag{2.22}$$

and

$$\sigma_j^y = \text{minmod}\left(\frac{s_{i,j+1} - s_{i,j}}{\Delta y}, \frac{s_{i,j} - s_{i,j-1}}{\Delta y}\right), \tag{2.23}$$

where

$$\text{minmod}(a_1, \cdots, a_m) = \begin{cases} \text{sgn}(a_1) \min\limits_{1 \leqslant k \leqslant m} \{|a_k|\}, & \text{if } \text{sgn}(a_1) = \cdots = \text{sgn}(a_m) \\ 0, & \text{otherwise} \end{cases}. \tag{2.24}$$

One can observe that if the reconstruction is constant (i.e, $\sigma_i^x = 0 \; \forall \; i$ and $\sigma_j^y = 0 \; \forall \; j$) then this discretization will result in the Rusanov method (RUSANOV, 1962).

2.4.2 The first order upwind scheme

The first order upwind scheme has the discrete fluxes $F_{i-1/2,j}$ and $G_{i,j-1/2}$ on respective interfaces $x_{i-1/2}$ and $y_{j-1/2}$, given by

$$F_{i-1/2,j} = \begin{cases} f(s_{i-1,j})\, u^x_{i-1/2,j} & \text{if } u^x_{i-1/2,j} > 0 \\ f(s_{i,j})\, u^x_{i-1/2,j} & \text{otherwise} \end{cases} \tag{2.25}$$

and

$$G_{i,j-1/2} = \begin{cases} f(s_{i,j-1})\, u^y_{i,j-1/2} & \text{if } u^y_{i,j-1/2} > 0 \\ f(s_{i,j})\, u^y_{i,j-1/2} & \text{otherwise} \end{cases}. \tag{2.26}$$

In our numerical simulations, the time discretization of Eq. (2.18) is given by the classical Forward Euler method.

CHAPTER

3

AN ADAPTIVE STRATEGY FOR THE MRCM

In this chapter we present the first study on the MRCM for two-phase flows in porous media (ROCHA *et al.*, 2020b). The choice of parameters for the MRCM is thoroughly investigated, demonstrating its accuracy compared to other popular methods for problems with high contrast permeability coefficients. We investigate the performance of the multiscale approximations for two-phase flows taking advantage of the great flexibility to the choice of interface spaces as well as the boundary conditions for subdomain coupling allowed by the MRCM formulation.

From our numerical experiments, we find that the coupling of adjacent subdomains through the imposition of a continuous pressure is the best strategy to approximate two-phase flows in the presence of high permeability channels; such coupling can be implemented by the MMMFEM. On the other hand, the coupling of subdomains through the imposition of continuous normal components of fluxes is an adequate strategy to handle low permeability regions; this can be accomplished by the use of the MHM. Thus, accuracy in the approximation of two-phase flows would require that, adaptively, the numerical procedure to solve for velocity and pressure switches between the MMMFEM and MHM, depending on the underlying heterogeneity A method that allows one to switch between the MMMFEM and MHM locally in the skeleton of the domain decomposition is not known. However, such task is easily accomplished if one takes advantage of a built-in algorithmic parameter of the MRCM, that allows this method to produce either MMMFEM-like or MHM-like solutions, by setting this parameter to extreme values. The MRCM is the only multiscale procedure that has this flexibility to switch from Dirichlet-dominated to Neumann-dominated coupling of subdomains; a new adaptive scheme based on this idea is proposed.

The adaptive strategy is introduced to give specific treatment to selected regions of the domain according to the variation on the permeability field. For this purpose, instead of dealing with a previously fixed α parameter in equation (2.7), we will instead consider a more flexible

definition of β_i,

$$\beta_i(\mathbf{x}) = \frac{\alpha(\mathbf{x})H}{\kappa_i(\mathbf{x})}, \tag{3.1}$$

such that $\alpha(\mathbf{x})$ can be locally chosen in an adaptive fashion. We remark that the concept of adaptivity has been very recently applied in the numerical approximation of two-phase flows (CORTINOVIS; JENNY, 2017), where improved accuracy in numerical solutions requires the construction of special multiscale basis functions adapted to the underlying heterogeneity.

In the next sections, we present numerical results, comparisons, and an assessment of the MRCM for two-phase flows. We fix the numerical set-up for this chapter in section 3.1, after that we show our numerical experiments. Initially, in section 3.2, we study global errors of saturation and velocity fields and compare our findings with single-phase flows results discussed in (GUIRALDELLO *et al.*, 2018; GUIRALDELLO *et al.*, 2019). Then we focus on a detailed analysis of fingering instabilities in heterogeneous permeability fields. In section 3.3 we consider high-contrast permeability fields having either a high permeability channel or a low permeability region. Our numerical studies indicate that the best solutions for two-phase flows in such challenging fields occur for extreme values of α. These numerical results are used in the adaptive strategy for setting the parameter α according to the variation of the permeability field. Results with this new strategy are presented in section 3.4, followed by section section 3.5 with the concluding remarks of the chapter.

3.1 Numerical set-up

The MRCM is investigated through several numerical simulations of two-phase flows in high-contrast formations. In all simulations the reservoir is initially fully saturated with oil and water is injected at a constant rate. We use quadratic relative permeability curves: $k_{ro} = (1-s)^2$ and $k_{rw} = s^2$, such that the fractional flow function is given by

$$f(s) = \frac{Ms^2}{Ms^2 + (1-s)^2}, \tag{3.2}$$

where $M = \mu_o/\mu_w$. We take $M = 40$ in our numerical experiments.

For each production well, the fraction of oil in the produced fluid is given by

$$\mathscr{P}(t) = 1 - \frac{\int_{\partial\Omega_{\text{out}}} f(s)\,\mathbf{u}\cdot\mathbf{n}\,dl}{\int_{\partial\Omega_{\text{out}}} \mathbf{u}\cdot\mathbf{n}\,dl}, \tag{3.3}$$

where $\partial\Omega_{\text{out}}$ denotes the outflow well boundaries with the outward unit normal $\mathbf{n}$. We refer to the dimensionless time expressed in Pore Volume Injected (PVI), a standard time unit in reservoir simulation that refers to the fraction of the total accessible pore volume that has been injected into the domain (CHEN; HUAN; MA, 2006)

$$T_{\text{PVI}} = -V_p^{-1} \int_0^t \int_{\partial\Omega_{\text{in}}} \mathbf{u}(\mathbf{x},\tau)\cdot\mathbf{n}\,dl\,d\tau, \tag{3.4}$$

where V_p is the total pore-volume of the reservoir, t is the time taken for injection and $\partial\Omega_{\text{in}}$ the inflow well boundaries with the outward unit normal $\mathbf{n}$.

The time steps are chosen such that they satisfy a CFL condition (LEVEQUE, 2002).The number of transport steps between successive elliptic updates used in the operator splitting scheme is at most 20. The hyperbolic equation (2.2) is approximated by an explicit Euler time integration combined with the Kurganov-Tadmor method. We use the extrapolation of Eq. (2.4) in our numerical experiments.

We present and discuss results of numerical simulations performed with two-dimensional permeability fields set initially to be layers of the 3D SPE10 field (<www.spe.org/web/csp/index.html>) (CHRISTIE; BLUNT, 2001). For the fields considered the permeability contrast is $K_{\max}/K_{\min} \approx 10^6$ and the computational grid has 220×60 cells distributed on a rectangular domain $\Omega = [0, 11/3] \times [0, 1]$. In most of our simulations, we consider a slab geometry, with no-flow boundary conditions at the top and bottom boundaries ($y = 0$ and $y = 1$) along with an imposed flux on the left ($x = 0$) and right ($x = 11/3$) boundaries, with no source terms. This is the geometry considered in the numerical experiments unless stated otherwise.

Concerning the MRCM, we consider linear polynomials spaces $\mathscr{U}_H$ and $\mathscr{P}_H$ for interfaces unknowns. For simplicity, the skeleton partition $\mathscr{T}_H$ is built by taking only one element per interface Γ_{ij} between subdomains. Refinements of $\mathscr{T}_H$ are possible in the MRCM algorithm, but these are left for future work. The downscaling scheme presented in the previous chapter is used.

3.2 Two-phase flows: global errors

The objective of this study is to investigate whether the improved accuracy shown by the MRCM when compared to existing procedures in the approximation of single phase flow (GUIRALDELLO *et al.*, 2018; GUIRALDELLO *et al.*, 2019) is also present for two-phase flows. In the references just mentioned the improved accuracy of the MRCM indicates that typically minimal error for pressure and flux is attained somewhere between the MMMFEM-like and MHM-like solutions. Note that by setting small (respectively, large) values for the MRCM algorithmic parameter α one can produce MMMFEM-like (resp., MHM-like) numerical approximations.

Numerical results obtained with the MRCM for two-phase problem at $T_{\text{PVI}} = 0.3$ are shown in Figure 1 for some selected layers of the SPE10 field that contain channelized structures. The domain is divided into 11×3 subdomains with 20×20 cells into each one. The $L^2(\Omega)$ and $L^1(\Omega)$ relative errors, for flux and water saturation, respectively, are computed with respect to a reference fine grid solution. Figure 1 shows that the behavior of the errors for the flux is similar to that reported in (GUIRALDELLO *et al.*, 2018), where a strong dependence on the parameter α is noticed. We have observed that applying a downscaling procedure (used here, but not in (GUIRALDELLO *et al.*, 2018)) shifts the position of the minimum for the errors from

values of $\alpha \in [1, 100]$ to $\alpha \in [0.01, 1]$. Moreover, the minimum errors for saturation and flux are attained at essentially the same values of α. Once the minimum errors for saturation occur for intermediate values of α we confirm that the MRCM when applied to two-phase flows produces more accurate solutions when compared to both MMMFEM and MHM. We have selected layer number 36 of the SPE10 field to investigate flux and saturation errors throughout a simulation. Figure 2 shows that the minima for both quantities do not vary significantly over time.

Figure 1 – Relative errors computed at $T_{\text{PVI}} = 0.3$. $L^2(\Omega)$ errors for flux (top) and $L^1(\Omega)$ errors for saturation (bottom). Each curve shows the results of a different SPE10 layer as a function of the algorithmic parameter α. Note that the minimum errors for saturation and flux are attained at intermediate values of α.

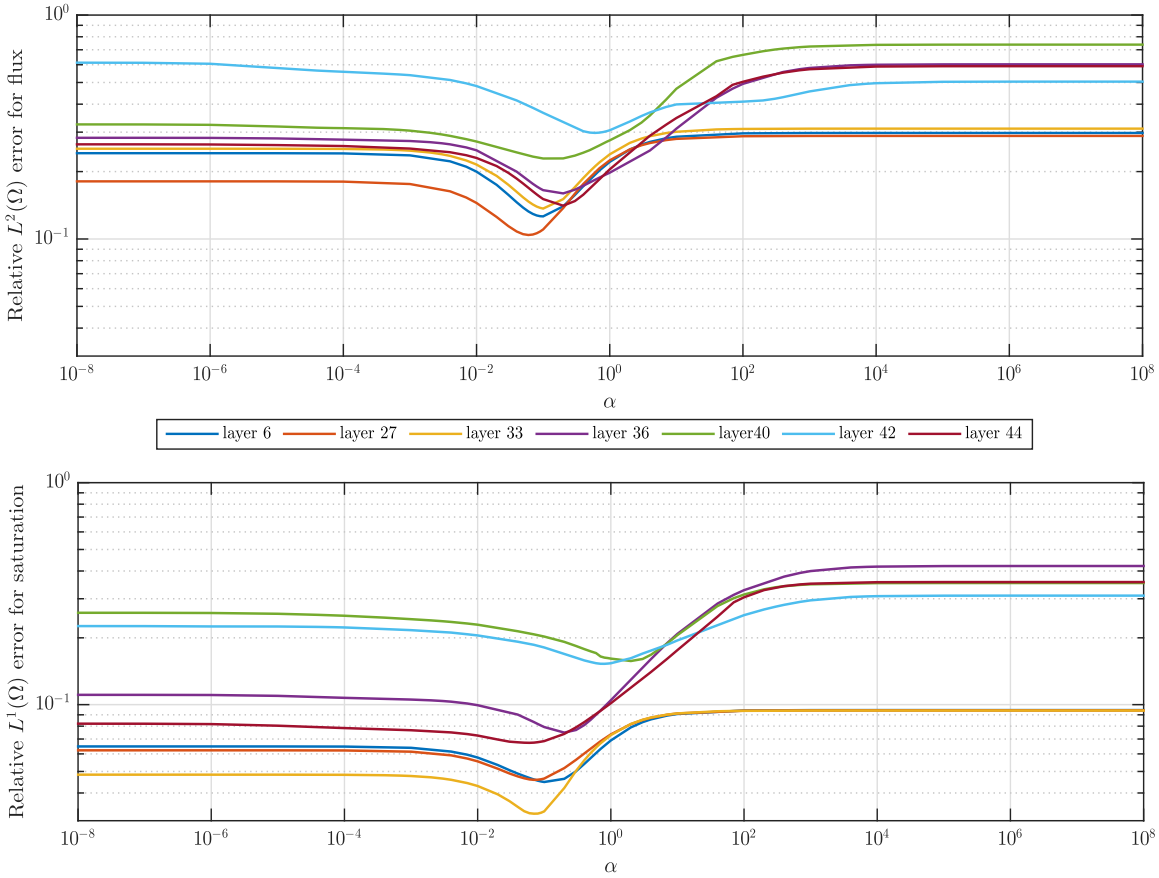

Source: Research data.

Next, in line with similar studies discussed in (KIPPE; AARNES; LIE, 2008) and (GUIRALDELLO *et al.*, 2019), we consider all SPE10 layers in a study to assess the accuracy of the MRCM when compared to two-phase flows approximated by the MMMFEM and the MHM. We set $\alpha = 1$ in the MRCM (see (GUIRALDELLO *et al.*, 2019) for a justification of this choice) and we refer to the method with this choice as the MRCM-usual. In order to produce MMMFEM-like and MHM-like solutions we take $\alpha = 10^{-8}$ and $\alpha = 10^{8}$, respectively. In Figure 3 we present $L^2(\Omega)$ and $L^1(\Omega)$ relative errors for flux and saturation, respectively. The errors are computed at $T_{\text{PVI}} = 0.3$ for all SPE10 layers. Note that the MHM-like solutions are the least accurate ones, a result that is similar to a study presented in (GUIRALDELLO *et al.*, 2019)

Figure 2 – Relative errors for layer 36 as a function of the algorithmic parameter α at different times. $L^2(\Omega)$ errors for flux (top) and $L^1(\Omega)$ errors for saturation (bottom). Note that the behavior of errors for both quantities do not vary significantly throughout the simulation.

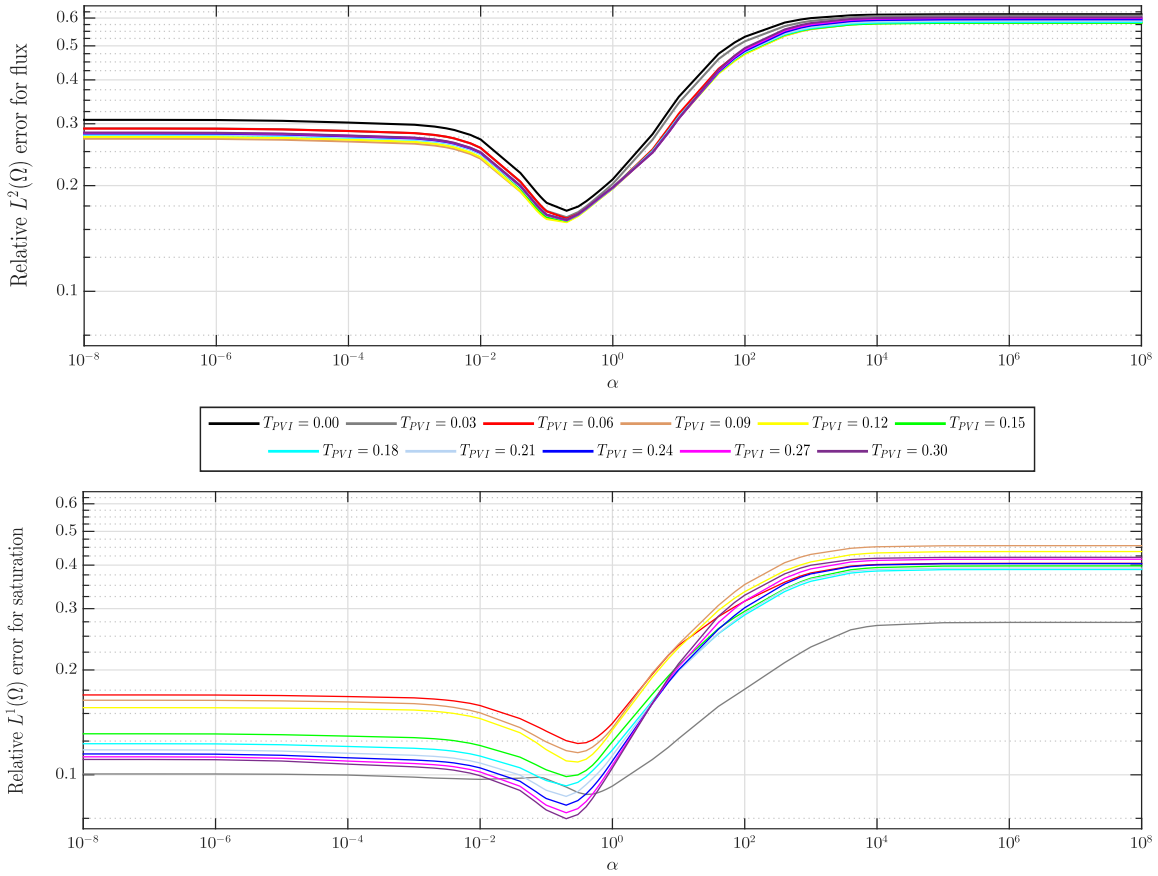

Source: Research data.

(performed with other choices of interface spaces, without the effect of downscaling and for single-phase flows). The MRCM-usual solution is comparable in accuracy to the MMMFEM-like solution, however for the flux variable the MMMFEM-like solution behaves poorly for some of the layers around 40 and 80. These results are reflected also in the corresponding saturation fields. Our results indicate that the MRCM-usual produces more accurate solutions for flux and saturation than the corresponding solutions produced with the MHM-like method, for all layers of the SPE10 field. Moreover the MRCM-usual results are more accurate than the simulation results performed with the MMMFEM-like method in the case where the permeability field is highly channelized (layers 36 to 85).

We close this discussion of global errors with the result reported in Figure 4. In order to illustrate that the choice of a domain decomposition does not affect the main trend of saturation error curves, we consider different domain decompositions for the 36th layer of SPE10 project. Errors are computed at $T_{\text{PVI}} = 0.3$ and can be seen in Figure 4. We consider subdivisions of 11×3, 20×4 and 22×6 subdomains, having 20×20, 11×15 and 10×10 fine grid cells inside each subdomain, respectively.

Figure 3 – Relative flux and saturation errors for the MRCM-usual, the MMMFEM-like method and the MHM-like method for each layer of the SPE10 field at $T_{\text{PVI}} = 0.3$. $L^2(\Omega)$ error for flux (top) and $L^1(\Omega)$ error for saturation (bottom). Note that the MRCM-usual is the most accurate procedure on highly channelized permeability layers (36 to 85).

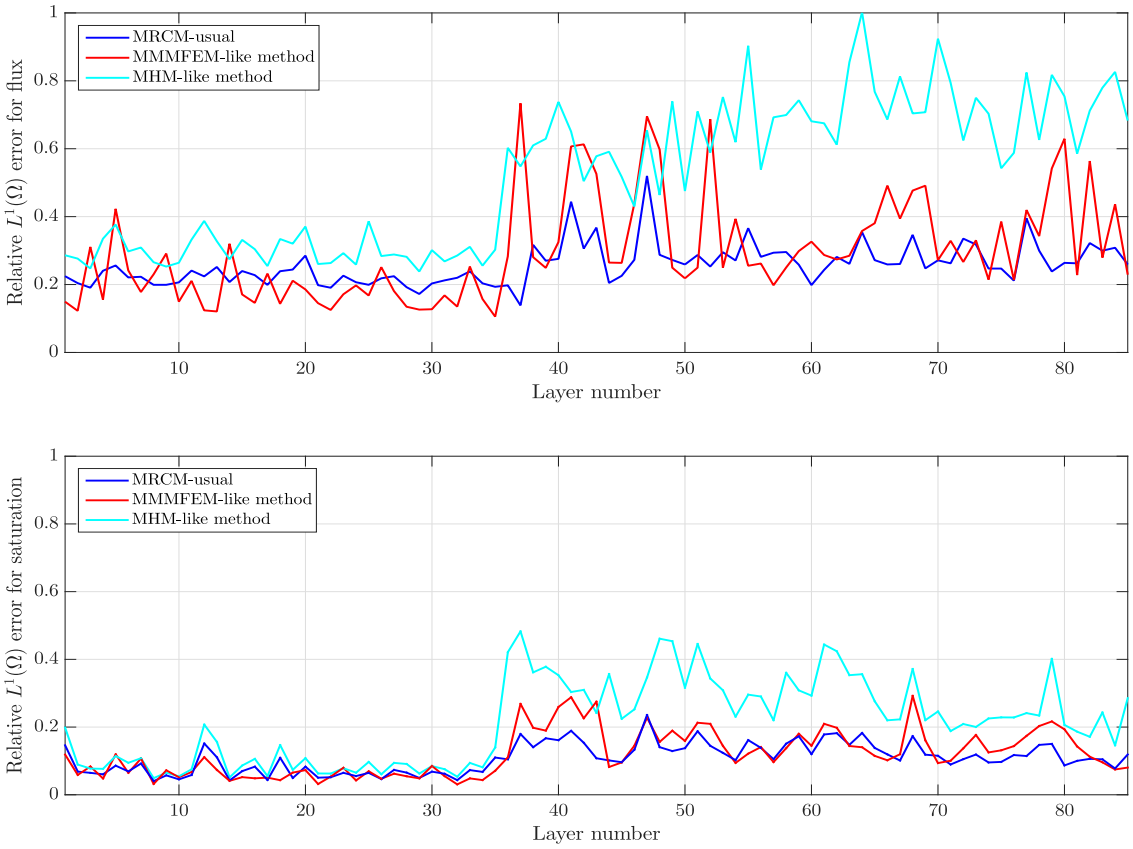

Source: Research data.

Multi-phase flows in high-contrast formations are typically dominated by fingering instabilities. The details of such fingers are not well captured by the global norms considered above. However, the correct approximations of such water-oil fingers is essential in predicting breakthrough times, that are important for decision making in reservoir engineering. Next we perform a more detailed assessment of the performance of multiscale mixed methods by comparing their 2D saturation profiles. We will also compare results produced by multiscale mixed methods with a classical multiscale method: the Multiscale Finite Volume Method (MSFV) (JENNY; LEE; TCHELEPI, 2003; LUNATI; LEE, 2009).

3.3 Two-phase flows: detailed analysis

We now compare saturation profiles of two-phase flows approximated by the MRCM, the MMMFEM-like and MHM-like procedures and the MSFV.

Figure 4 – Relative $L^1(\Omega)$ error for saturation as a function of the algorithmic parameter α for different choices of the domain decomposition. Errors are calculated for the 36th layer of the SPE10 field at $T_{\text{PVI}} = 0.3$. We compare results for subdivisions of the domain in 11×3, 20×4 and 22×6 subdomains with 20×20, 11×15 and 10×10 fine grid cells in each subdomain, respectively. Note that all domain decompositions considered share the same trend for the saturation error curves.

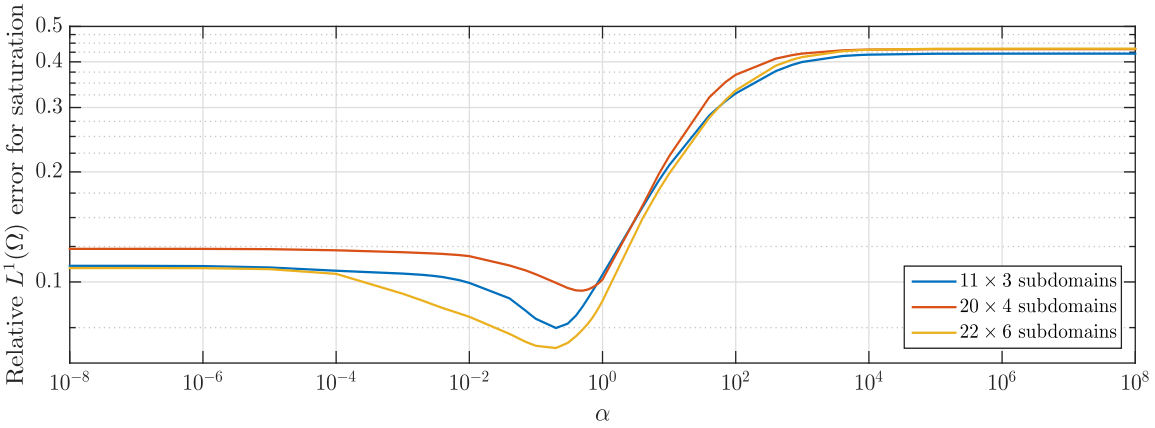

Source: Research data.

3.3.1 Permeability field with a high permeability channel

In our first study we consider the 36th layer of the SPE10 field with a domain decomposition of 20×4 subdomains, each one discretized by 11×15 cells. Note that the MSFV version that we use for comparison (presented in (JENNY; LEE; TCHELEPI, 2003) with the correction functions proposed in (LUNATI; LEE, 2009)) requires an odd number of cells in each direction in the discretization of subdomains. Layer 36 of the SPE10 project has a channel of high permeability. The approximation of the velocity field in such a high-contrast formation presents a challenge for the multiscale methods. Figure 5 shows the permeability field (log-scaled) along with the saturation profiles at $T_{\text{PVI}} = 0.06$ (before breakthrough time) approximated by multiscale methods. The methods that produce a saturation solution closer to the reference run (fine grid solution of the problem at hand) are the MRCM-usual and MMMFEM-like method, while the latter is the most accurate in capturing the details of the fingers. The MSFV and the MHM-like method produce very inaccurate solutions for this channelized permeability field. The oil production curves along with saturation relative errors corresponding to the simulations reported in Figure 5 are displayed in Figure 6. In this figure, the breakthrough time for the fine grid simulation is illustrated by a dashed line in the saturation relative errors plot. The oil production curve computed by the MHM-like method clearly differs considerably from the reference one. The procedures that better predict oil production curves are the MRCM-usual and the MMMFEM-like method. The saturation global errors reflect these results: we note that the errors associated with the MRCM-usual and MMMFEM-like method are the smallest.

We also consider another version of this example by using a point source for water injection and production wells, along with no-flow boundary condition in the whole domain,

Figure 5 – Comparison of multiscale methods. Saturation profiles at $T_{\text{PVI}} = 0.06$ for layer 36 of the SPE10 field are shown. Left column, top to bottom: high-contrast permeability field (log-scaled); MSFV saturation profile; MMMFEM-like saturation profile. Right column, top to bottom: reference fine grid solution; MRCM-usual saturation profile; MHM-like saturation profile. The MMMFEM-like method is the most accurate in capturing the details of the fingers on this field with a high permeability channel.

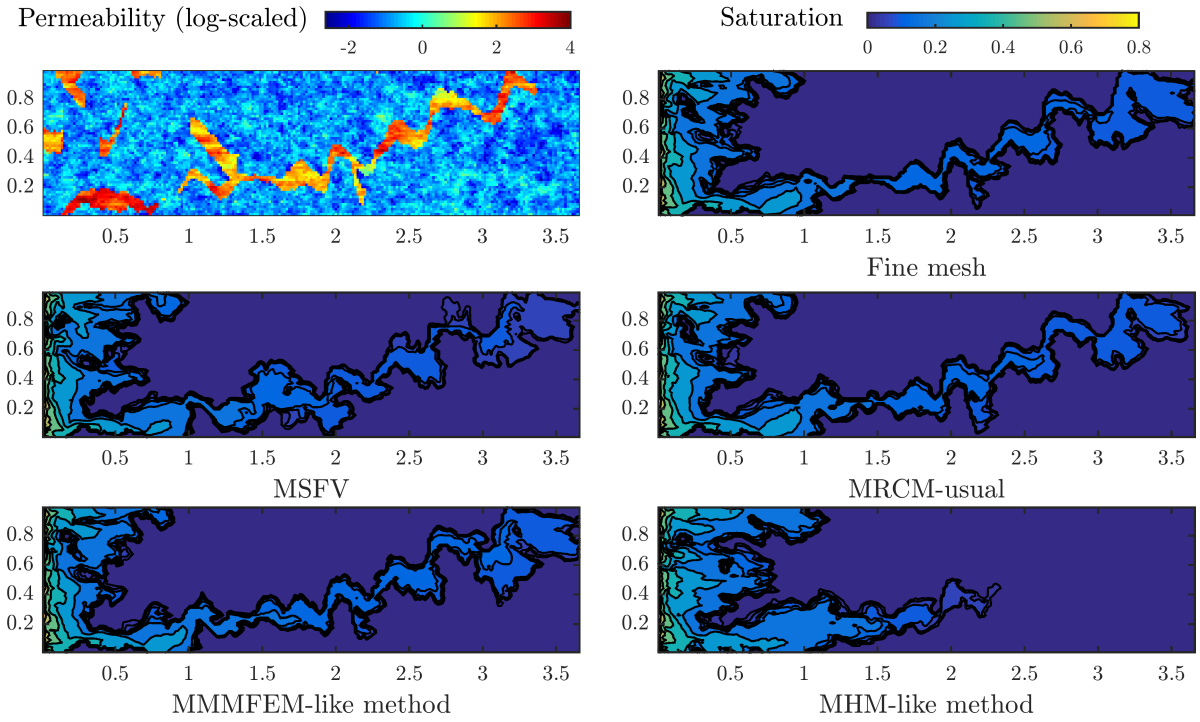

Source: Research data.

keeping the same permeability field and domain decomposition of the previous case. Water is injected at the bottom-left corner while the production well is located at the top-right corner. The saturation profiles at $T_{\text{PVI}} = 0.13$ (just before breakthrough time) are shown in Figure 7, where one can observe the same behavior as for the slab geometry, with the MMMFEM-like being the most accurate in capturing the details of the fingers. Similar results are also attained for the oil production curves and saturation relative errors, presented in Figure 8, where better predictions of oil production curves are obtained by the MMMFEM-like method, as well as the smallest saturation global errors.

3.3.2 Permeability field with a region of low permeability

Regions of low permeability also pose difficulties for multiscale methods. In order to assess the various methods considered here in such a situation we built a region of low permeability taking advantage of the channelized structure of layer 36. We consider a region at the bottom left corner of the layer 36 with 165×45 fine grid cells divided into 15×3 subdomains. The low permeability region is defined along the channel of layer 36. The boundary conditions for this case follow the slab geometry as before. Figure 9 shows the permeability

Figure 6 – Oil production curve (left) and relative $L^1(\Omega)$ errors for saturation (right) on layer 36 of SPE10 model as a function of time. The breakthrough time is illustrated by a dashed line (right plot). We note that the best approximations of oil production curves and the smallest saturation errors are performed by the MRCM-usual and MMMFEM-like method.

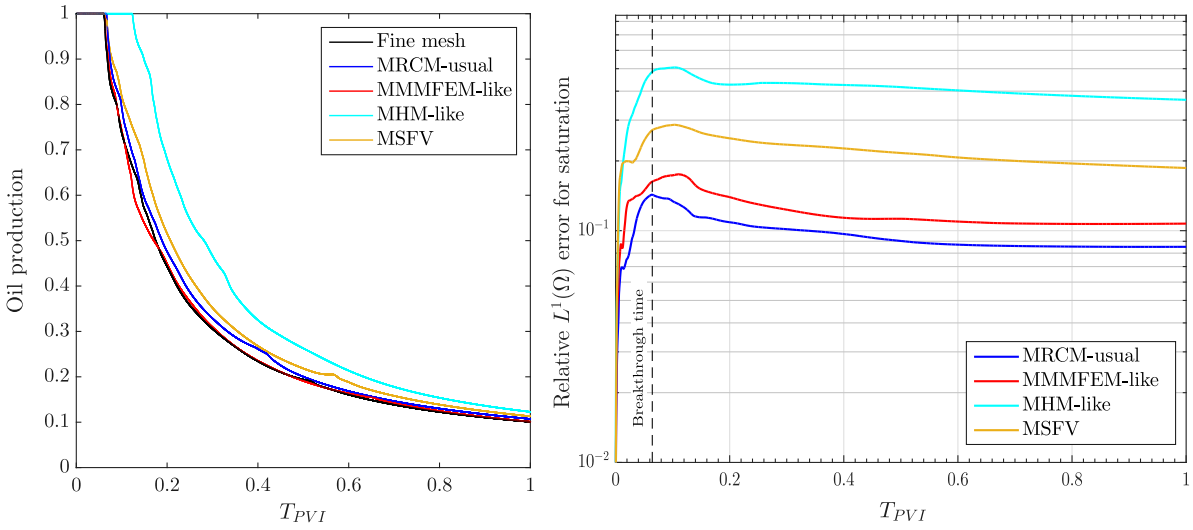

Source: Research data.

field (log-scaled) with the region of low permeability and saturation profiles at $T_{\text{PVI}} = 0.09$ (before breakthrough). In contrast to our findings in the previous example the only procedure that produces a saturation field close to the reference solution is the MHM-like method. Figure 10 shows the oil production curve and the relative saturation error as a function of time. Note that all oil production curves are quite inaccurate. This confirms that problems with obstacles are difficult to approximate by multiscale methods. The saturation errors produced by the MHM-like method after breakthrough time are the smallest. These results indicate that the remaining procedures (MRCM, MMMFEM-like method and MSFV) produce poor quality solutions in presence of low permeability regions.

We repeat this example now with point source and sink, along with no-flow boundary condition in the whole domain, keeping the same permeability field and domain decomposition as the previous simulation. Water is injected at the bottom-left corner, while the production well is located at the top-right corner of the domain. The saturation profiles at $T_{\text{PVI}} = 0.18$ (just before breakthrough time) are shown in Figure 11, where one can note that the MHM-like is the most accurate method, the same conclusion as in the slab geometry case. Similar results are also obtained for the oil production curves and saturation relative errors, which are presented in Figure 12. All approximations of oil production curves are inaccurate and the smallest saturation global errors after breakthrough time are associated with the MHM-like method.

Figure 7 – Comparison of multiscale methods using point source and no-flow boundary conditions. Saturation profiles at $T_{\mathrm{PVI}} = 0.13$ for layer 36 of the SPE10 field are shown. Left column, top to bottom: high-contrast permeability field (log-scaled); MSFV saturation profile; MMMFEM-like saturation profile. Right column, top to bottom: reference fine grid solution; MRCM-usual saturation profile; MHM-like saturation profile. The MMMFEM-like method is the most accurate in capturing the details of the fingers.

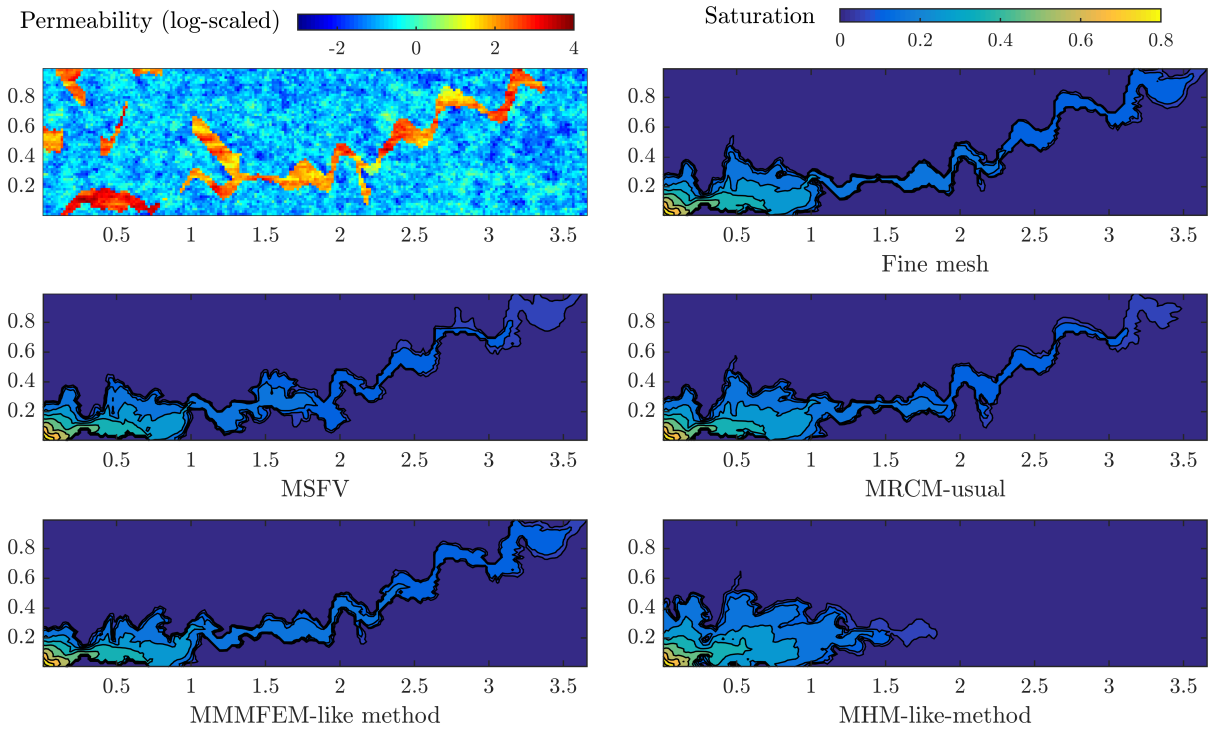

Source: Research data.

3.4 Adaptive MRCM

The two studies reported above (permeability fields with either a high permeability channel and a low permeability region) illustrate the difficulties of multiscale methods in the approximation of velocity fields in high-contrast formations. Although relative errors for saturation attain minima for the MRCM with the algorithmic parameter $\alpha \approx 1$ (see Figure 1) we have determined that $\alpha = 10^{-8}$ (the MMMFEM-like method) is appropriate for the approximation of velocity fields in the presence of high-permeability channels. This is an indication that the coupling of nearest neighbor subdomains through the imposition of a continuous pressure is the best strategy to approximate flow in the presence of high permeability channels. On the other hand, the coupling of subdomains through the imposition of continuous normal components of fluxes accomplished by setting $\alpha = 10^{8}$ (the MHM-like method) is an adequate strategy to handle low permeability regions. Note that the MRCM, as opposed to the other multiscale procedures discussed here, has enough built-in flexibility to handle both challenging permeability fields, by varying its algorithmic parameter α.

In order to further assess the accuracy of the methods considered here we construct

Figure 8 – Oil production curve (left) and relative $L^1(\Omega)$ errors for saturation (right) on layer 36 of SPE10 model as a function of time using point source and no-flow boundary conditions. The breakthrough time is illustrated by a dashed line (right plot). We confirm the better performance of the MMMFEM-like method throughout the simulation.

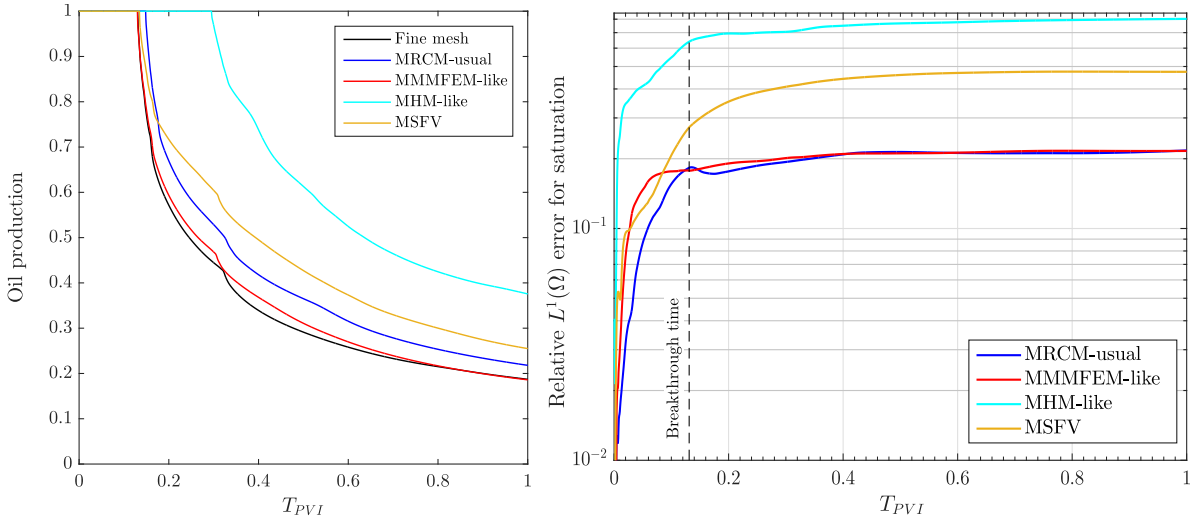

Source: Research data.

a challenging, high-contrast permeability field that contains both types of structures: a high permeability channel and a low permeability region. The domain considered is $\Omega = [0,33/12] \times [0,3/2]$ with 165×90 fine grid cells equally divided into 15×6 subdomains. The upper half of the permeability field contains part of the channel structure from layer 36 of the SPE10 project and the lower half contains a region of low permeability. The permeability contrast is $K_{\max}/K_{\min} \approx 10^9$ and the field is shown in Figure 13. The upper and lower regions are separated by a low permeability strip. The studies reported above indicate that for this permeability field all the multiscale methods that we have considered might produce inaccurate solutions.

In order to approximate the saturation solution in this challenging permeability field we propose initially a naive strategy for the selection of the MRCM parameter α. We use $\alpha = 10^{-8}$ (MMMFEM-like method) for the upper half containing the high permeability channel and $\alpha = 10^{8}$ (MHM-like method) for the half containing the low permeability region. We refer to this method as the MRCM-naive. We intend to use this example as a proof of concept: by varying the algorithmic parameter α of the MRCM we intend to show that we can produce good approximations velocity fields in complex, high-contrast formations. Clearly this strategy would not be applicable in fields exhibiting multiple channelized and low permeability regions. We will address the general case later.

Figure 14 shows the choice for α at the boundaries of subdomains. A comparison of multiscale solution methods at $T_{\text{PVI}} = 0.06$ is illustrated in Figure 15. For the upper half of the domain the MHM-like procedure is clearly inaccurate while for the lower half the remaining procedures (MSFV, MRCM-usual and the MMMFEM-like method) provide poor approximations. Therefore the only procedure that produces a saturation solution close to the reference run is the

Figure 9 – Comparison of multiscale methods. Saturation profiles at $T_{\text{PVI}} = 0.09$ for a permeability field exhibiting a low permeability region are shown. Left column, top to bottom: high-contrast permeability field (log-scaled); MSFV saturation profile; MMMFEM-like saturation profile. Right column, top to bottom: reference fine grid solution; MRCM-usual saturation profile; MHM-like saturation profile. Note that the MHM-like solution is considerably more accurate than the others.

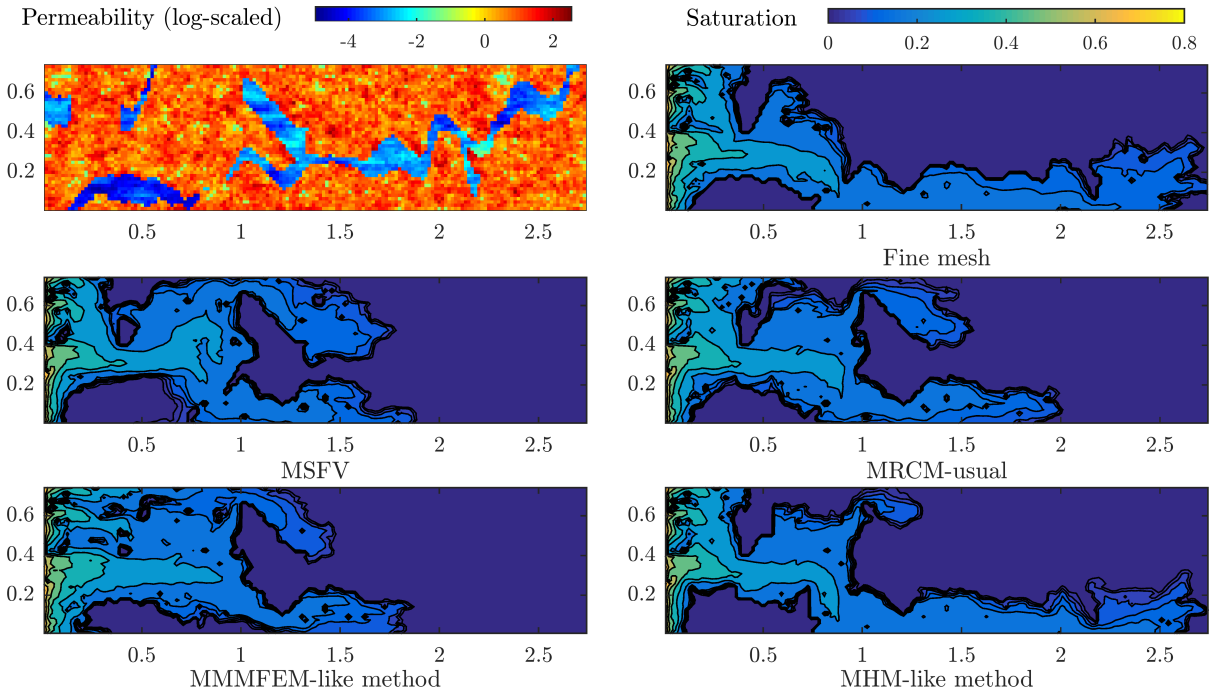

Source: Research data.

MRCM-naive. Figure 16 shows the comparison of saturation profiles at $T_{\text{PVI}} = 0.5$, where it can be seen that these findings are even more evident after breakthrough.

Aiming at approximating velocity fields in realistic permeability fields where a clear separation of high and low permeability regions would not be possible we introduce an adaptive strategy for the choice of the α parameter. The basic idea is to identify the regions of high permeability and set α adaptively. We remark that a special treatment for distinct permeability regions has recently appeared in (CORTINOVIS; JENNY, 2017) where the focus was the construction of additional multiscale basis functions in selected regions. Our focus is computationally more competitive because we achieved improved approximation capabilities without adding multiscale basis function to the original set.

Our proposed strategy consists in setting the value of α locally, depending on the values of the permeability field at the boundaries of the subdomains. We set $\alpha = 10^{-8}$ (a MMMFEM-like method) for regions where the permeability is larger than a cutoff value ζ and $\alpha = 10^{8}$ (a MHM-like method) for the remaining subdomain boundaries. This procedure can be considered in a preprocessing operation, in which we map the absolute permeability variations and set α only once in an offline step. We refer to MRCM with α set through this procedure as the MRCM-adaptive. Figure 17 shows the α values set by the proposed method for $\zeta \in [10^0, 10^1, 10^2, 10^3]$.

Figure 10 – Oil production curve (left) and relative $L^1(\Omega)$ errors for saturation (right) on a region of low permeability as function of time. The breakthrough time is illustrated by dashed line (right plot). We note that all approximations of oil production curves are inaccurate. The smallest saturation errors are obtained by the MHM-like method.

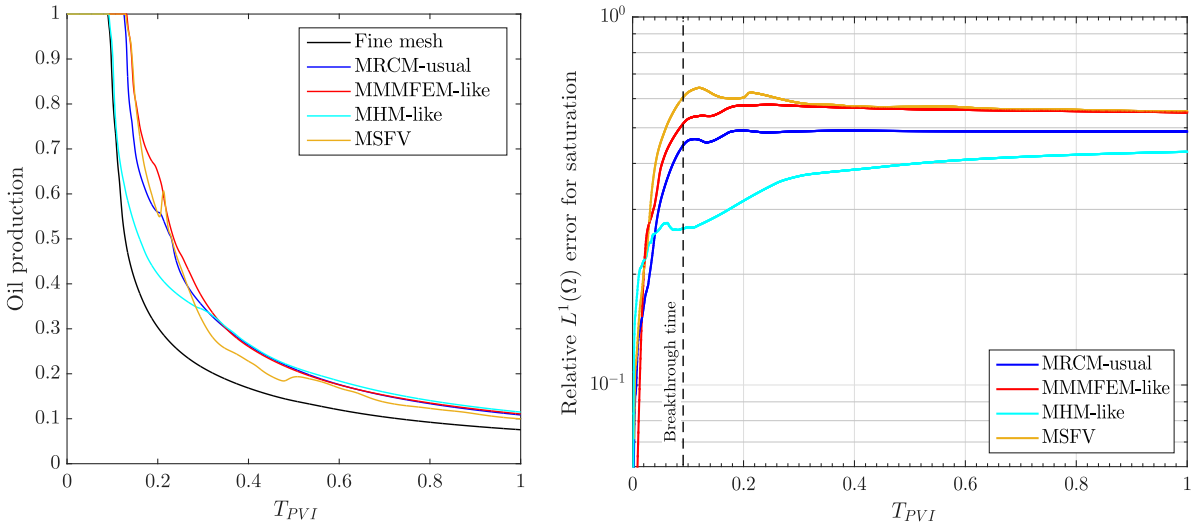

Source: Research data.

We note that the high permeability channel structure is well captured for $\zeta = 10^1$ or $\zeta = 10^2$. In the study reported below we set $\zeta = 10$.

The comparison of saturation profiles for the MRCM (MRCM-usual, MRCM-naive and MRCM-adaptive) at $T_{\text{PVI}} = 0.06$ is displayed in Figure 18. Note in Figure 18 that the MRCM-naive and MRCM-adaptive provide more accurate solutions than the MRCM-usual. This comparison for a later time ($T_{\text{PVI}} = 0.5$) is shown in Figure 19. Note that the better solutions produced by the MRCM-naive and MRCM-adaptive remain the best after breakthrough. Figure 20 shows oil production curves and relative saturation errors as a function of time. The procedures that yield oil production curves close to the reference one are the naive and adaptive versions of the MRCM. The saturation results after breakthrough time (illustrated by the dashed line) show smaller errors for these strategies. Note that, in particular, the MRCM-adaptive produces the smallest errors. In summary with the adaptive strategy we have successfully predicted reservoir production in high contrast formations with both channels and obstacles.

3.5 Discussion

The Multiscale Robin Coupled method has been carefully investigated for the numerical solution of two-phase, oil-water flows in heterogeneous, high-contrast porous media. The governing system of equations is discretized by an operator splitting technique, such that elliptic equations for velocity and pressure and a hyperbolic conservation law for the water saturation are solved sequentially in time.

Figure 11 – Comparison of multiscale methods using point source and no-flow boundary conditions. Saturation profiles at $T_{\text{PVI}} = 0.18$ for a permeability field exhibiting a low permeability region are shown. Left column, top to bottom: high-contrast permeability field (log-scaled); MSFV saturation profile; MMMFEM-like saturation profile. Right column, top to bottom: reference fine grid solution; MRCM-usual saturation profile; MHM-like saturation profile. Note that the MHM-like solution is the most accurate.

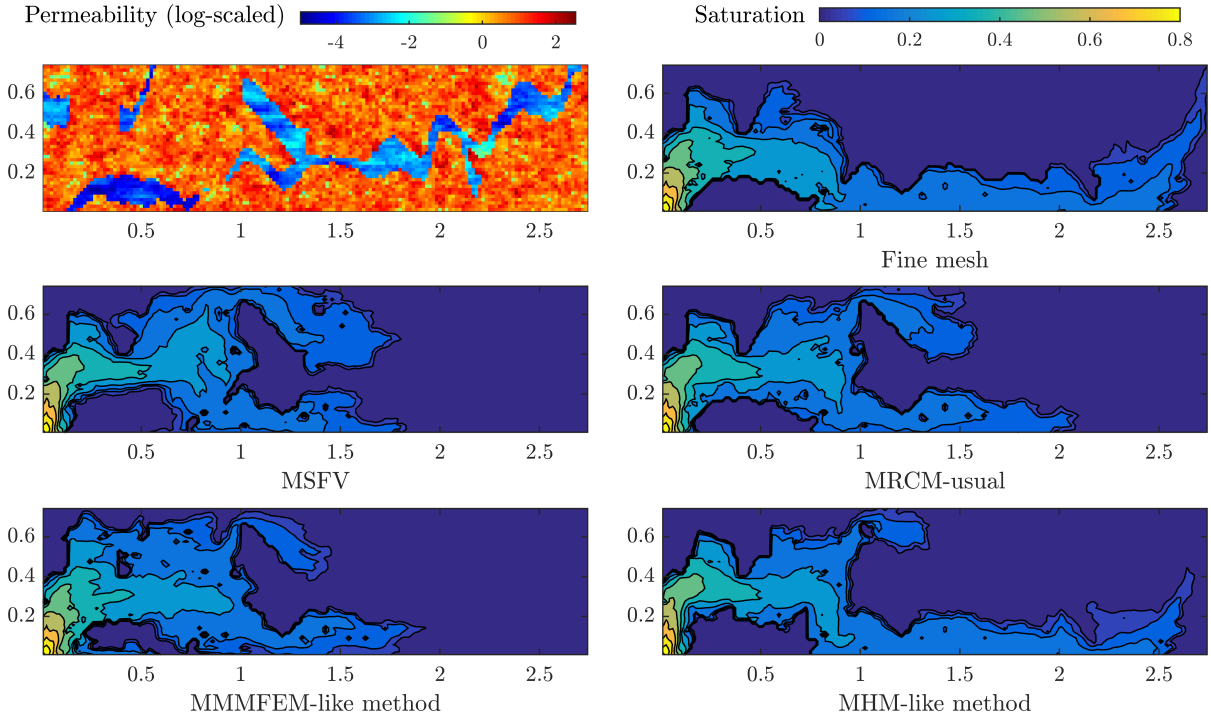

Source: Research data.

Initially we show that, in line with results obtained for single phase flows, the MRCM produces more accurate solutions than other well known multiscale procedures (in terms of global norms of velocity and saturation fields). Then we focus on a detailed investigation of how well multiscale methods approximate oil-water fingering instabilities in very high-contrast, realistic permeability fields. We show that, within multiscale mixed methods, the best scenario for the approximation of these problems involve two well known procedures: the Multiscale Mortar Mixed Finite Element Method (that we show to be appropriate for the approximation of flows in high permeability channels) and the Multiscale Hybrid-Mixed Finite Element Method (that we show to be adequate to handle low permeability regions). By taking advantage of an algorithmic parameter of the MRCM we develop a new adaptivity strategy, such that depending on the local properties of the permeability field we can easily switch between the known procedures to achieve much better accuracy in comparison with these procedures alone.

Figure 12 – Oil production curve (left) and relative $L^1(\Omega)$ errors for saturation (right) on a region of low permeability as a function of time, using point source and no-flow boundary conditions. The breakthrough time is illustrated by a dashed line (right plot). We confirm the better performance of the MHM-like method.

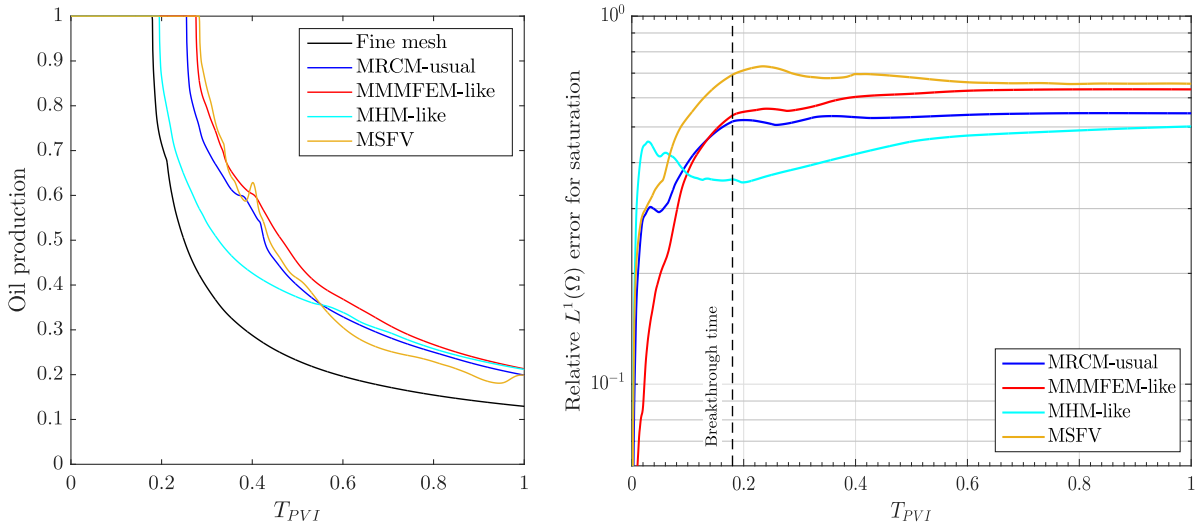

Source: Research data.

Figure 13 – A high-contrast permeability field (log-scaled) built to assess the accuracy of multiscale methods. The upper half contains the channel structure from layer 36 of the SPE10 field and the lower half contains a low permeability region. The permeability contrast is $K_{\max}/K_{\min} \approx 10^9$.

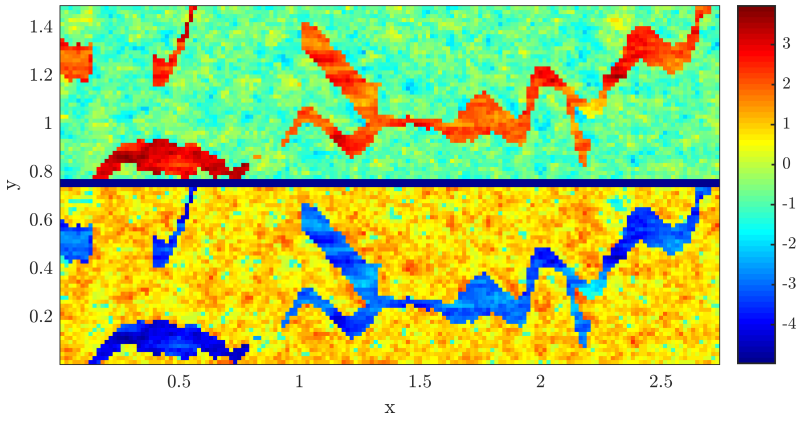

Source: Research data.

Figure 14 – Choice of the parameter α on subdomain boundaries for the MRCM-naive. The upper half considers the MMMFEM-like method by setting $\alpha = 10^{-8}$ (red). The lower half considers the MHM-like method by setting $\alpha = 10^{8}$ (cyan).

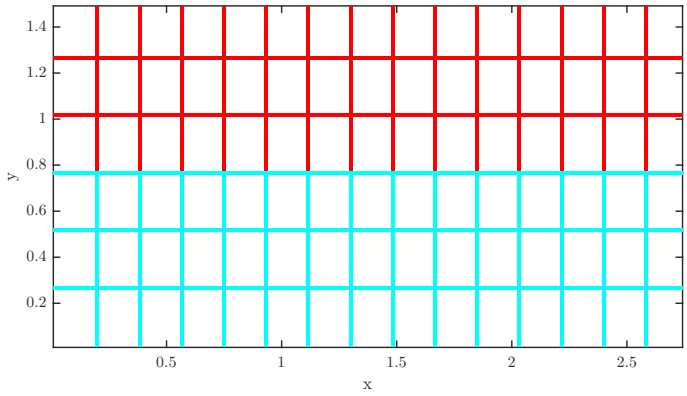

Source: Research data.

Figure 15 – Saturation profiles at $T_{\text{PVI}} = 0.06$ (before breakthrough) on the high-contrast permeability field that combines a high permeability channel and a low permeability region. Left column, top to bottom: reference fine grid solution; MRCM-usual saturation profile; MMMFEM-like saturation profile. Right column, top to bottom: MSFV saturation profile; MRCM-naive saturation profile; MHM-like saturation profile. The only procedure that produces a saturation solution close to the reference run is the MRCM-naive.

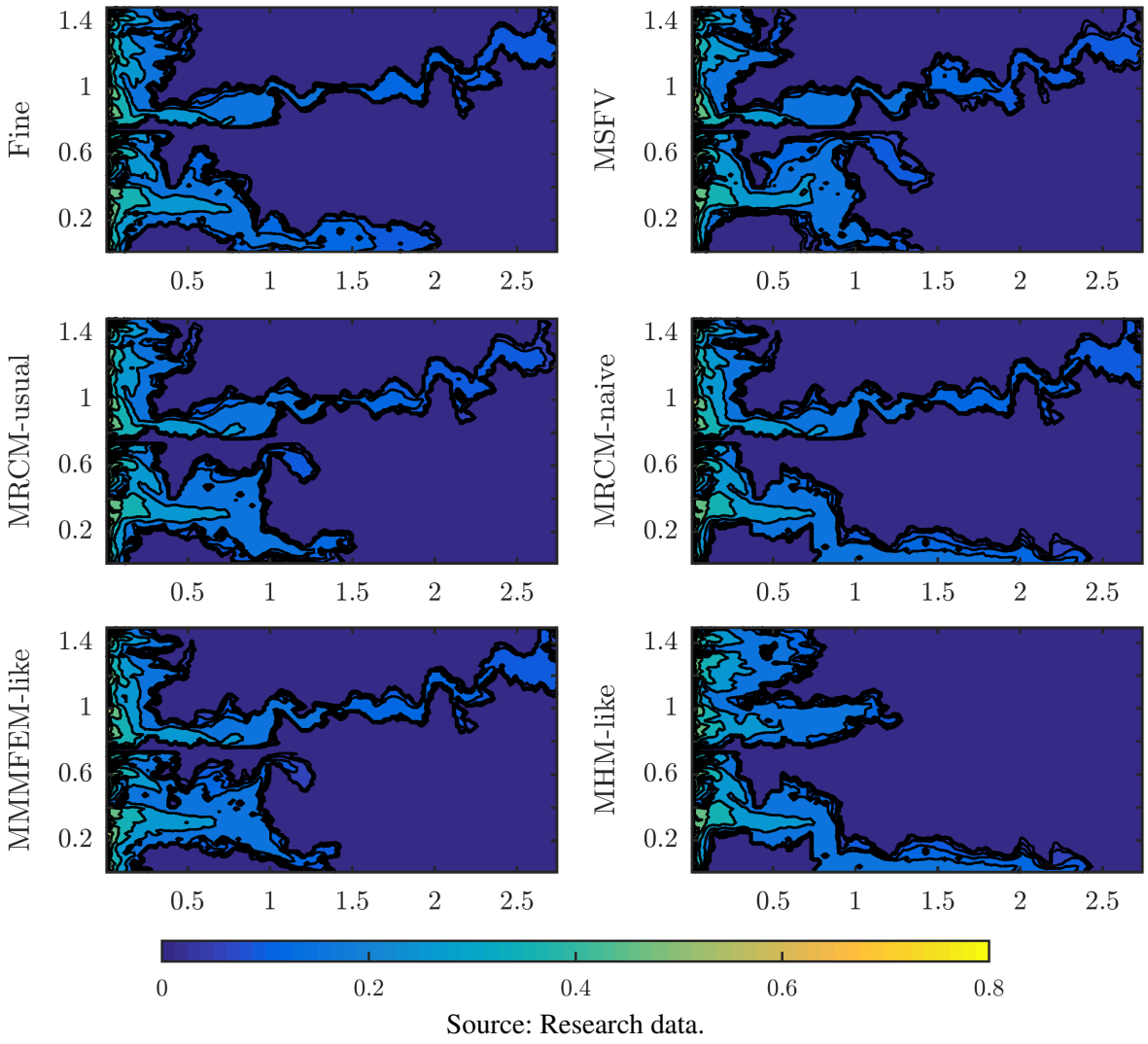

Source: Research data.

Figure 16 – Saturation profiles at $T_{\text{PVI}} = 0.5$ on the high-contrast permeability field that combines a high permeability channel and a low permeability region. Left column, top to bottom: reference fine grid solution; MRCM-usual saturation profile; MMMFEM-like saturation profile. Right column, top to bottom: MSFV saturation profile; MRCM-naive saturation profile; MHM-like saturation profile. We note that the MRCM-naive approximation is the only method that produces a solution close to the reference saturation map after the breakthrough.

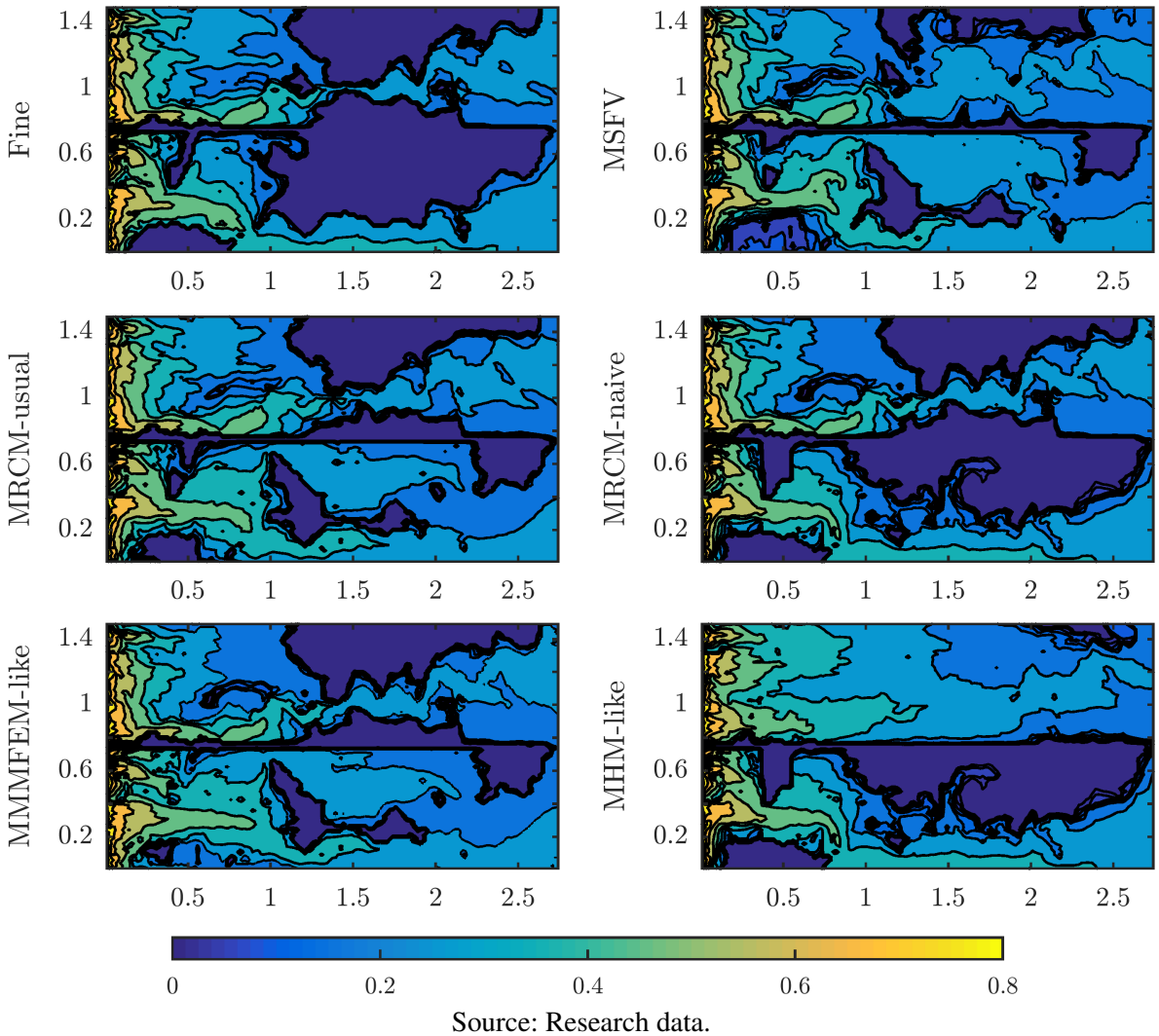

Source: Research data.

Figure 17 – Choice of the parameter α on subdomain boundaries for the MRCM-adaptive. The red color considers the MMMFEM-like method ($\alpha = 10^{-8}$) on the subdomain boundaries that are in regions of high permeability. The cyan color considers the MHM-like method ($\alpha = 10^{8}$) on the remaining subdomain boundaries. We compare four possibilities for cutoff value ζ. Left column, top to bottom: $\zeta = 10^{0}$; $\zeta = 10^{2}$. Right column, top to bottom: $\zeta = 10^{1}$; $\zeta = 10^{3}$. The high permeability channel structure is well captured for $\zeta = 10^{1}$ or $\zeta = 10^{2}$.

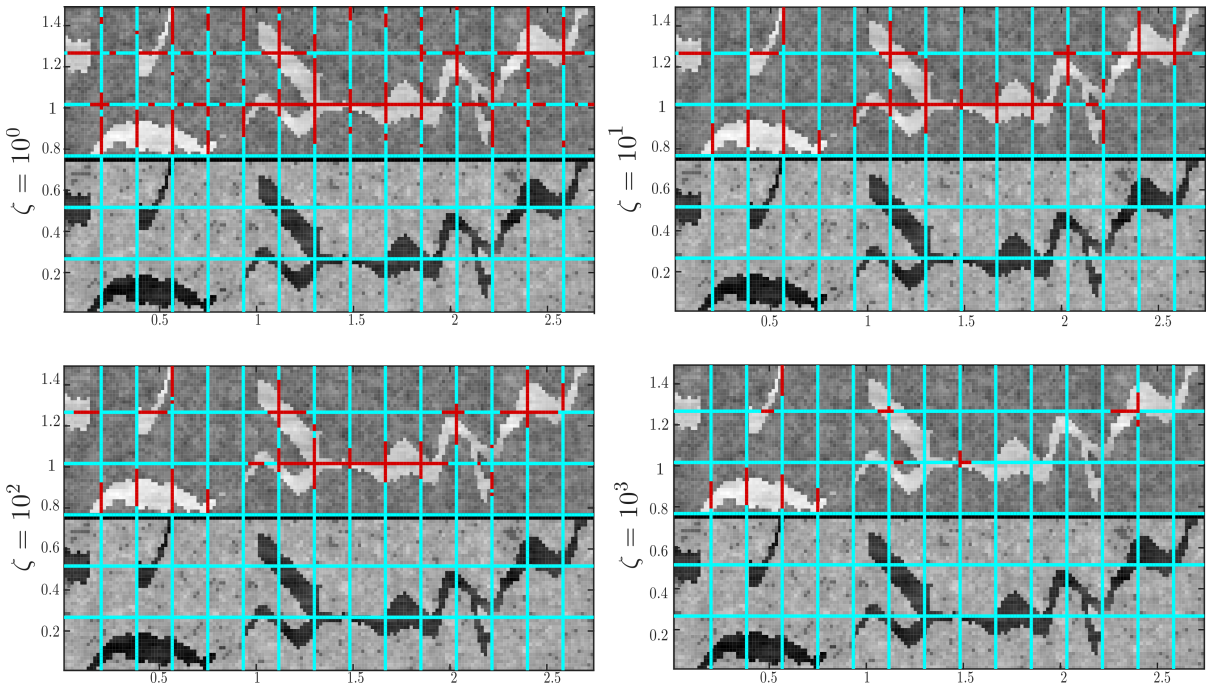

Source: Research data.

Figure 18 – Comparison of the saturation solutions calculated with the different versions of the MRCM on the high-contrast permeability field that combines a high permeability channel and a low permeability region. Saturation profiles at $T_{\mathrm{PVI}} = 0.06$ (before breakthrough) are shown. Left column, top to bottom: reference fine grid solution; MRCM-naive saturation profile. Right column, top to bottom: MRCM-usual saturation profile; MRCM-adaptive saturation profile. The MRCM-naive and MRCM-adaptive provide more accurate solutions than the MRCM-usual.

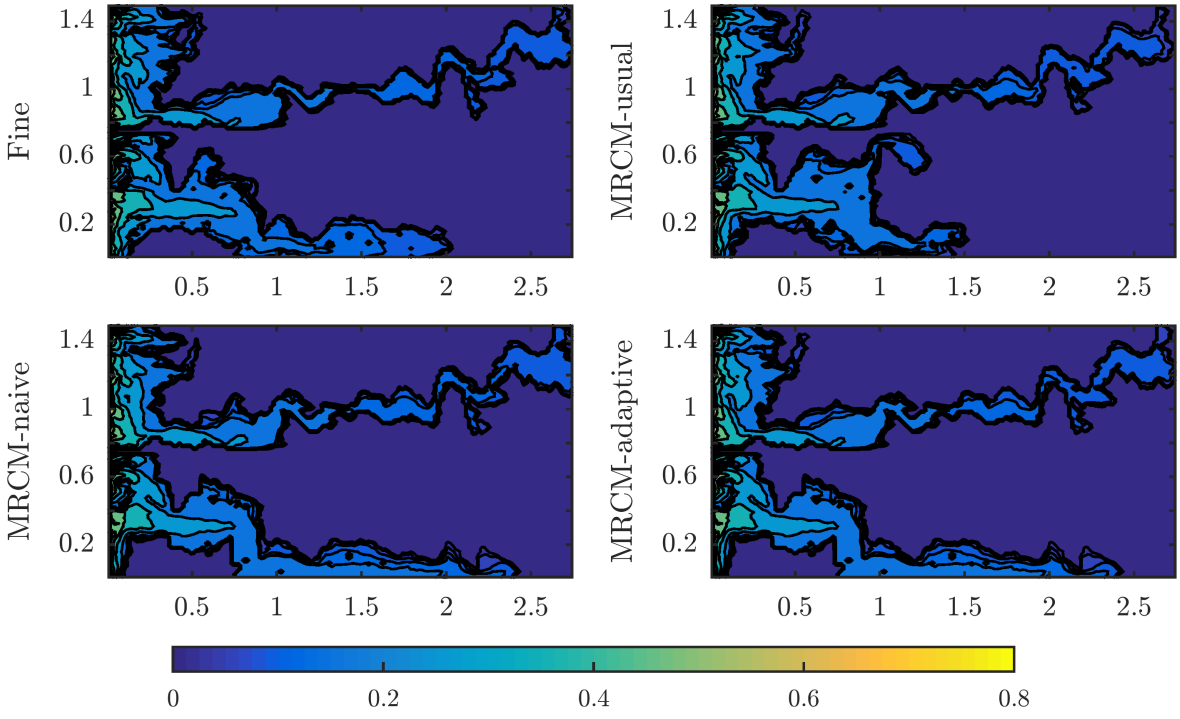

Source: Research data.

Figure 19 – Comparison of the saturation solutions calculated with the different versions of the MRCM on the high-contrast permeability field that combines a high permeability channel and a low permeability region. Saturation profiles at $T_{\text{PVI}} = 0.5$ are shown. Left column, top to bottom: reference fine grid solution; MRCM-naive saturation profile. Right column, top to bottom: MRCM-usual saturation profile; MRCM-adaptive saturation profile. The MRCM-naive and MRCM-adaptive results remain more accurate than the MRCM-usual after breakthrough.

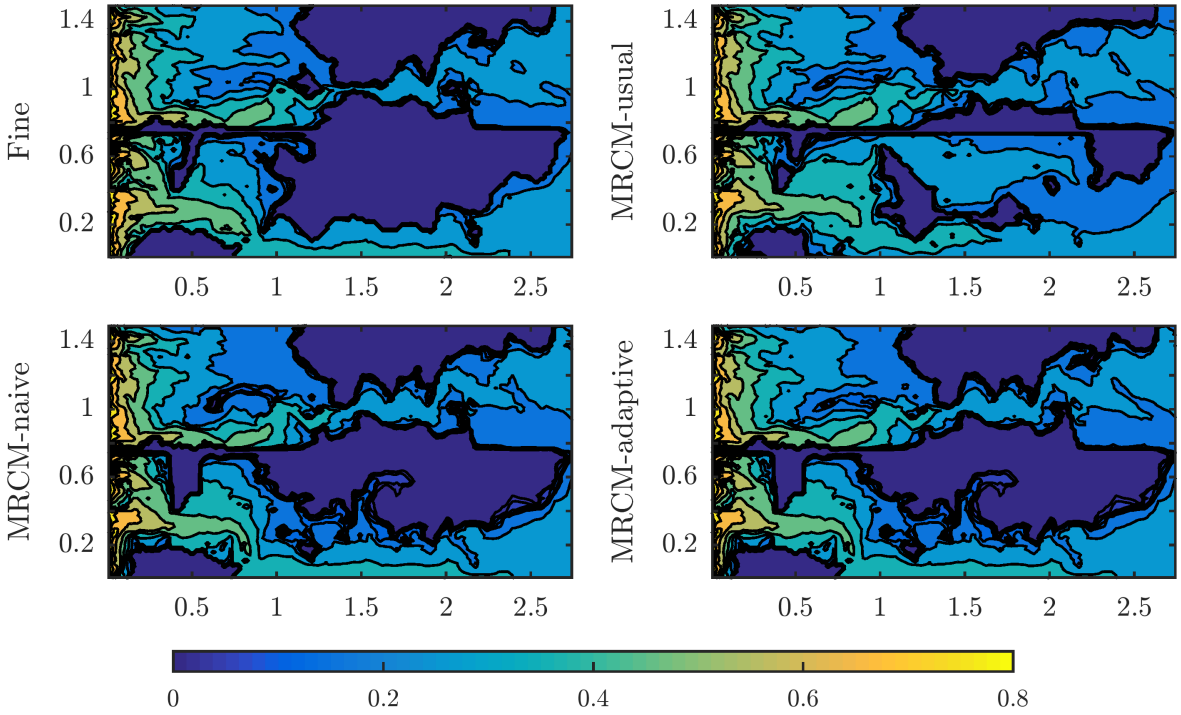

Source: Research data.

Figure 20 – Oil production curve (left) and relative $L^1(\Omega)$ errors for saturation (right) on the built permeability field as function of time. The breakthrough time is illustrated by dashed line (right plot). We note that the best approximations of oil production curves are performed by the MRCM-naive and MRCM-adaptive. The MRCM-adaptive produces the smallest saturation errors.

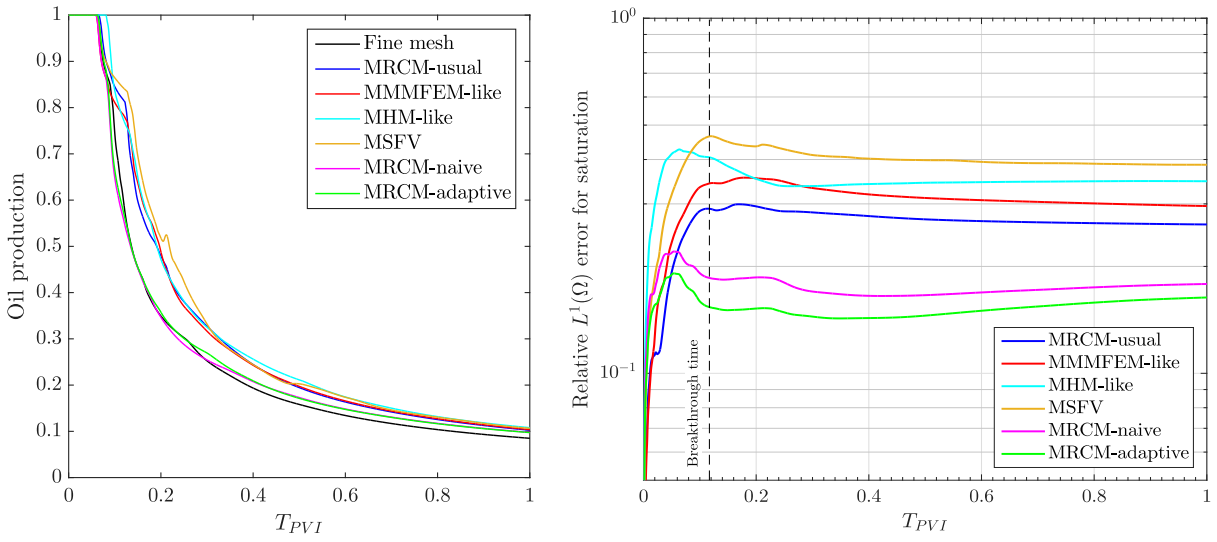

Source: Research data.

CHAPTER

4

INTERFACE SPACES BASED ON PHYSICS

The multiscale approaches solve the problem on a coarse decomposition of the domain, incorporating the fine-grid information through local basis functions. The accuracy of the multiscale methods is related to the calculation of the basis functions. If the heterogeneities are not well represented by the basis, inaccurate solutions are obtained. Spaces that are polynomial on the interfaces of the domain decomposition work well for smooth or Gaussian permeability fields, but their performance for high contrast, channelized ones is not satisfactory (CHUNG; EFENDIEV; LI, 2014; CHUNG; FU; YANG, 2016; CORTINOVIS; JENNY, 2014; GUIRALDELLO *et al.*, 2019). To remedy this, informed spaces obtained from sets of snapshots by algebraic dimensionality reduction were considered in (EFENDIEV; GALVIS; HOU, 2013; CHUNG; FU; YANG, 2016; GUIRALDELLO *et al.*, 2019). Another approach is to define the interface space through eigensolutions of local partial-differential problems (MADUREIRA; SARKIS, 2017). These approaches can also be coupled to a-posteriori error estimators (CHUNG; EFENDIEV; LI, 2014; CHUNG; EFENDIEV; LEUNG, 2017; CHUNG; PUN, 2019).

Other authors have looked for approaches more directly based on the geometry of the heterogeneities. In (AARNES; KROGSTAD; LIE, 2006; MØYNER; LIE, 2016; KLEMETSDAL; MØYNER; LIE, 2019), for example, the authors consider polynomial bases but adapt the grid to the geological properties, while in (PESZYŃSKA; WHEELER; YOTOV, 2002; CORTINOVIS; JENNY, 2014; CORTINOVIS; JENNY, 2017) local enrichment functions were added on high-permeability regions. These geometrical strategies are well suited for permeability fields containing either channels or barriers, but not both. In this chapter, we propose a strategy to deal with the simultaneous presence of channels and barriers, since such situation is not unfrequent in reservoir simulation (HOSSEINIMEHR *et al.*, 2019). For this purpose, we use the MRCM for the independent choice of the pressure and flux interface spaces. In fact, the pressure space is designed so as to accommodate channels and the flux space to accommodate barriers, and the adaptivity of the MRCM is used to automatically select the appropriate parameters at each location.

Our intention is to use high-definition volumetric grids that capture the large scale features of the fracture network, especially when they are relatively large as happens in fractured karst reservoirs (BAOMIN; JINGJIANG, 2009; POPOV *et al.*, 2009; HUANG; YAO; WANG, 2013; LOPES *et al.*, 2019). Typically, fractures are handled with separate discrete models that represent the fractures as lower-dimensional objects so as to incorporate sub-grid resolution (MARTIN; JAFFRÉ; ROBERTS, 2005; REICHENBERGER *et al.*, 2006; FORMAGGIA *et al.*, 2014; SCHWENCK *et al.*, 2015; BERKOWITZ, 2002; FLEMISCH *et al.*, 2018). A popular approach is the Discrete Fracture Model (DFM) which uses unstructured grids to place fractures at the interface between matrix cells (KIM; DEO, 2000; KARIMI-FARD; DURLOFSKY; AZIZ, 2003; HOTEIT; FIROOZABADI, 2008). Other approaches are the Embedded DFM (TENE; KOBAISI; HAJIBEYGI, 2016; CHAI *et al.*, 2018), the multi-continuum model (CHUNG *et al.*, 2017; WANG *et al.*, 2020) and the hierarchical fracture models (HAJIBEYGI; KARVOUNIS; JENNY, 2011; LI; LEE, 2008; EFENDIEV *et al.*, 2015).

Since it is possible to combine discrete models with multiscale methods (BOSMA *et al.*, 2017; ZHANG *et al.*, 2017; DEVLOO; TENG; ZHANG, 2019; XIA *et al.*, 2018), the final goal of the improved MRCM proposed here is to allow a unified treatment of fractured karst reservoirs in which the modeling of the fractures is shared, depending on the fracture's size, between the volumetric grid and the discrete models. For this reason, we consider here permeability fields containing multiple narrow and relatively straight features (channels, barriers) that mimic the largest structures of a fractured porous medium.

In the next section, the strategies for building the physics-based interface spaces are presented along with some numerical experiments. Then, we explain our proposed combination of the physics-based spaces with the adaptive MRCM in section 4.2, followed by numerical results and discussions.

4.1 Physics-based interface spaces

The interface spaces $\mathscr{U}_H$ and $\mathscr{P}_H$ for the MRCM were setting as low-dimensional polynomial spaces in (GUIRALDELLO *et al.*, 2018) and informed spaces in (GUIRALDELLO *et al.*, 2019). However, low-dimensional polynomial spaces are not robust to represent variations of high-contrast permeability fields containing structures as high permeability channels and barriers. Even informed spaces with a low number of degrees of freedom are not enough. To better represent the variations of channelized permeability fields we present two physics-based interface spaces. The idea is to build the multiscale basis functions based on the pressure and flux solutions at each structure (channel/barrier). We present one space for pressure and another for flux. The new pressure space is suited for high permeability channels, whereas the new flux space for barriers or low permeability barriers, that cross the interface between subdomains.

The support of the new basis functions are the interfaces that contain channelized

structures. In the remaining interfaces the spaces can be freely chosen (any low-dimensional polynomial or informed spaces). We denote $(\mathscr{U}_{H,k}, \mathscr{P}_{H,k})$ the choice of the interface spaces made up of the elementwise constant fine grid representation of polynomials over the interface elements, where k is the degree of the polynomial. To introduce the concept we consider, for simplicity, the linear spaces $(\mathscr{U}_{H,1}, \mathscr{P}_{H,1})$ for both flux and pressure. This choice of interface spaces is used further in the numerical section. The basis of these spaces contain $k_U = 2$ and $k_P = 2$ functions on each interface between two subdomains. If the permeability field contains high-permeable structures passing through the interface we propose to replace the space $\mathscr{P}_{H,1}$ by the physics-based pressure space. On the other hand, if the permeability filed contains barriers crossing the interface we replace the space $\mathscr{U}_{H,1}$ by the physics-based flux space. In the following subsections, we describe how the physics-based interface spaces are built for capturing the high-contrast structures.

4.1.1 A physics-based interface space for the pressure

We define a simplified problem test to show the behavior of the solution to define the interface spaces. In Figure 21 we consider a high-contrast permeability field containing a vertical high-permeable structure (Figure 21a). We show the pressure (Figure 21b) and flux (Figure 21c) fine grid solutions. Here we consider a single-phase model, where the flow is established by imposing a flux boundary condition from left to right and no-flow at top and bottom. This geometry induces a one-dimensional pressure solution which is plotted along a horizontal line in Figure 21d. Notice, the pressure is essentially constant over the high-permeable region. Any domain decomposition with more than one subdomain in the y-direction contains horizontal interfaces through which the high-permeable structure passes. Let Γ^{high} be the set of all interfaces that contain at least one fine cell in which the permeability is larger than a cutoff value ζ_{max}. We intend to replace the pressure linear space $\mathscr{P}_{H,1} = \text{span}\{\psi_1, \psi_2\}$ at the interfaces $\Gamma_{i,j} \subset \Gamma^{\text{high}}$ by a physics-based pressure space, denoted by $\mathscr{P}^*_H$.

Figure 21 – Problem with a vertical high-permeable structure. (a) Permeability field (log-scaled) containing a vertical high-permeable structure. (b) Pressure field. (c) Flux. The colors in the flux plot refer to the log-scale flux magnitude. (d) Pressure along a horizontal line.

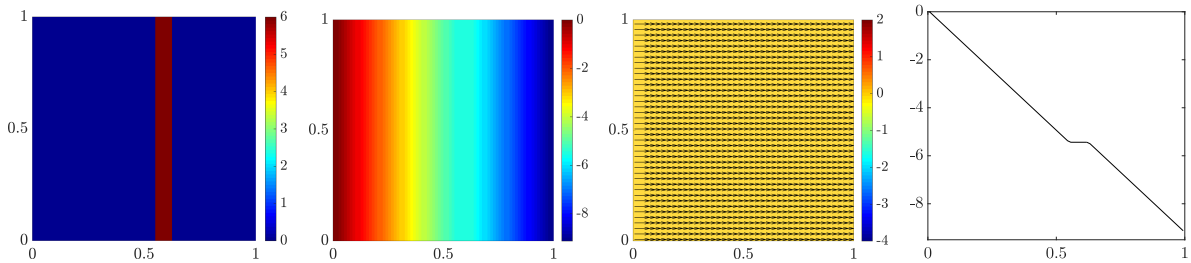

(a) Permeability (b) Pressure (c) Flux (d) Pressure profile

Source: Research data.

The new pressure space mimics the behavior of the pressure across the high-permeable structures. Let $\Gamma_{i,j} \subset \Gamma^{\text{high}}$ be an interface with support in $[a,d]$ through which a high-permeable structure passes in $[b,c] \subset [a,d]$, as sketched in Figure 22. The basis functions are defined as:

$$\psi_1^*(x) = \begin{cases} \dfrac{b-x}{b-a} & \text{if } x \in (a,b) \\ 0 & \text{otherwise} \end{cases} \tag{4.1}$$

$$\psi_2^*(x) = \begin{cases} \dfrac{x-a}{b-a} & \text{if } x \in (a,b) \\ 1 & \text{if } x \in (b,c) \\ \dfrac{d-x}{d-c} & \text{if } x \in (c,d) \end{cases} \tag{4.2}$$

$$\psi_3^*(x) = \begin{cases} \dfrac{x-c}{d-c} & \text{if } x \in (c,d) \\ 0 & \text{otherwise} \end{cases} . \tag{4.3}$$

The new interface pressure space is then defined as $\mathscr{P}_H^* = \text{span}\{\psi_1^*, \psi_2^*, \psi_3^*\}$ at $\Gamma_{i,j} \subset \Gamma^{\text{high}}$. Since the definition of the basis depends only on the fine-grid discretization of the permeability at the interface, any high-permeable structure crossing the interface can be represented. Therefore, these basis functions are not restricted to structures orthogonal to the interface. If the interface contains more than one high-permeable structure we need to define a new basis function with similar behavior to the ψ_2^* for each structure. The total number of basis functions per interface is thus $2 + N_{\text{high}}$, where N_{high} is the number of high-permeable structures at the interface.

Figure 22 – Physics-based basis functions for pressure at the interfaces that contain high-permeable structures. Note that the set of functions is able to capture the pressure profile across the structure.

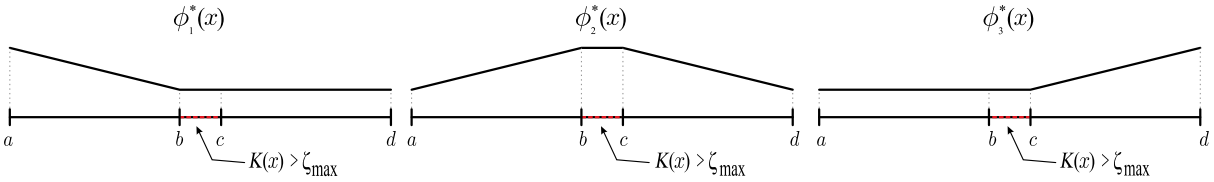

Source: Research data.

In Figure Figure 23, we show the pressure solution at the horizontal line $y = 0.49$ delivered by the MMMFEM (by setting the α parameter of the MRCM to the value 10^{-6}) in a domain decomposition with 2×2 coarse cells. We denote by MMMFEM-PBS the multiscale method combined with the physics-based spaces and by MMMFEM-POL the multiscale method combined with polynomial spaces (linear in this thesis). We note that for both single (Figure 23a and Figure 23c) and multiple (Figure 23b and Figure 23d) high-permeable structures the correct pressure solution is only captured by the MMMFEM combined with physics-based interface spaces.

Figure 23 – High-contrast permeability field (log-scaled) with one (a) and two high-permeable structures (c). Pressure solutions for one (b) and two high-permeable structures (d) computed by the fine-grid solver and the multiscale ones MMMFEM-POL and MMMFEM-PBS. We note that for both one and two high-permeable structures the correct pressure solution is only captured by the MMMFEM-PBS.

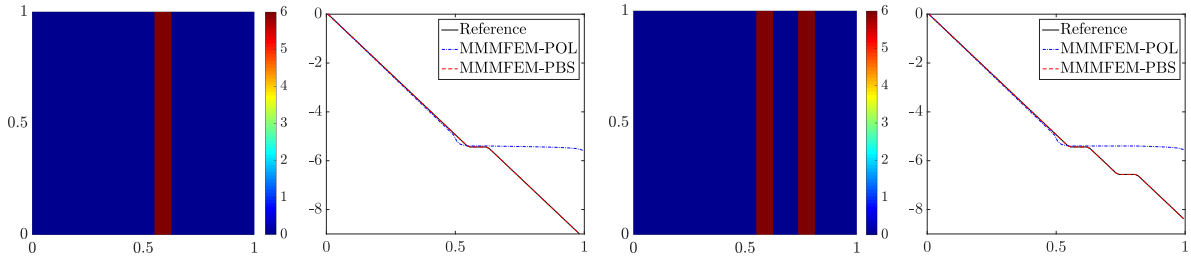

(a) Permeability (b) Pressure (c) Permeability (d) Pressure

Source: Research data.

4.1.2 A physics-based interface space for the flux

Now we focus on fields containing low-permeable structures. Once again we define a simplified problem to motivate the interface spaces. In Figure 24a we consider a high-contrast permeability field containing a horizontal barrier. We show the fine grid solutions for pressure (Figure 24b) and for flux (Figure 24c). Here the flow is established by imposing a pressure gradient from left to right and no-flow at top and bottom. The x-component of the flux along a vertical line is illustrated in Figure 24d, showing the discontinuities at the locations of transitions to barrier regions. Any domain decomposition with more than one subdomain in x-direction contains vertical interfaces through which the low-permeable structure passes. Let Γ^{low} be the set of all the interfaces that contain at least one fine cell in which the permeability is lower than a cutoff value ζ_{min}. We introduce the new flux spaces $\mathcal{U}_H^*$ according to the behavior of the flux solution by replacing the flux linear spaces $\mathcal{U}_{H,1} = \text{span}\{\phi_1, \phi_2\}$ at the interfaces $\Gamma_{i,j} \subset \Gamma^{\text{low}}$.

Figure 24 – Horizontal barrier problem. (a) Permeability field (log-scaled) containing a horizontal barrier. (b) Pressure field. (c) Flux. The colors in the flux plot refer to the log-scale flux magnitude. Additionally, the x-component solution of the flux along a vertical line is illustrated in (d), where we note that the flux is discontinuous at the transitions to barrier regions.

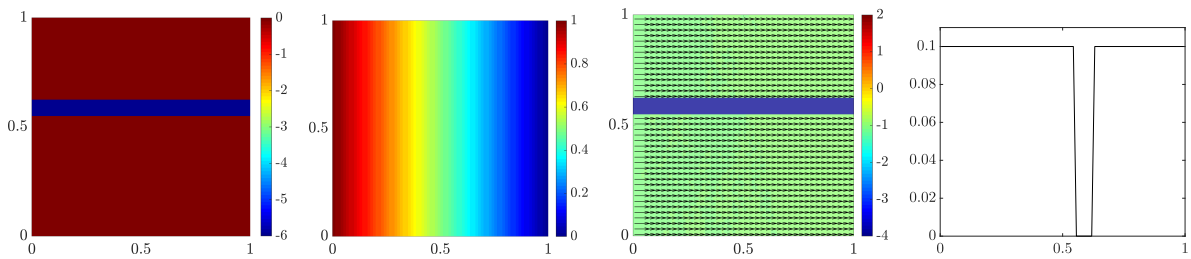

(a) Permeability (b) Pressure (c) Flux (d) Flux profile

Source: Research data.

Let $\Gamma_{i,j} \subset \Gamma^{\text{low}}$ be an interface with support in $[a,d]$ through which a barrier passes in $[b,c] \subset [a,d]$, as sketched in Figure 25. We define the following basis functions:

$$\phi_1^*(x) = \begin{cases} 1 & \text{if } x \in (a,b) \\ 0 & \text{otherwise} \end{cases} \tag{4.4}$$

$$\phi_2^*(x) = \begin{cases} 1 & \text{if } x \in (b,c) \\ 0 & \text{otherwise} \end{cases} \tag{4.5}$$

$$\phi_3^*(x) = \begin{cases} 1 & \text{if } x \in (c,d) \\ 0 & \text{otherwise} \end{cases} . \tag{4.6}$$

The new interface space is defined as $\mathscr{U}_H^* = \text{span}\{\phi_1^*, \phi_2^*, \phi_3^*\}$ at $\Gamma_{i,j}^{\text{low}}$. These basis functions are not restricted to barriers orthogonal to the interface, similar to the pressure basis. If the interface contains more than one barrier we need to define a new basis function with behavior similar to that of the ϕ_2^* for each barrier, plus a constant function for each region between two barriers. The total number of basis functions per interface is thus $1 + 2N_{\text{low}}$, where N_{low} is the number of barriers.

Figure 25 – Physics-based basis functions for flux at the interfaces that contain barriers.

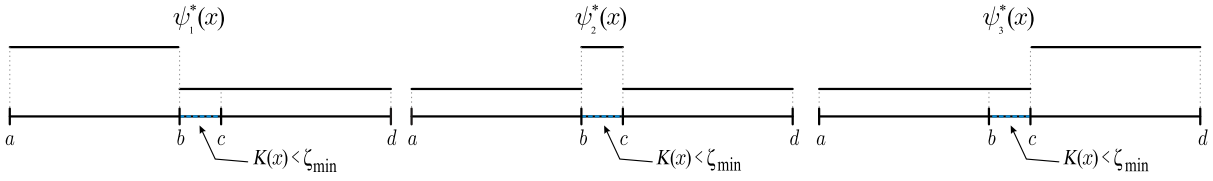

Source: Research data.

In Figure 26 we show the x-component of the flux along $x = 0.5$ provided by the MHM (by setting the α parameter of the MRCM to the value 10^6) in a domain decomposition with 2×2 coarse cells. We compare the approximations provided by the MHM-POL (MHM combined with the linear spaces) and MHM-PBS (MHM combined with the physics-based spaces) with the fine-grid solution. We note that for both single (Figure 26a and Figure 26c) and multiple (Figure 26b and Figure 26d) barriers the correct x-component of the flux is only captured by MHM-PBS.

4.1.3 Experiments with the physics-based interface spaces

The examples in Figure 23 and Figure 26 illustrate that the usual linear interface spaces fail to approximate the solution in the presence of high-permeable structures and barriers even for simple problems. The proposed physics-based spaces have been able to represent the behavior of the solution in those problems. In this subsection, we show that the physics-based spaces work well also in slightly more complex permeability fields. Initially, we consider a permeability field with high permeability channels and use the physics-based pressure space combined with the

Figure 26 – High-contrast permeability field (log-scaled) with one (a) and two barriers (c). Fine-grid reference, MHM-POL and MHM-PBS solutions for the x-component of the flux considering one (c) and two barriers (d). Notice that for both one and two barriers the correct x-flux solution is only captured by the MHM-PBS.

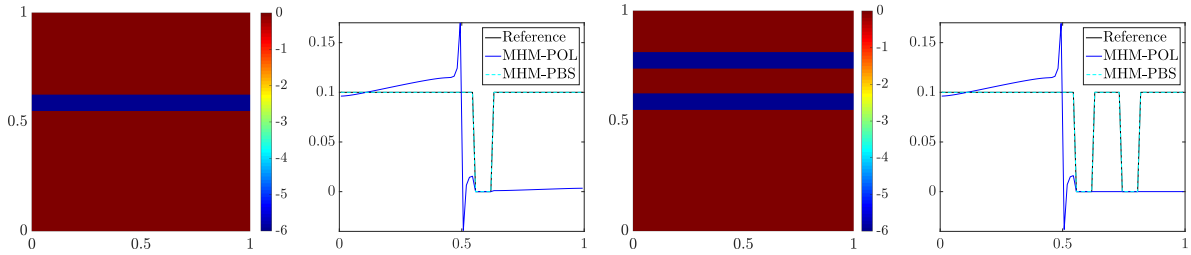

(a) Permeability (b) Flux (c) Permeability (d) Flux

Source: Research data.

MMMFEM. Then we consider a permeability field with barriers and use the physics-based flux space combined with the MHM.

4.1.3.1 The MMMFEM for permeability fields with high permeability channels

The first study considers a permeability field containing high permeability channels. In this case, the physics-based pressure space is applied to the interfaces that contain cells in which the permeability is larger than a cutoff value $\zeta_{\max}$. We combine the new interface space with the MMMFEM. We consider the permeability in the high-permeable structure, $K_{\max}$ varying from 10 to 10^8 whereas the background is homogeneous with $K = 1$, see Figure 27a. The cutoff value set to capture the high-permeable structures is $\zeta_{\max} = 1$ in all cases. The domain considered is $\Omega = [0,1] \times [0,1]$ containing 160×160 cells. In Figure 27b we show the relative $L^2(\Omega)$ errors for pressure as function of the permeability contrast. Three domain decompositions are considered: 4×4, 8×8 and 16×16 coarse cells, each one containing, respectively 40×40, 20×20 and 10×10 fine cells. The boundary conditions in the simulations of this subsection are no-flow at the top and bottom boundaries along with an imposed flux on the left and right boundaries. No source terms are considered. We compare the multiscale solution considering the usual linear polynomial (MMMFEM-POL) and the physics-based (MMMFEM-PBS) pressure interface spaces. We note that for permeability contrasts larger than 100 the improvement with the physics-based spaces is significant for all the domain decompositions considered. Domain decompositions with more subdomains present smaller errors. Figure 28 shows the pressure approximations for the decomposition of 8×8 coarse cells in the highest permeability contrast $K_{\max}/K_{\min} = 10^8$. It is clear that the imprecisions of the MMMFEM solution with the linear interface spaces are corrected with the use of the physics-based ones.

Figure 27 – High-contrast permeability field with high permeability channels (a). We consider the permeability in the channel, $K_{\max}$ varying from 10 to 10^8 whereas the background is homogeneous with $K = 1$. Relative $L^2(\Omega)$ pressure errors as function of the contrast are shown for the MMMFEM-POL and MMMFEM-PBS (b). Three domain decompositions are considered: with 4×4, 8×8 and 16×16 coarse cells. We note a significant improvement for the MMMFEM-PBS in all the meshes, especially for high-contrast.

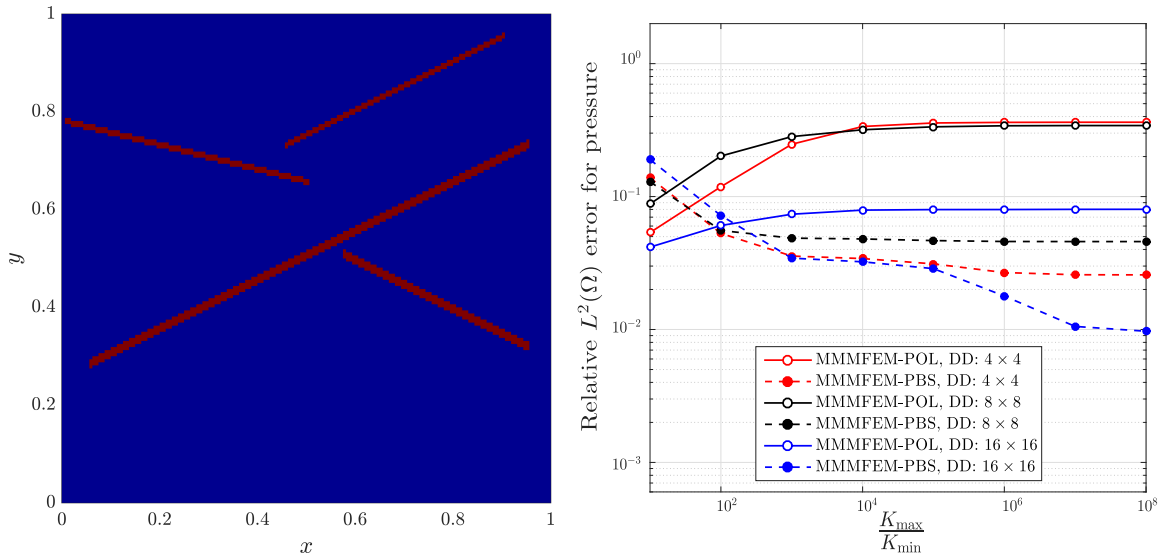

(a) Permeability (b) Pressure errors

Source: Research data.

Figure 28 – Pressure approximations considering the contrast of $K_{\max}/K_{\min} = 10^8$. Left to right: fine mesh, MMMFEM-POL, and MMMFEM-PBS solutions. The domain decomposition considered contains 8×8 coarse cells and is illustrated by the lines in the plot. We note that the MMMFEM-PBS solution is more accurate than the MMMFEM-POL.

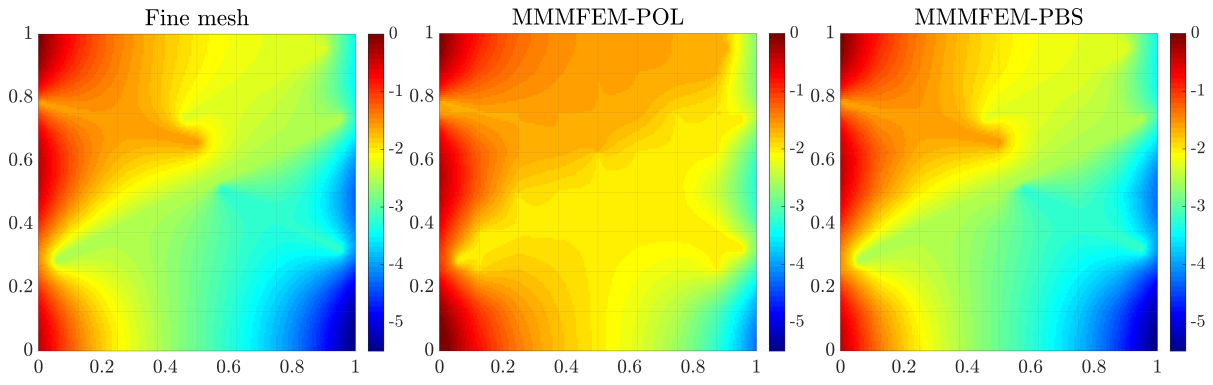

Source: Research data.

4.1.3.2 *The MHM for permeability fields with barriers*

In the next experiment, the same problem of the previous subsection is considered, except that the high permeability channels are replaced by barriers of low permeability. The physics-based flux space is used at interfaces that contain cells in which the permeability is lower than a cutoff value $\zeta_{\min}$. We combine the flux space with the MHM to approximate the

solution. Similar to the previous example, we compare different permeability contrasts. Here, we consider the permeability in the barrier, K_{min} varying from 10^{-8} to 10^{-1} whereas the background is homogeneous with $K = 1$, see Figure 29a. The cutoff value set to capture the barriers is $\zeta_{\text{min}} = 1$ in all cases. The relative $L^2(\Omega)$ errors for flux as function of the contrast are displayed in Figure 29b. Similar to the previous case, the solution is more accurate by using the physics-based space instead of the linear space. The flux errors provided by the linear spaces increase quickly with the contrast whereas the errors from the physics-based spaces are controlled. The results are consistent for the three domain decompositions, where the smaller errors are provided by the decompositions with more subdomains. In Figure 30 we show the flux approximations for the decomposition of 8×8 coarse cells in the highest permeability contrast $K_{\text{max}}/K_{\text{min}} = 10^8$. We note that the MHM-POL solution is inaccurate and the MHM-PBS approximation captures the correct behavior of the reference solution.

Figure 29 – High-contrast permeability field with barriers (a). We consider the permeability in the barrier, K_{min} varying from 10^{-8} to 10^{-1} whereas the background is homogeneous with $K = 1$. Relative $L^2(\Omega)$ flux errors as function of the contrast are shown for the MHM-POL and MHM-PBS (b). Three domain decompositions are considered: with 4×4, 8×8 and 16×16 coarse cells. We note that for high-contrast the only accurate approximations are produced by the MHM-PBS (in all the meshes).

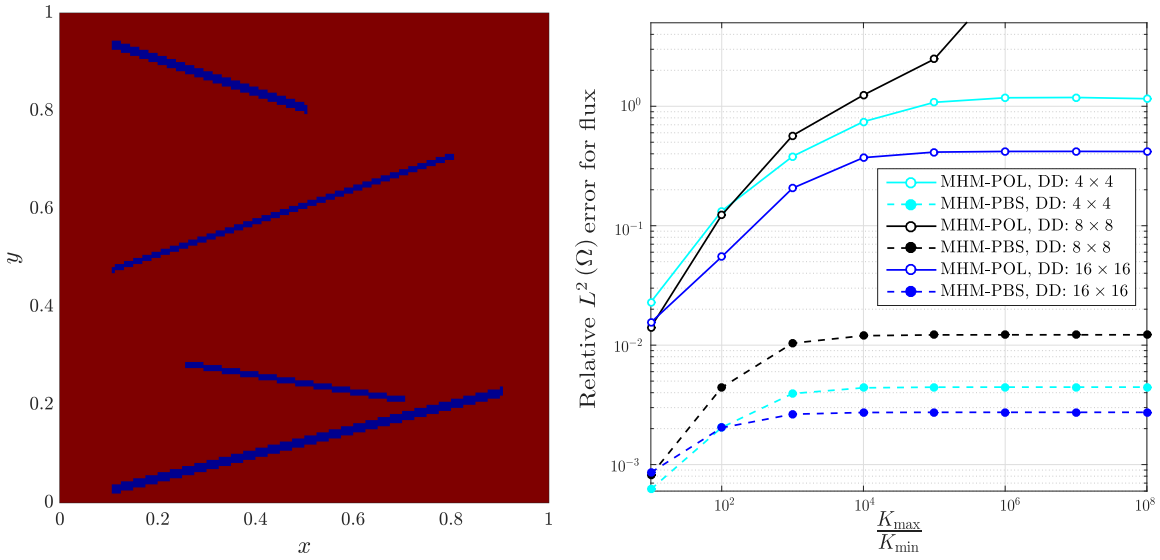

(a) Permeability

(b) Flux errors

Source: Research data.

4.2 Adaptive MRCM with the physics-based interface spaces

We can conclude from the numerical studies reported above that the physics-based pressure (respectively, flux) space is fundamental to produce an accurate pressure (resp., flux)

Figure 30 – Flux approximations considering the contrast of $K_{\max}/K_{\min} = 10^8$. Left to right: fine mesh, MHM-POL, and MHM-PBS solutions. The colors in the flux plot refer to the log-scale flux magnitude. The domain decomposition considered contains 8×8 coarse cells and is illustrated by the lines in the plot. We note that the MHM-PBS approximation is closely related to the reference solution and the MHM-POL is inaccurate.

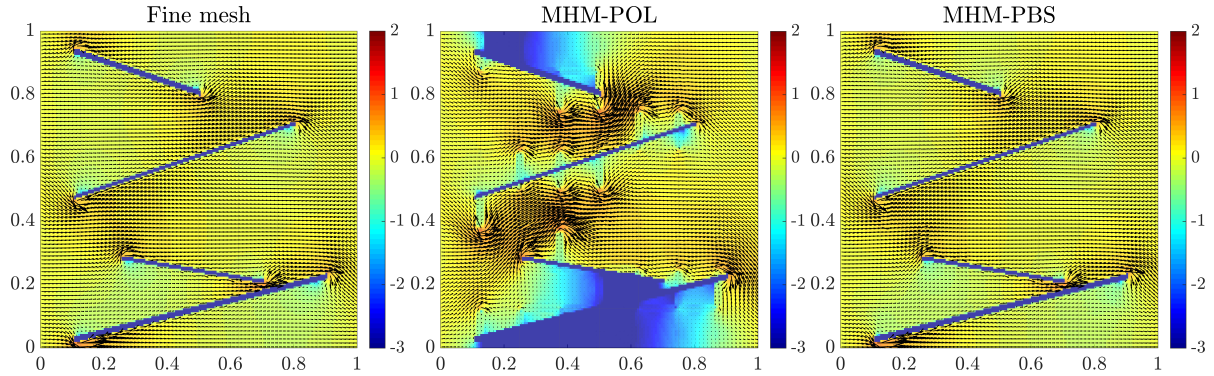

Source: Research data.

solution in presence of high permeability channels (resp., barriers). Therefore if high permeability channels and barriers appear in a single interface one can achieve a better approximation of pressure and flux using both pressure and flux physics-based interface spaces. To attain this goal one feature necessary for the multiscale method used is the ability to include the interface spaces independently. For this purpose, we combine the physics-based interface spaces with the MRCM, whose formulation enables to include the spaces separately. In the MRCM framework, we consider the adaptive version (denoting by *a*MRCM) that consists of setting the function $\alpha(\mathbf{x})$ depending on the variation of the permeability field at the interfaces. In line with the previous chapter, we take a small value α_{small} (pressure is favored) for regions where the permeability is larger than a cutoff parameter, and a large value α_{large} (flux is favored) for the remaining areas. In this sense, the *a*MRCM controls the relative importance of each interface space at each location.

To solve Equation (2.1) by the MRCM we need to set the interface parameters (i.e., the interface spaces and the adaptive function $\alpha(\mathbf{x})$). In Algorithm 2 we detail the preprocessing operations to set the interface spaces and the adaptive coefficient $\alpha(\mathbf{x})$ from the permeability field. At each interface $\Gamma_k,\ k = 1,\cdots,M$ (where M is the total number of interfaces), and at each interface cell $e_l \in \Gamma_k,\ l = 1,\cdots,m_k$ (where m_k is the number of fine cells in Γ_k), it is defined whether e_l corresponds to a high permeability channel, a barrier, or to background, and then $\alpha(\mathbf{x}_l)$ (at the cell's center) is set accordingly. Then, we use the proposed physics-based interface spaces taking into account the observations presented in the previous section. We set the interface pressure (resp., flux) spaces as $\mathscr{P}^*_{H,1}$ (respectively, $\mathscr{U}^*_{H,1}$), that consider the physics-based space for the interfaces containing high permeability channels (resp., barriers) and linear spaces for the remaining interfaces. Finally we are able to combine the *a*MRCM with the physics-based spaces $(\mathscr{U}^*_{H,1}, \mathscr{P}^*_{H,1})$. We refer to this combination as *a*MRCM-PBS and consider for comparisons, the *a*MRCM-POL, which represents the *a*MRCM combined with linear polynomial spaces

independently on the permeability field. We remark that the *a*MRCM can deal with one high-permeable structure per interface, and hence, we use the pressure physics-based space only at the interfaces that contain more than one high-permeable structure.

Algorithm 2 – Setting interface parameters for solving Equation (2.1) by the *a*MRCM-PBS

Given $K(\mathbf{x})$, ζ_{min}, ζ_{max}, α_{small} and α_{large}
for $k \in \{1, \cdots, M\}$ **do**
  for $l \in \{1, \cdots, m_k\}$ **do**
    Evaluate the permeability in both sides ($K^-(\mathbf{x}_l)$ and $K^+(\mathbf{x}_l)$) of the interface cell $e_l \in \Gamma_k$
    if $(\max\{K^-(\mathbf{x}_l), K^+(\mathbf{x}_l)\} > \zeta_{\text{max}})$ **then**
      $\alpha(\mathbf{x}_l) = \alpha_{\text{small}}$
      Add Γ_k to Γ^{high}
    else
      $\alpha(\mathbf{x}_l) = \alpha_{\text{large}}$
    end if
    if $(\min\{K^-(\mathbf{x}_l), K^+(\mathbf{x}_l)\} < \zeta_{\text{min}})$ **then**
      Add Γ_k to Γ^{low}
    end if
  end for
  if $(\Gamma_k \subset \Gamma^{\text{high}})$ **then**
    Compute the physics-based functions for pressure from Equations (4.1)-(4.3)
    Set $\mathscr{P}^*_{H,1} = \mathscr{P}^*_H$ at Γ_k
  else
    Compute the linear polynomials functions for pressure
    Set $\mathscr{P}^*_{H,1} = \mathscr{P}_{H,1}$ at Γ_k
  end if
  if $(\Gamma_k \subset \Gamma^{\text{low}})$ **then**
    Compute the physics-based functions for flux from Equations (4.4)-(4.6)
    Set $\mathscr{U}^*_{H,1} = \mathscr{U}^*_H$ at Γ_k
  else
    Compute the linear polynomials functions for flux
    Set $\mathscr{U}^*_{H,1} = \mathscr{U}_{H,1}$ at Γ_k
  end if
end for
Given $(\mathscr{U}^*_{H,1}, \mathscr{P}^*_{H,1})$ and $\alpha(\mathbf{x})$, solve Equation (2.1) to obtain $p(\mathbf{x})$ and $\mathbf{u}(\mathbf{x})$ by the *a*MRCM-PBS

Next, we explore the proposed *a*MRCM-PBS in challenging high-contrast channelized porous media through numerical experiments.

4.3 Numerical experiments

We present representative numerical experiments to investigate the accuracy of the introduced physics-based interface spaces for the approximation of flows in high-contrast channelized porous media. We start with the investigation of the physics-based interface spaces combined

with the *a*MRCM for the elliptic problem. Then we study the influence of the physics-based interface spaces in the approximation of two-phase problems.

In all simulations the fine grid solution is used as the reference solution for evaluating the multiscale approximations. We consider the *a*MRCM (by setting $\alpha_{\text{small}} = 10^{-2}$ and $\alpha_{\text{large}} = 10^{2}$), MMMFEM (by setting $\alpha = 10^{-6}$) and MHM (by setting $\alpha = 10^{6}$). To recover a continuous flux at the fine scale we consider a velocity post-processing (downscaling) (GUIRALDELLO *et al.*, 2020). We choose the Stitch method, which has been indicated as a procedure that provides good compromise between computational cost and precision. The patch thicknesses of the oversampling regions for the Stitch method is fixed in two elements (that represents 10% of the size of most subdomains considered in the examples).

4.3.1 Single-phase flows in permeability fields with high permeability channels and barriers

We consider a permeability field containing both high permeability channels and barriers (see Figure 31) to produce experiments as those presented in subsection 4.1.3. We fix the homogeneous background permeability with $K = 1$ and consider the permeability in the barriers, K_{min} varying from 10^{-4} to 0.5 whereas the permeability in the high permeability channels, K_{max} varying from 10 to 10^{4}. The cutoff values considered are $\zeta_{\text{max}} = \zeta_{\text{min}} = 1$.

Figure 31 – Permeability field containing both high permeability channels (red) and barriers (blue). The contrast considered vary from 10 to 10^{8}.

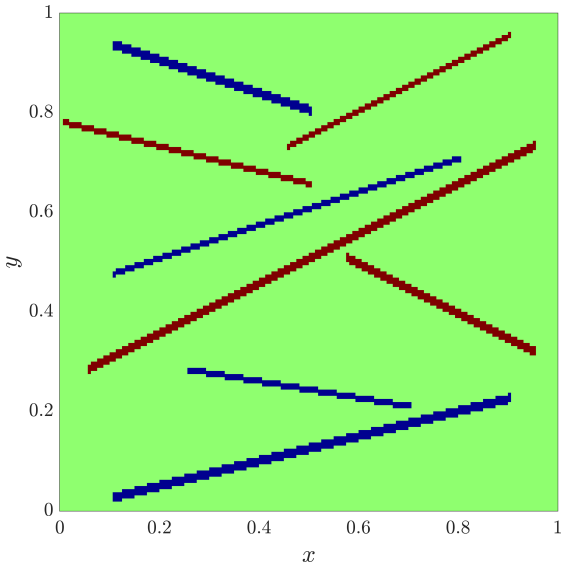

Source: Research data.

The relative $L^2(\Omega)$ error norms for pressure and flux as function of the contrast are shown in Figure 32 for three domain decompositions: with 4×4, 8×8 and 16×16 coarse cells. We observe that the pressure and flux errors related to the linear interface spaces increase quickly with the contrast. However, the errors provided by the physics-based spaces are moderate even

for very large permeability contrasts. The results are consistent for all the domain decomposition tested, where the smaller errors are attained by the decompositions with more subdomains. In Figure 33 we compare the solutions provided by the aMRCM, MMMFEM and MHM considering the domain decomposition of 8×8 subdomains having 20×20 fine cells into each one. The first observation is that the MMMFEM and MHM approximations are not accurate for the permeability field with high permeability channels and barriers even using the physics-based interface spaces. On the other hand, the aMRCM-PBS solutions are expressively more accurate than the ones obtained with the aMRCM-POL. The pressure and flux approximations for the permeability contrast of 10^8 are shown in Figure 34 and Figure 35, respectively. The plots confirm that the aMRCM combined with the physics-based interface spaces produces the most accurate solutions. We observe that all methods fail when using the linear interface spaces. We can conclude that the physics-based interface spaces are indispensable for a reasonable approximation of pressure, flux and further applications in two-phase flows.

Figure 32 – Relative $L^2(\Omega)$ pressure (left) and flux (right) errors as function of the contrast are shown for the aMRCM-POL and aMRCM-PBS. Three domain decompositions are considered: with 4×4, 8×8 and 16×16 coarse cells. We note that the aMRCM-PBS is more accurate than the aMRCM-POL in all the contrast and meshes considered.

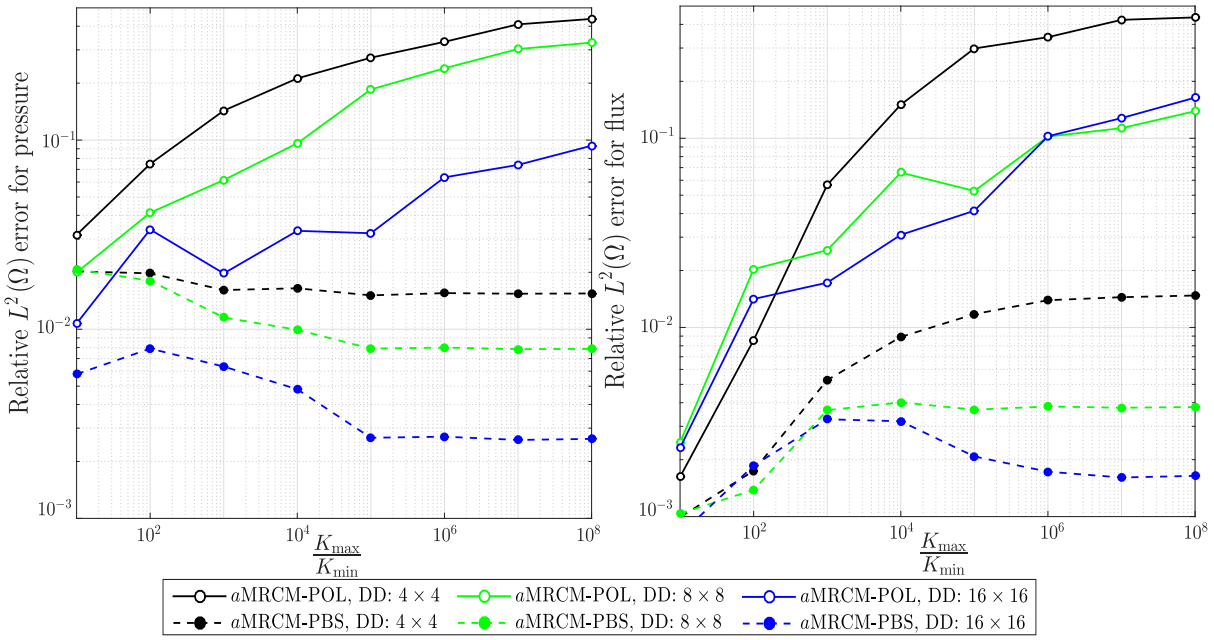

Source: Research data.

Finally, we present in Figure 36 the behavior of the errors for pressure and flux as a function of α (varying from 10^{-6} to 10^6) for the permeability contrast of 10^8 and maintaining the domain decomposition of 8×8 coarse cells. We compare the MRCM errors with linear and physics-based interface spaces. Two choices for the aMRCM are presented: setting $\alpha_{\text{small}} = 10^{-2}$ and $\alpha_{\text{large}} = 10^2$ or $\alpha_{\text{small}} = 10^{-6}$ and $\alpha_{\text{large}} = 10^6$. The errors for the adaptive version of the MRCM are illustrated as horizontal lines. We note a strong dependence on the parameter α, where the minimum errors are attained at intermediate values (for choosing α constant), similarly to

Figure 33 – Relative $L^2(\Omega)$ pressure (left) and flux (right) errors as function of the contrast are shown for the aMRCM, MMMFEM and MHM considering both the linear and physics-based spaces. Three domain decompositions are considered: with 4×4, 8×8 and 16×16 coarse cells. We note that the aMRCM-PBS is more accurate than the aMRCM-POL in all the contrast and meshes considered.

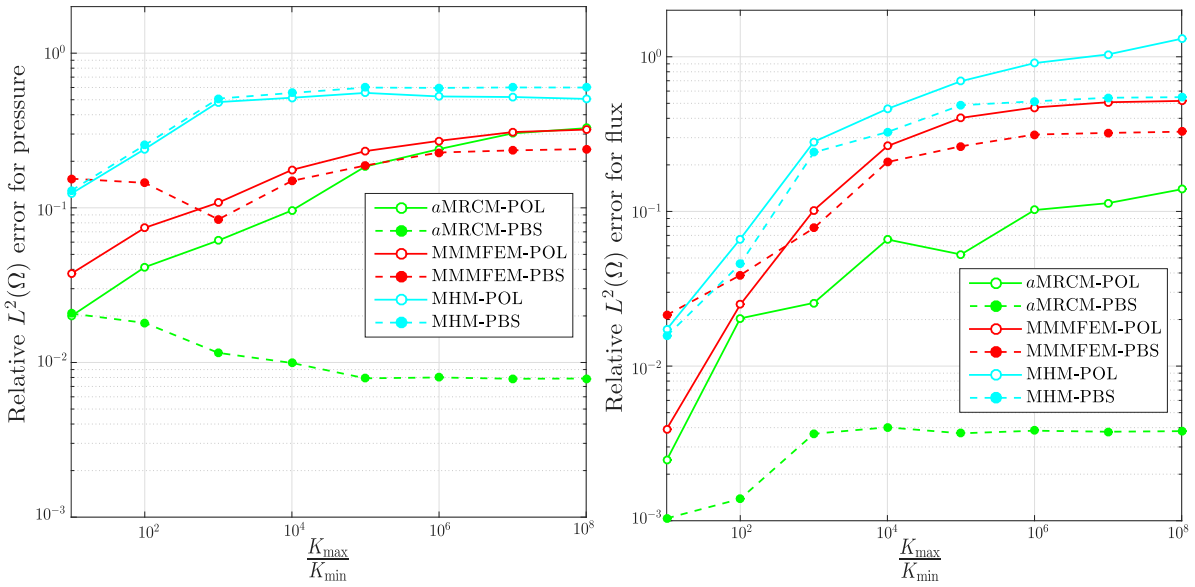

Source: Research data.

the previous works (GUIRALDELLO *et al.*, 2018; GUIRALDELLO *et al.*, 2019; ROCHA *et al.*, 2020b). But the approximations by choosing any constant value of α, even for the MRCM-PBS are inaccurate. We remark that the MMMFEM and MHM are also included in this observation. One can conclude that, besides the physics-based interface spaces, the aMRCM is necessary to obtain more accurate solutions. We note that the choice of $\alpha_{\text{small}} = 10^{-2}$ and $\alpha_{\text{large}} = 10^{2}$ or $\alpha_{\text{small}} = 10^{-6}$ and $\alpha_{\text{large}} = 10^{6}$ does not affect significantly the error.

These results indicate that the linear interface spaces are not robust for capturing the effects of features as high permeability channels and barriers. Even the physics-based spaces are not enough for complex fields if not combined with an appropriate multiscale method. In order to study how these results are reflected in the corresponding saturation fields, in the next subsection we present numerical results for two-phase flows.

4.3.2 Two-phase flow and transport problems

Now we focus on a study of the MRCM performance for two-phase flows using the physics-based interface spaces for high-contrast channelized permeability fields. We introduce the saturation comparisons with a detailed analysis of fingering instabilities to show the impact of the design of the basis functions on the transport of the water saturation. Firstly we present numerical results for the permeability field with high permeability channels and barriers of the previous subsection. Then we consider a high-contrast permeability field with channels and

Figure 34 – Pressure approximations considering the contrast of $K_{\max}/K_{\min} = 10^8$. First line, left to right: permeability field, fine mesh, aMRCM-POL, and aMRCM-PBS solutions. Second line, left to right: MMMFEM-POL, MMMFEM-PBS, MHM-POL, and MHM-PBS solutions. The domain decomposition considered contains 8×8 coarse cells and is illustrated by the lines in the plot. We note that the aMRCM-PBS approximation is the most closely related to the reference solution followed by the aMRCM-POL.

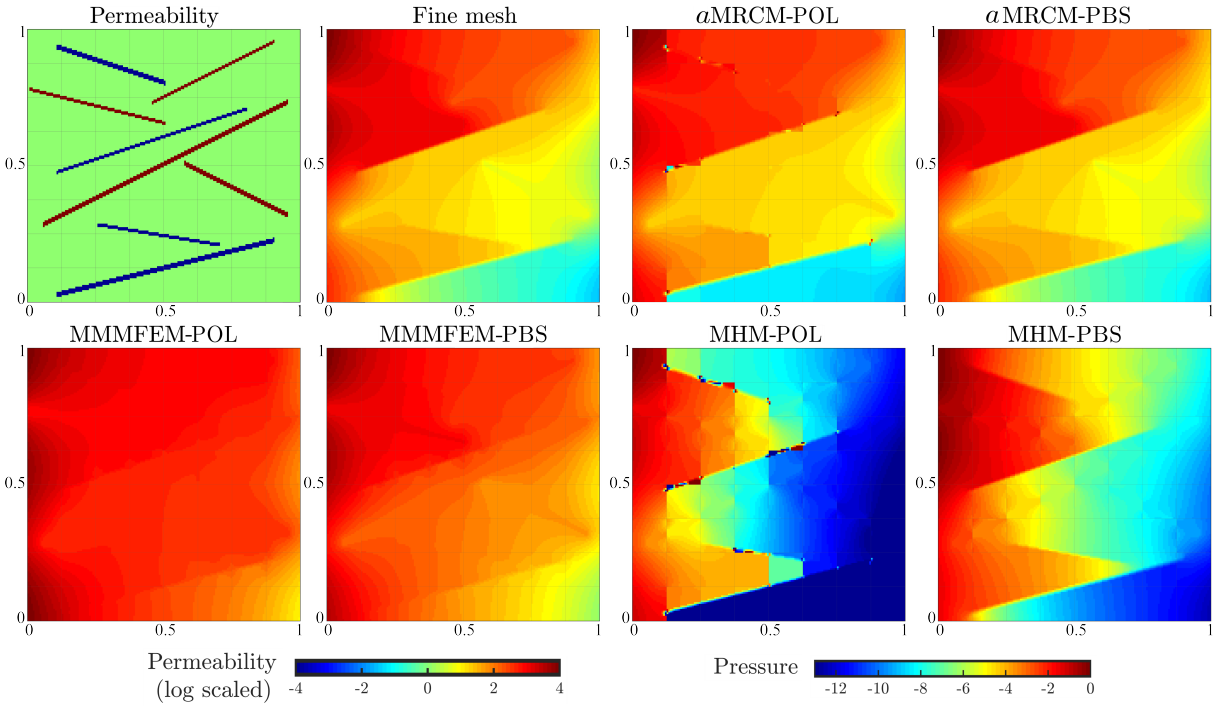

Source: Research data.

isolated inclusions that has frequently appeared in the literature (JIANG; LI, 2017).

In all simulations the reservoir is initially filled with oil ($s^0 = 0$) and water is injected at a constant rate. We consider $M = \mu_o/\mu_w$ set as $M = 10$, and the relative permeabilities given by $k_{ro} = (1-s)^2$ and $k_{rw} = s^2$. The hyperbolic equation (2.2) is approximated by an explicit Euler time integration combined with the first order upwind method. In the operator splitting approach, we take the number of transport steps between the elliptic updates at most $C = 20$. We use the extrapolation of Eq. (2.4) in our numerical experiments. The time units employed are in PVI.

4.3.2.1 *High-contrast permeability field with high permeability channels and barriers*

The objective of this study is to investigate the aMRCM, MMMFEM and MHM saturation solutions considering the physics-based interface spaces for the high-contrast permeability field with high permeability channels and barriers. We consider the permeability field of the previous experiment, illustrated in Figure 31. We fix the highest permeability contrast $K_{\max}/K_{\min} = 10^8$ and the domain decomposition having 8×8 subdomains, each one discretized by 20×20 cells.

The first example considers the same slab geometry of the previous experiments, by

Figure 35 – Flux approximations considering the contrast of $K_{\max}/K_{\min} = 10^8$. First line, left to right: permeability field, fine mesh, *a*MRCM-POL, and *a*MRCM-PBS solutions. Second line, left to right: MMMFEM-POL, MMMFEM-PBS, MHM-POL, and MHM-PBS solutions. The colors refer to the log-scale flux magnitude. The domain decomposition considered contains 8×8 coarse cells and is illustrated by the lines in the plot. The only accurate procedure is the *a*MRCM-PBS.

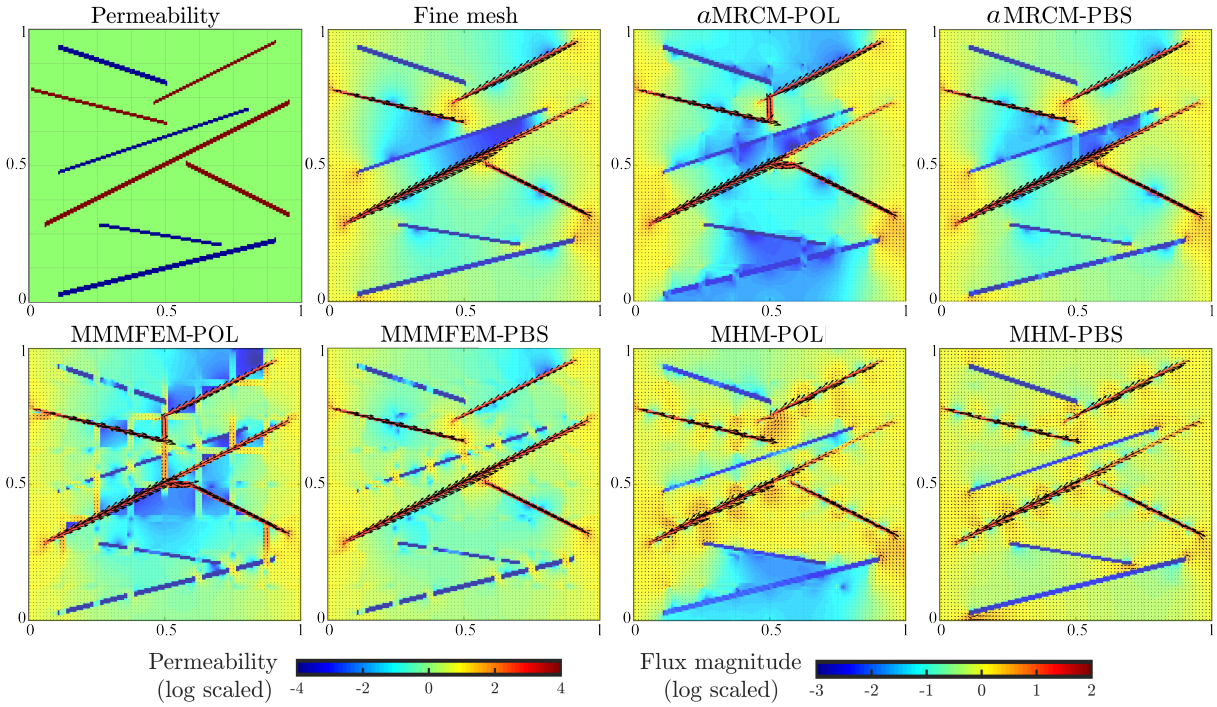

Source: Research data.

imposing the flux on the left and right boundaries and no source terms. Figure 37 shows the permeability field (log-scaled) along with the saturation profiles at $T_{\text{PVI}} = 0.06$ (before breakthrough time) approximated by the multiscale methods with the linear and the physics-based interface spaces. The procedure that produces a saturation solution closer to the reference one is the *a*MRCM-PBS. The use of the physics-based spaces enables more accurate solutions for the *a*MRCM and the MMMFEM. However, the last one is still inaccurate. The MHM solutions are unacceptable either for linear or physics-based spaces. The corresponding relative $L^1(\Omega)$ errors throughout the simulation are presented in Figure 38. We note an expressive improvement provided by the physics-based interface spaces combined with the *a*MRCM. This combination enables the error to drop by one order of magnitude.

Now we maintain the slab geometry but using global boundary conditions of no-flow at top and bottom boundaries along with imposed pressure on the left and right boundaries. In Figure 39 we present the saturation profiles at $T_{\text{PVI}} = 0.0001$ (before breakthrough time) approximated by the multiscale methods with the linear and the physics-based interface spaces. Similar results to the previous example are obtained. The corresponding relative errors throughout the simulation are presented in Figure 40, where it is clear the improved accuracy provided

Figure 36 – Relative $L^2(\Omega)$ errors as a function of α for pressure (left) and flux (right) considering the permeability field plotted in Figure 31 with contrast of 10^8 and the domain decomposition that contains 8×8 coarse cells. The physics-based and linear spaces are compared. We include the errors for two choices in the aMRCM: setting $\alpha_{\text{small}} = 10^{-2}$ and $\alpha_{\text{large}} = 10^{2}$ or $\alpha_{\text{small}} = 10^{-6}$ and $\alpha_{\text{large}} = 10^{6}$ (illustrated as horizontal lines). The improvement with the combination of the aMRCM and the physics-based spaces is expressive.

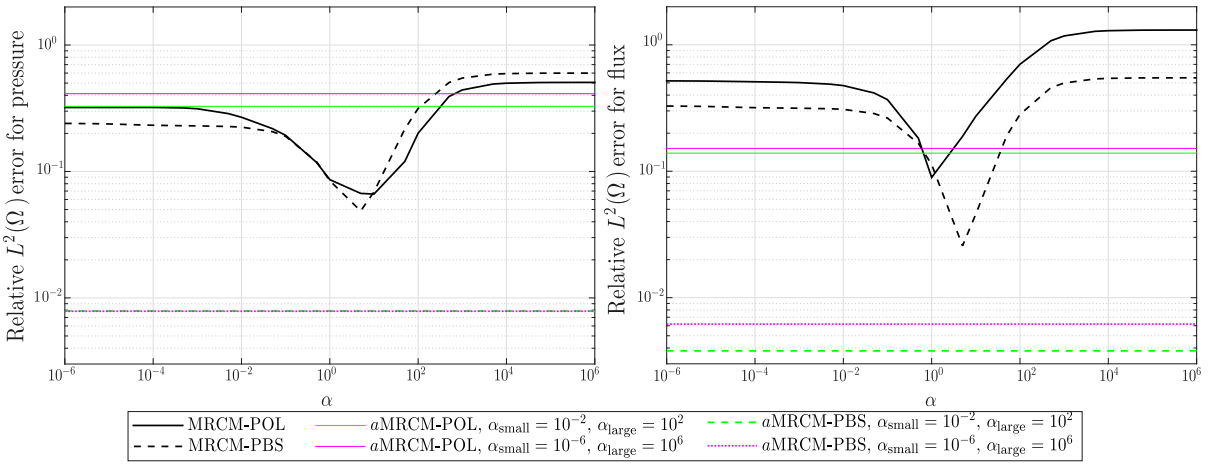

Source: Research data.

by combining the physics-based spaces with the aMRCM. Again, the MHM solutions are not acceptable with both interface spaces. The MMMFEM approximations improve significantly with the physics-based spaces, however, these solutions are comparable to the aMRCM-POL approximations.

Lastly, we test the multiscale methods in a quarter of a five-spot model, where we inject the water at the bottom-left cell and the sink is located at the top-right cell. The saturation profiles at $T_{\text{PVI}} = 0.09$ (before breakthrough time) are shown in Figure 41. The most accurate solutions are produced by the aMRCM considering both types of interface spaces. The MMMFEM and MHM approximations present expressive fingering instabilities that are not present in the fine grid solution. In Figure 42, the relative errors confirm that the aMRCM produces more accurate solutions. It is noticeable the poor quality solutions provided by the MMMFEM and MHM (even with the physics-based spaces), that are less accurate than the aMRCM-POL approximation. The solutions produced by the aMRCM-PBS are much more accurate than all the other approximations.

The high-contrast permeability fields are challenging for multiscale methods. We show that the methods fail in a field with both high permeability channels and barriers. In all the models previously tested, the aMRCM-PBS is the only scheme that provides satisfactory approximations.

4.3.2.2 High-contrast permeability field with channels and isolated inclusions

In this subsection, we consider a high-contrast permeability field with channels and isolated inclusions that has frequently appeared in the literature (EFENDIEV; GALVIS; HOU,

Figure 37 – Comparison of multiscale methods for the slab geometry with flux boundary conditions on the left and right. Saturation profiles at $T_{PVI} = 0.06$ for the permeability field with high permeability channels and barriers are shown. First line, left to right: high-contrast permeability field (log-scaled); reference fine grid solution; *a*MRCM-POL saturation profile; *a*MRCM-PBS saturation profile. Second line, left to right: MMMFEM-POL saturation profile; MMMFEM-PBS saturation profile; MHM-POL saturation profile; MHM-PBS saturation profile. The *a*MRCM-PBS provides the most accurate approximation.

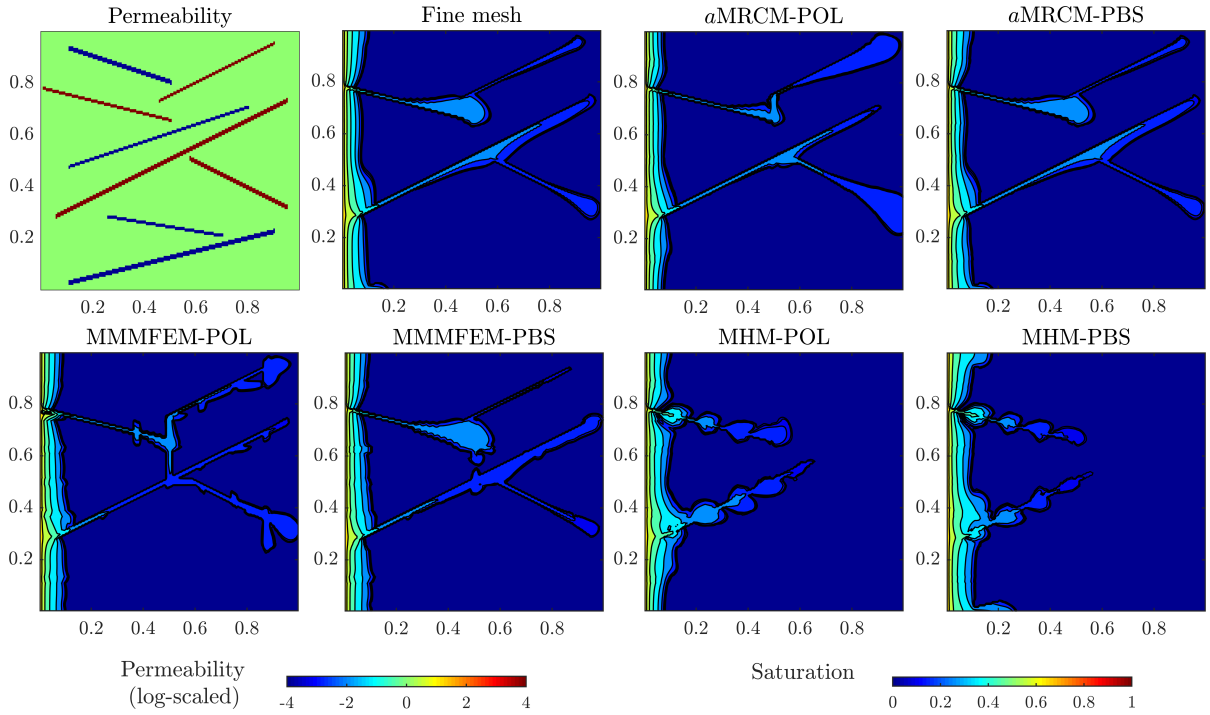

Source: Research data.

2013; CHUNG; EFENDIEV; LEE, 2015; CHUNG; FU; YANG, 2016; CHUNG; EFENDIEV; LI, 2014; CHUNG; EFENDIEV; LEUNG, 2017; CHUNG; PUN, 2019; JIANG; LI, 2017). We consider a domain Ω containing 100×100 fine grid cells divided into 5×5 subdomains. The boundary conditions are no-flow at the top and bottom boundaries along with an imposed flux on the left and right boundaries. No source terms are considered. The permeability contrast considered is $K_{\text{max}}/K_{\text{min}} = 10^6$ and the cutoff values are set as $\zeta_{\text{max}} = \zeta_{\text{min}} = 1$.

Figure 43 shows the permeability field (log-scaled) containing high-permeable channels and isolated inclusions and the saturation profiles at $T_{\text{PVI}} = 0.07$ (before breakthrough). In this example, only the pressure physics-based spaces are used to handle the high-permeable structures, since there are no barriers. The more accurate solutions are provided by the *a*MRCM-PBS and the MMMFEM-PBS. For these two methods, the figure shows that the imprecisions that happen by using the linear spaces have completely disappeared with the physics-based spaces. The MHM solutions are inaccurate. We remark that the MHM method provides the same solution with the linear and the physics-based interface spaces, because this method considers only the flux space, which is always maintained as linear for this permeability field. The relative errors are shown in Figure 44 and reflect these observations throughout the whole simulation.

Figure 38 – Relative $L^1(\Omega)$ saturation errors as a function of time for the slab geometry with flux boundary conditions considering the field with high permeability channels and barriers. We compare the aMRCM, MMMFEM and MHM with both physics-based and linear spaces. We note that the errors associated with the aMRCM-PBS are much smaller than all the others.

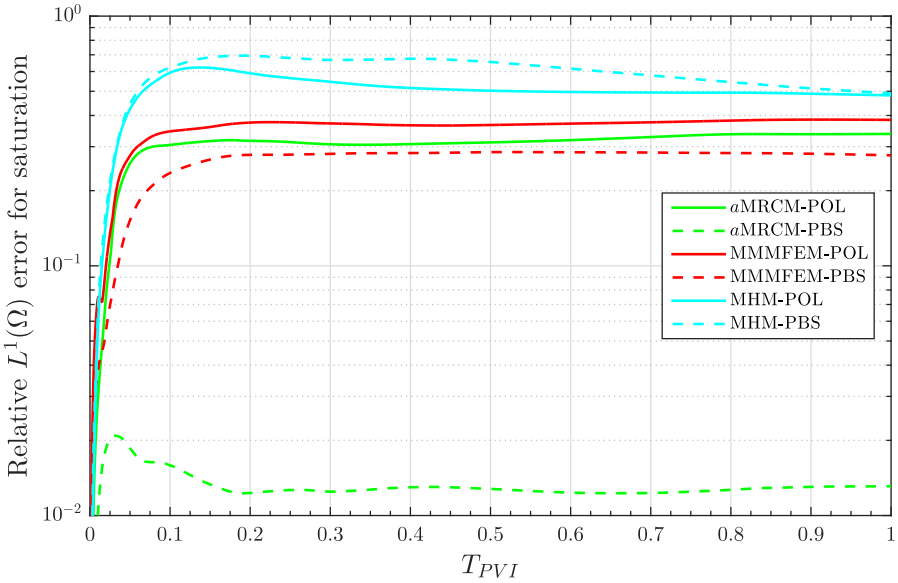

Source: Research data.

As a final validation, we consider the performance of the methods in dealing with the same high-contrast permeability field replacing the type of channelized structures to barriers, as in (JIANG; LI, 2017). Figure 45 shows the permeability field (log-scaled) containing the low-permeable channels and the saturation profiles at $T_{\text{PVI}} = 0.33$ (before breakthrough). In this case, only the flux physics-based spaces are used, since there are only low-permeable structures. We note a considerable improvement in the aMRCM and MHM approximations replacing the linear interface spaces by the physics-based ones. The MMMFEM solutions present just some modest errors if compared to the aMRCM-POL and MHM-POL approximations. We remark that the MMMFEM solutions are the same with the linear and the physics-based interface spaces because, this method considers only the pressure space, which is always maintained as linear for this permeability field. The relative errors throughout the whole simulation are shown in Figure 46. We confirm that the aMRCM-POL and MHM-POL are not accurate, the MMMFEM provides intermediate results and the aMRCM-PBS and MHM-PBS produce the most accurate approximations.

The numerical studies demonstrate the improvement obtained by using physics-based interface spaces. High-contrast fields were chosen that allowed us to assess the ability of the methods to handle problems in the presence of both high and low-permeable structures. The results provide strong evidence that the adaptive MRCM combined with the physics-based spaces leads to improved transport approximations in high-contrast channelized porous media.

Figure 39 – Comparison of multiscale methods for the slab geometry with pressure boundary conditions on the left and right. Saturation profiles at $T_{PVI} = 0.0001$ for the permeability field with high permeability channels and barriers are shown. First line, left to right: high-contrast permeability field (log-scaled); reference fine grid solution; *a*MRCM-POL saturation profile; *a*MRCM-PBS saturation profile. Second line, left to right: MMMFEM-POL saturation profile; MMMFEM-PBS saturation profile; MHM-POL saturation profile; MHM-PBS saturation profile. The *a*MRCM-PBS is clearly the most accurate procedure.

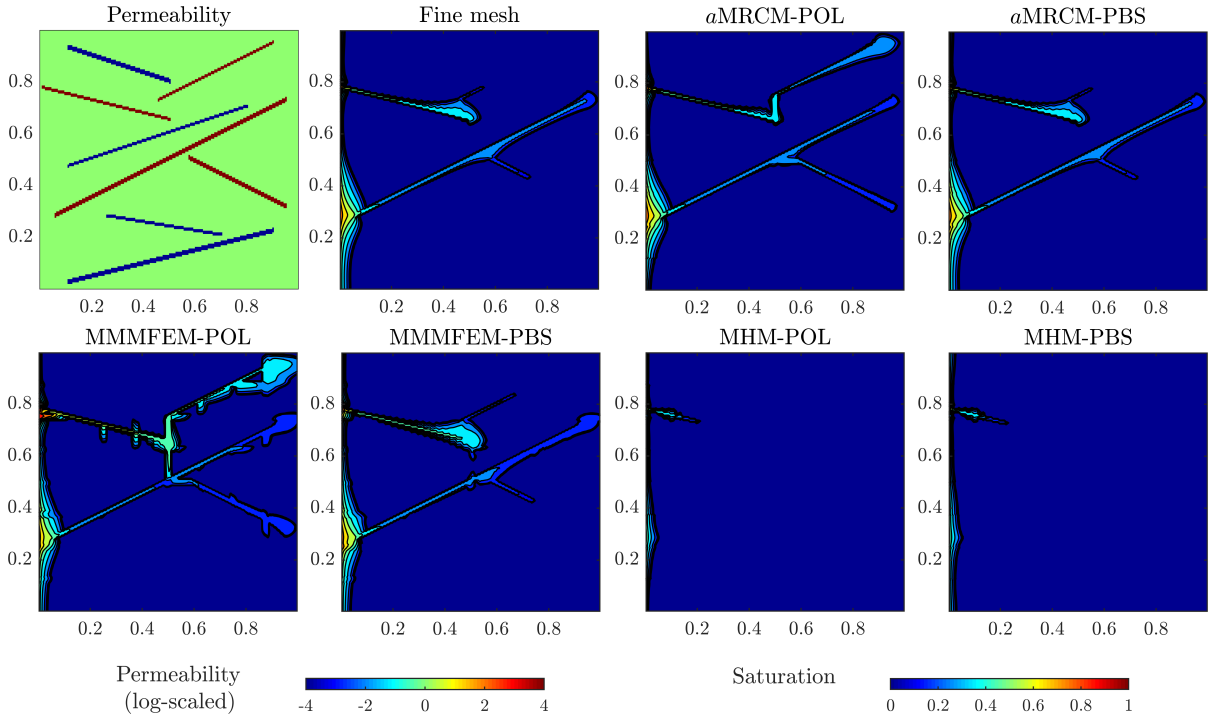

Source: Research data.

4.4 Discussion

Two physics-based interface spaces (one for pressure and other for flux) have been proposed for better capturing the high-contrast effects of channelized structures. A careful investigation has been performed for the numerical solution of single and two-phase flows by combining the new spaces with multiscale mixed methods.

We show that the introduced physics-based pressure space can offer much better accuracy in comparison with the usual polynomial spaces in the presence of high-permeable structures. On the other hand, the proposed physics-based flux space can provide more accurate solutions in comparison with the polynomial spaces in the presence of low-permeable structures. Two well known multiscale procedures have been applied to confirm these results: the Multiscale Mortar Mixed Finite Element Method (combined with the pressure space) and the Multiscale Hybrid-Mixed Finite Element Method (using the flux space). Aiming at using simultaneously both interface spaces we combine them with the MRCM, which allows for including the interface spaces independently. With this combination, we achieve the best accuracy in the approximation of challenging high-contrast flows in comparison with the other multiscale methods tested.

Figure 40 – Relative $L^1(\Omega)$ saturation errors as a function of time for the slab geometry with pressure boundary conditions considering the field with high permeability channels and barriers. We compare the *a*MRCM, MMMFEM and MHM with both physics-based and linear spaces. Similarly to the previous example, the errors associated with the *a*MRCM-PBS are the smallest.

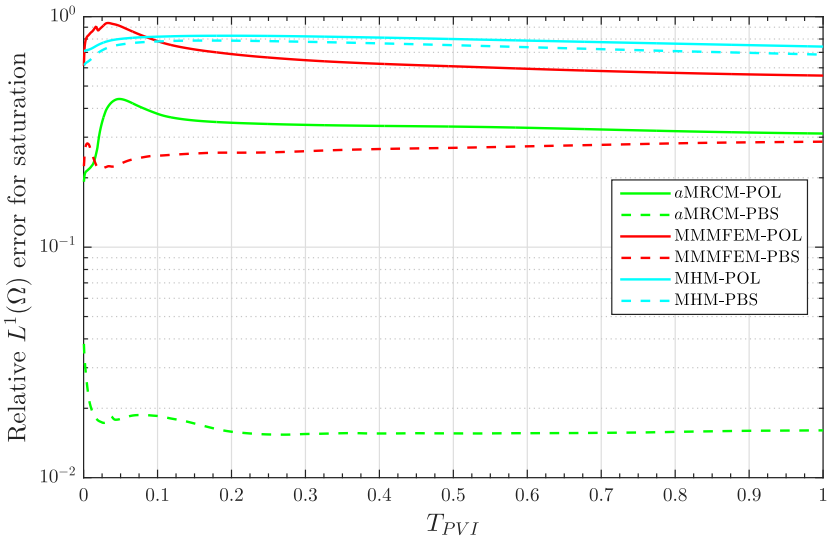

Source: Research data.

Figure 41 – Comparison of multiscale methods for the quarter of a five-spot geometry. Saturation profiles at $T_{PVI} = 0.09$ for the permeability field with high permeability channels and barriers are shown. First line, left to right: high-contrast permeability field (log-scaled); reference fine grid solution; *a*MRCM-POL saturation profile; *a*MRCM-PBS saturation profile. Second line, left to right: MMMFEM-POL saturation profile; MMMFEM-PBS saturation profile; MHM-POL saturation profile; MHM-PBS saturation profile. The *a*MRCM is the only procedure that captures the details of the fingers.

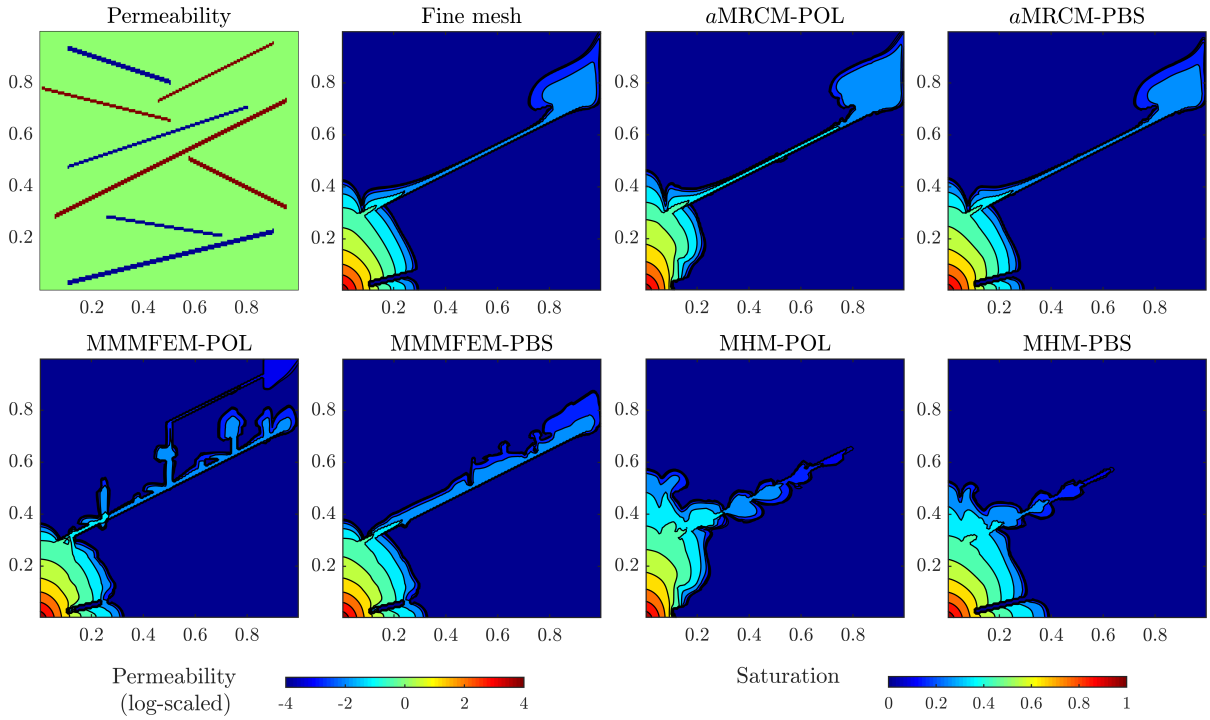

Source: Research data.

Figure 42 – Relative $L^1(\Omega)$ saturation errors as a function of time for the quarter of a five-spot geometry on the field with high permeability channels and barriers. We compare the *a*MRCM, MMMFEM and MHM with both physics-based and linear spaces. The errors associated with the *a*MRCM-PBS are the smallest, followed by the *a*MRCM-POL.

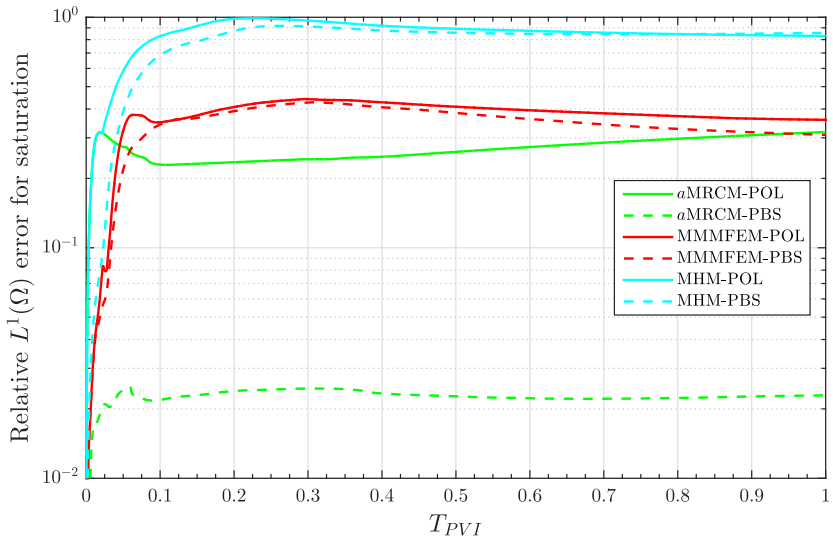

Source: Research data.

Figure 43 – Comparison of multiscale methods. Saturation profiles at $T_{PVI} = 0.07$ for the permeability field with channels and isolated inclusions. First line, left to right: high-contrast permeability field (log-scaled); reference fine grid solution; *a*MRCM-POL saturation profile; *a*MRCM-PBS saturation profile. Second line, left to right: MMMFEM-POL saturation profile; MMMFEM-PBS saturation profile; MHM-POL saturation profile; MHM-PBS saturation profile. The more accurate approximations are attained by the *a*MRCM-PBS and MMMFEM-PBS.

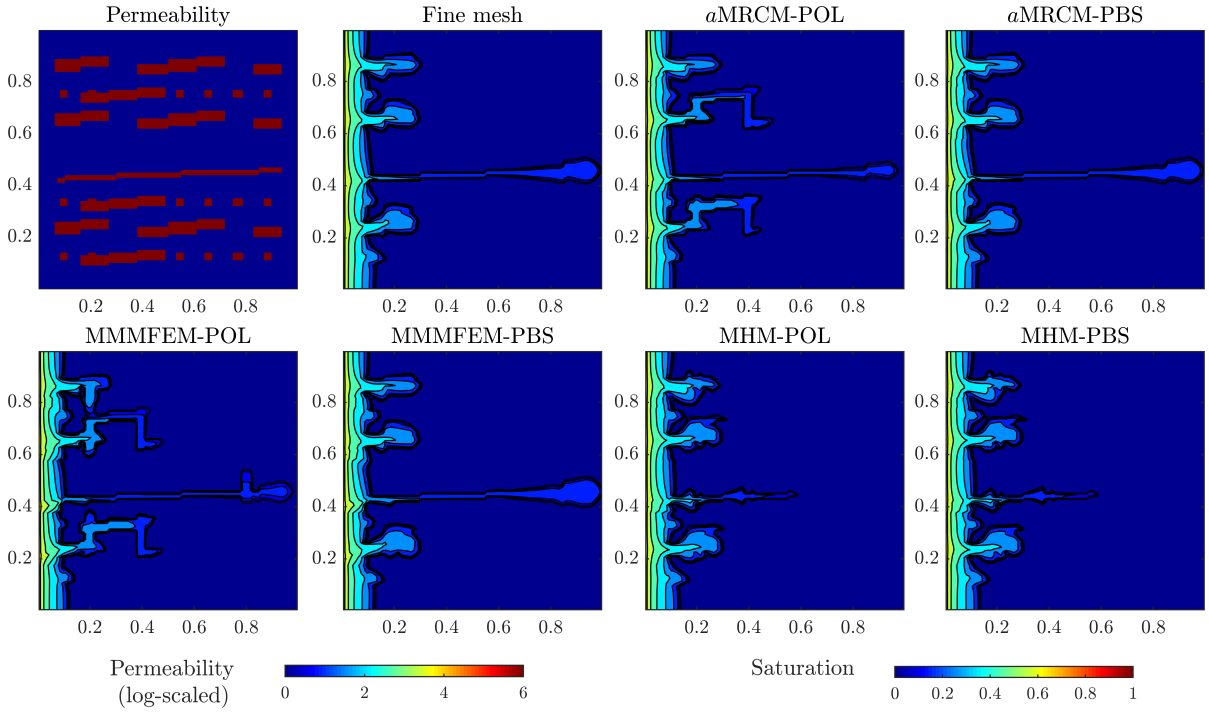

Source: Research data.

Figure 44 – Relative $L^1(\Omega)$ saturation errors as a function of time on the field with channels and isolated inclusions. We compare the *a*MRCM, MMMFEM and MHM with both physics-based and linear spaces. The errors associated with the *a*MRCM-PBS and MMMFEM-PBS are the smallest.

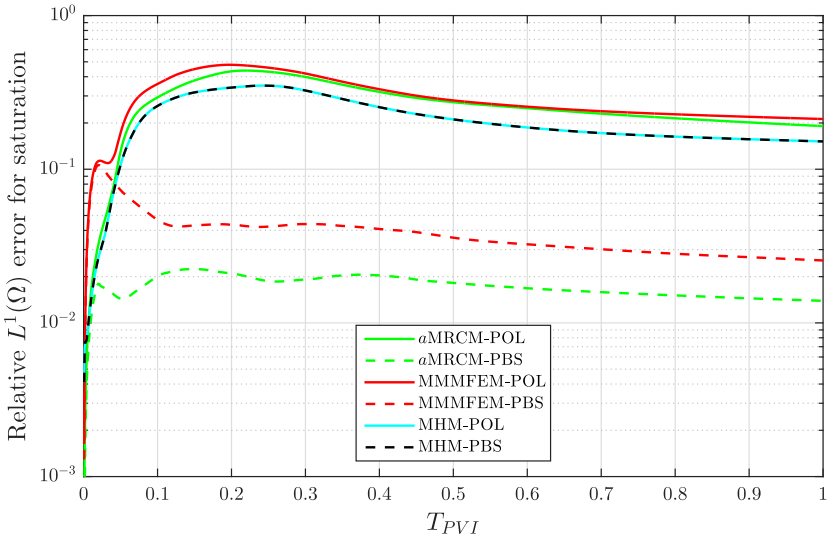

Source: Research data.

Figure 45 – Comparison of multiscale methods. Saturation profiles at $T_{PVI} = 0.33$ for the permeability field with barriers are shown. First line, left to right: high-contrast permeability field (log-scaled); reference fine grid solution; *a*MRCM-POL saturation profile; *a*MRCM-PBS saturation profile. Second line, left to right: MMMFEM-POL saturation profile; MMMFEM-PBS saturation profile; MHM-POL saturation profile; MHM-PBS saturation profile. A considerable improvement is noticed in the *a*MRCM and MHM approximations replacing the linear spaces by the physics-based.

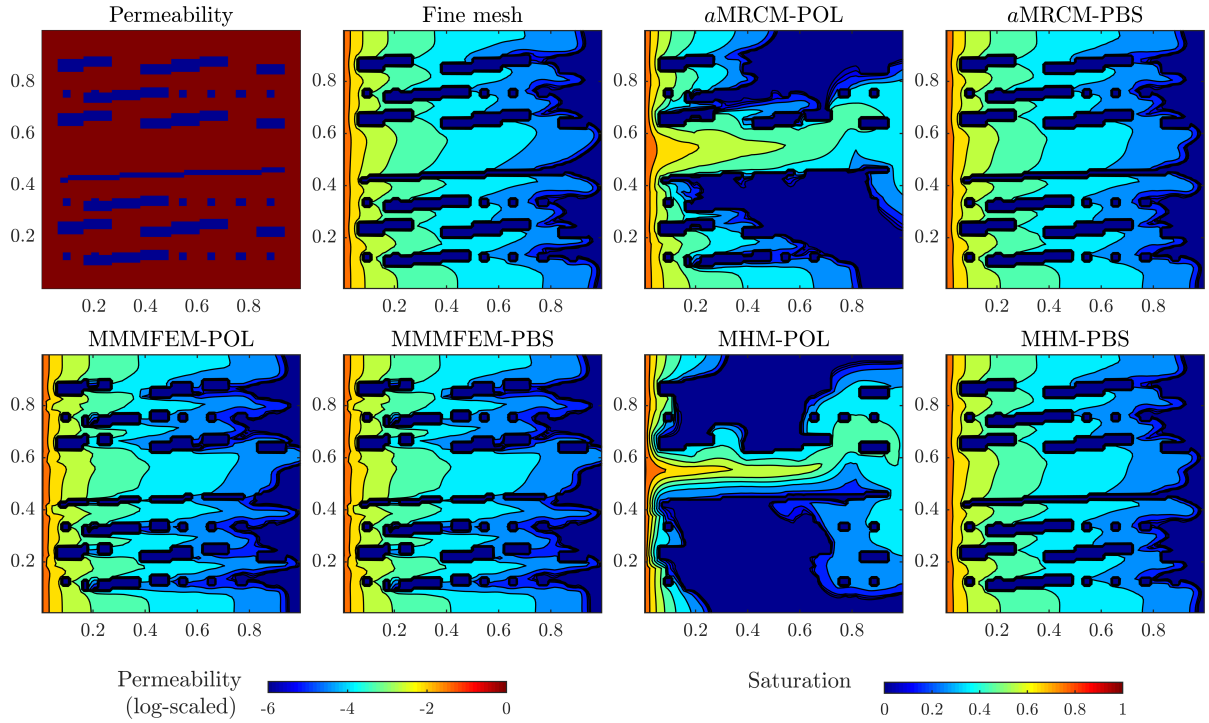

Source: Research data.

Figure 46 – Relative $L^1(\Omega)$ saturation errors as a function of time on the field with barriers. We compare the *a*MRCM, MMMFEM and MHM with both physics-based and linear spaces. The *a*MRCM-PBS and MMMFEM-PBS produce the smallest errors.

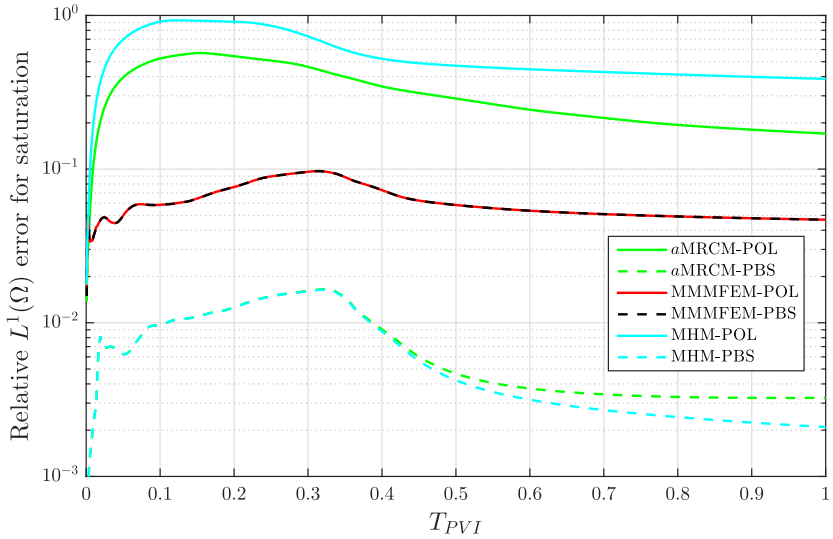

Source: Research data.

CHAPTER

5

THE MUTISCALE PERTURBATION METHOD

In this chapter, we formulate and test a new procedure, the Multiscale Perturbation Method for Two-Phase Flows (MPM-2P), to speed-up the solution of two-phase flows in porous media approximated by an operator splitting method. The proposed procedure is based on domain decomposition and combines the MRCM with the Multiscale Perturbation Method (MPM) (ALSADIG *et al.*, 2020).

A recursive formulation of the MRCM recently introduced (FERRAZ, 2019) shows excellent scalability (both weak and strong) for the solution of second order elliptic equations. These conclusions were reached by solving elliptic equations on state-of-the-art multi-core devices, for problems with a few billion variables that are of interest to the oil industry. In (FERRAZ, 2019) the solution of a second-order elliptic equation is obtained in two steps. In a first step, for each subdomain of a decomposition of the domain of interest, a set of multiscale basis functions (local boundary value problems of Robin type) has to be computed. Then, a coarse interface problem defined on the skeleton of the domain decomposition needs to be solved. It has been shown in (FERRAZ, 2019) that the time associated with the solution of the interface problem is essentially negligible when compared to the time spent in solving the local boundary value problems that give the multiscale basis functions. Thus, a fair assessment of the cost of the solution of the elliptic equation by a multiscale method can be made in terms of the number of multiscale basis functions that are computed. Our main objective in this chapter is to design a method that can accomplish a reduction in the number of updates of multiscale basis functions that are needed in the numerical simulation of two-phase flows.

In order to explain our approach, consider the operator splitting scheme for two-phase flows as presented in Chapter 2. If the MRCM is applied to solve the elliptic equation, then a set of multiscale basis functions has to be, in principle, recomputed every time the solution algorithm calls for an updated velocity field. Thus, the development of methods that reduce the number

of multiscale basis functions to be computed in each subdomain, without loss of accuracy, is of great importance to speed-up the solution of two-phase flow problems. The procedure that we introduce in this chapter has precisely this objective. The MPM-2P is based on the original MPM (ALSADIG *et al.*, 2020), that was introduced to approximate the velocity field by reusing multiscale basis functions computed for a distinct pressure equation (with different, but closely related coefficients), provided that the solutions of the two elliptic equations at hand can be related by classical perturbation theory. The method proposed here combines the MPM with the MRCM for two-phase flow problems. When an update of the velocity field is called by the operator splitting algorithm, the MPM-2P may provide an accurate and computationally inexpensive approximation for the velocity field by reusing multiscale basis functions that are computed by the MRCM at an earlier time of the simulation. Thus, a full update of all multiscale basis functions required by the MRCM for the construction of a new velocity field is avoided.

The formulation and a cost analysis of the MRCM-2P are presented in section 5.1, followed by section 5.2 with the numerical experiments. Concluding remarks of the chapter appear in section 5.3.

5.1 The Multiscale Perturbation Method for Two-Phase Flows

We consider the operator splitting scheme for two-phase flows as presented in Chapter 2, where pressure is updated at times $t_n = n\Delta t_p$, for $n = 0, 1, \ldots$, while the saturation is computed at intermediate times $t_{n,k} = t_n + k\Delta t_s$, for $k = 1, 2, \ldots, C_n$, such that $t_n < t_{n,k} \leq t_{n+1}$. Here, we denote by C_n the number of transport time steps between t_n and t_{n+1}.

Let $p^n(\mathbf{x})$, $\mathbf{u}^n(\mathbf{x})$ and $s^n(\mathbf{x})$ denote the pressure, velocity and saturation approximations at time t^n. We compute the saturation $s^n(\mathbf{x})$ through Eq. (2.2) by using an explicit Euler time integration (with $\mathbf{u}^{n-1}$ constant at intermediate times $t_{n-1,k}$) combined with a first order upwind method. Then, the saturation $s^n(\mathbf{x})$ is used to compute the pressure $p^n(\mathbf{x})$ and velocity $\mathbf{u}^n(\mathbf{x})$ through Eq. (2.1) by applying a multiscale method. At this point, instead of calling directly the MRCM, our operator splitting algorithm uses it in the framework of the MPM.

5.1.1 Reusing basis functions previously computed

The goal of the MPM-2P is to approximate the pressure $p^n(\mathbf{x})$ and velocity $\mathbf{u}^n(\mathbf{x})$ by reusing the Basis Functions (BFs) that are computed by the MRCM at an earlier time of the simulation. In order to introduce the formulation of the MPM-2P, consider that the BFs computed at time t_m ($m < n$) will be reused. Therefore, we have two elliptic problems: $\mathscr{P}_{t_m}$ and $\mathscr{P}_{t_n}$, associated with times t_m and t_n, respectively. Following the perturbation theory presented in (ALSADIG *et al.*, 2020), we express the conductivity of problem $\mathscr{P}_{t_n}$ as a perturbation of

the conductivity of problem $\mathscr{P}_{t_m}$, i.e. $\kappa^n = \kappa^n(\mathbf{x}) = \lambda(s^n(\mathbf{x}))K(\mathbf{x}) = \kappa^m + \varepsilon\kappa_\varepsilon$, where $\varepsilon = ||\kappa^n - \kappa^m||_{L^2(\Omega)}$ is a small parameter that measures the difference between κ^n and κ^m from times t_n and t_m, respectively, while $\kappa_\varepsilon = (\kappa^n - \kappa^m)/\varepsilon$ is an auxiliary field related to the formulation of the MPM. Thus, the two elliptic problems at hand can be written as

$$\mathscr{P}_{t_m}: \begin{cases} \mathbf{u}^m &= -\kappa^m \nabla p^m & \text{in } \Omega \\ \nabla\cdot\mathbf{u}^m &= q & \text{in } \Omega \\ p^m &= g & \text{on } \partial\Omega^p \\ \mathbf{u}^m\cdot\mathbf{n} &= z & \text{on } \partial\Omega_u \end{cases} \tag{5.1}$$

and

$$\mathscr{P}_{t_n}: \begin{cases} \mathbf{u}^n &= -(\kappa^m + \varepsilon\kappa_\varepsilon)\nabla p^n & \text{in } \Omega \\ \nabla\cdot\mathbf{u}^n &= q & \text{in } \Omega \\ p^n &= g & \text{on } \partial\Omega_p \\ \mathbf{u}^n\cdot\mathbf{n} &= z & \text{on } \partial\Omega_u. \end{cases} \tag{5.2}$$

For simplicity, we assume that the source term and the known boundary functions depend only on space, but time-dependent source terms and boundary data can, in principle, be considered. Next, we write the pressure and flux of problem $\mathscr{P}_{t_n}$ as perturbations of the respective pressure and flux of problem $\mathscr{P}_{t_m}$:

$$p^n = p^m + \delta p^n, \tag{5.3}$$

$$\mathbf{u}^n = \mathbf{u}^m + \delta\mathbf{u}^n. \tag{5.4}$$

By combining this decomposition with problem $\mathscr{P}_{t_n}$ (5.2) we get the following auxiliary system for the pair $(\delta\mathbf{u}^n, \delta p^n)$

$$\mathscr{P}_{\hat{\mathbf{u}}}: \begin{cases} \hat{\mathbf{u}} &= -(\kappa^m + \varepsilon\kappa_\varepsilon)\nabla\delta p^n & \text{in } \Omega \\ \nabla\cdot\hat{\mathbf{u}} &= q + \nabla\cdot((\kappa^m + \varepsilon\kappa_\varepsilon)\nabla p^m) & \text{in } \Omega \\ \delta p^n &= g - p^m & \text{on } \partial\Omega_p \\ \hat{\mathbf{u}}\cdot\mathbf{n} &= z + ((\kappa^m + \varepsilon\kappa_\varepsilon)\nabla p^m)\cdot\mathbf{n} & \text{on } \partial\Omega_u, \end{cases} \tag{5.5}$$

where $\hat{\mathbf{u}} = \mathbf{u}^m + \delta\mathbf{u}^n + (\kappa^m + \varepsilon\kappa_\varepsilon)\nabla p^m$. Although this system is well-posed, its solution is as expensive as the direct solution of problem $\mathscr{P}_{t_n}$, so approximations are needed in order to reduce the cost of solving this auxiliary problem.

Since our goal is to reuse the BFs computed for problem $\mathscr{P}_{t_m}$ (5.1), we need to somehow connect the solution of $\mathscr{P}_{\hat{\mathbf{u}}}$ (5.5) to the solution space of $\mathscr{P}_{t_m}$. This would allow us to write the solution of $\mathscr{P}_{\hat{\mathbf{u}}}$ by taking advantage of the span of the precomputed BFs. To approximate δp^n and $\delta\mathbf{u}^n$, we consider the following perturbation expansions:

$$\delta p^n = \delta p_0^n + \varepsilon\delta p_1^n + \varepsilon^2\delta p_2^n + \varepsilon^3\delta p_3^n + \cdots \tag{5.6}$$

and

$$\delta\mathbf{u}^n = \delta\mathbf{u}_0^n + \varepsilon\delta\mathbf{u}_1^n + \varepsilon^2\delta\mathbf{u}_2^n + \varepsilon^3\delta\mathbf{u}_3^n + \cdots \tag{5.7}$$

By applying Eqs. (5.6) and (5.7) in Eq. (5.5), and considering the expansions up to term ε^ℓ, we get the following problems for $\ell = 0$ and $\ell > 0$, respectively:

$$\mathscr{P}_{\hat{\mathbf{u}}_0}: \begin{cases} \hat{\mathbf{u}}_0 &= -\kappa^m \nabla \delta p_0^n & \text{in } \Omega \\ \nabla \cdot \hat{\mathbf{u}}_0 &= q + \nabla \cdot ((\kappa^m + \varepsilon \kappa_\varepsilon) \nabla p^m) & \text{in } \Omega \\ \delta p_0^n &= g - p^m & \text{on } \partial\Omega_p \\ \hat{\mathbf{u}}_0 \cdot \mathbf{n} &= z + ((\kappa^m + \varepsilon \kappa_\varepsilon) \nabla p^m) \cdot \mathbf{n} & \text{on } \partial\Omega_u, \end{cases} \tag{5.8}$$

$$\mathscr{P}_{\hat{\mathbf{u}}_\ell}: \begin{cases} \hat{\mathbf{u}}_\ell &= -\kappa^m \nabla \delta p_\ell^n & \text{in } \Omega \\ \nabla \cdot \hat{\mathbf{u}}_\ell &= \nabla \cdot (\kappa_\varepsilon \nabla p_{\ell-1}^n) & \text{in } \Omega \\ \delta p_\ell^n &= 0 & \text{on } \partial\Omega_p \\ \hat{\mathbf{u}}_\ell \cdot \mathbf{n} &= 0 & \text{on } \partial\Omega_u, \end{cases} \tag{5.9}$$

where $\hat{\mathbf{u}}_0 = \mathbf{u}^m + \delta \mathbf{u}_0^n + (\kappa^m + \varepsilon \kappa_\varepsilon) \nabla p^m$ and $\hat{\mathbf{u}}_\ell = \delta \mathbf{u}_\ell^n + \kappa_\varepsilon \nabla \delta p_{\ell-1}^n$. The problem $\mathscr{P}_{\hat{\mathbf{u}}_0}$ is associated with ε^0, while the problems $\mathscr{P}_{\hat{\mathbf{u}}_\ell}$ are associated with ε^ℓ, for each $\ell > 0$.

The approach developed in (ALSADIG *et al.*, 2020), neglects the perturbation terms with $\ell > 1$, since they are small enough ($\varepsilon^2 \ll 1$ if the perturbation in the conductivity is small enough from time t_m to time t_n). We find from our numerical experiments for two-phase flows that, even the first-order perturbation term can be neglected. We obtain accurate results when compared to the solution given directly by the MRCM. Therefore, our numerical experiments consider the approximation of $(\delta \mathbf{u}^n, \delta p^n)$ given by the solution of problem $\mathscr{P}_{\hat{\mathbf{u}}_0}$ (5.8), that is associated with ε^0.

We solve Eq. (5.8) to approximate $(\hat{\mathbf{u}}_0, \delta p_0^n)$ by using the MRCM. Note that the conductivity in this equation is κ^m, thus we can take advantage of the BFs computed at time t_m to solve only one local boundary value problem with trivial Robin boundary conditions for each subdomain. Specifically, considering the MRCM additive decomposition of the local approximations, we only need to solve the non-homogeneous part of the solution given by Eq. (2.13). Then, the global unknowns are given by a linear combination of the precomputed BFs, whose coefficients are obtained by solving an inexpensive interface problem.

With the computed approximation for $(\hat{\mathbf{u}}_0, \delta p_0^n)$, and hence, for $(\delta \mathbf{u}_0^n, \delta p_0^n)$, we can determine the pair $(\delta \mathbf{u}^n, \delta p^n)$. Then, we can find the solution of problem $\mathscr{P}_{t_n}$ using Eqs. (5.3) and (5.4). Let $\bar{\mathbf{u}} = \mathbf{u}^m + \delta \mathbf{u}^n$ denote the approximation of the velocity field at this stage. The resulting approximation is obtained by downscaling, where $\bar{\mathbf{u}}$ defines fluxes on the interfaces of the domain decomposition, which are used as boundary conditions for the following local problems

$$\begin{cases} \tilde{\mathbf{u}}_h^i &= -\kappa^n \nabla \tilde{p}_h^i & \text{in } \Omega_i \\ \nabla \cdot \tilde{\mathbf{u}}_h^i &= q^i & \text{in } \Omega_i \\ \tilde{\mathbf{u}}_h^i \cdot \check{\mathbf{n}}^i &= \bar{\mathbf{u}}_h^i \cdot \check{\mathbf{n}}^i & \text{on } \partial\Omega_i \cap \partial\Omega \\ \tilde{\mathbf{u}}_h^i \cdot \check{\mathbf{n}}^i &= \bar{\mathbf{u}}_h^i \cdot \check{\mathbf{n}}^i & \text{on } \Gamma_{ij}\ \forall j \end{cases} \tag{5.10}$$

for all $\Omega_i,\ i = 1,2,\cdots,N$, where $\tilde{\mathbf{u}}$ is the final approximation for $\mathbf{u}^n$. We remark that these local problems are undefined up to a pressure constant. This indeterminacy is removed by imposing a value for the pressure variable at some point of the computational domain.

5.1.2 A modified operator splitting scheme

The operator splitting scheme for two-phase flows calls for an updated velocity field at times $t_n = n\Delta t_p$, for $n = 0,1,\ldots$. We propose a modification in the algorithm to incorporate the option of choosing between the MRCM and MPM at the elliptic solution steps.

In order to explain our modified operator splitting algorithm, let $\{\Phi^m,\Psi^m\}$ denote the set of basis functions $\{\phi_1,\phi_2,\cdots,\phi_{N_U}\}$ and $\{\psi_1,\psi_2,\cdots,\psi_{N_P}\}$ built by the MRCM to solve the problem $\mathscr{P}_{t_m}$ (5.1), associated with time t_m. We compute p^0 and $\mathbf{u}^0$ with the MRCM and store the set of BFs $\{\Phi^0,\Psi^0\}$, such that we can use these basis functions to solve problems $\mathscr{P}_{t_n}$ (5.2), at times $t_1,t_2,\ldots$.

The closer the field κ^m is to the field κ^n, the more accurate is the approximation provided by the MPM (ALSADIG *et al.*, 2020). Since the field κ^n takes into account an updated saturation, it can be far from κ^m depending on the changes due to the displacement of oil by water interface throughout the domain. The difference between κ^n and κ^m is given by $\varepsilon = ||\kappa^n - \kappa^m||_{L^2(\Omega)}$. We intend to impose a tolerance for ε values in the modified operator splitting scheme to control the difference between κ^n and κ^m. For this purpose, we may need to update the BFs more than once throughout the simulation. Thus, we propose to separate the elliptic solutions into two cases: the case when the BFs are reused by the MPM and the case when a full update of the BFs is required. The latter is computed directly by the MRCM.

We start a two-phase flow simulation with the solutions p^0 and $\mathbf{u}^0$ computed by the MRCM, and the corresponding set of BFs $\{\Phi^0,\Psi^0\}$ stored. We use these basis functions to solve problems $\mathscr{P}_{t_n}$ (5.2), at times $t_n = t_1,t_2,\cdots,t_{m_1-1}$, where t_{m_1} is the first time such that $\varepsilon > \eta$ (η is the chosen tolerance). At time t_{m_1} we compute p^{m_1} and $\mathbf{u}^{m_1}$ by the MRCM and store the updated set of BFs $\{\Psi^{m_1},\Phi^{m_1}\}$. Then, we use these BFs to solve problems $\mathscr{P}_{t_n}$, at times $t_n = t_{m_1+1},t_{m_1+2},\cdots,t_{m_2-1}$, where t_{m_2} is the next time when $\varepsilon > \eta$, hence we compute p^{m_2}, $\mathbf{u}^{m_2}$ and the updated set of BFs by the MRCM. We repeat this procedure until the final simulation time. We remark that all the equations considered by the MPM-2P are in dimensionless form, see (ALSADIG *et al.*, 2020; MANKAD, 2020) for more details. The MPM-2P algorithm is summarized in Algorithm 3, where T_e denotes the total of elliptic solutions computed.

5.1.3 Computational cost of the MPM-2P

To compare the computational cost of the MRCM and MPM-2P in the solution of the elliptic equations arising within the operator splitting algorithm we start by computing the number of BFs required by them, considering a problem with a domain decomposition with

Algorithm 3 – Solving equations (2.1)-(2.2) by the modified operator splitting

Given $s^0(\mathbf{x})$, compute $\kappa^{m_0=0} = \lambda(s^0(\mathbf{x}))$
Compute $p^0(\mathbf{x})$ and $\mathbf{u}^0(\mathbf{x})$ from Eq. (2.1) by using the MRCM
Store the set of BFs $\{\Psi^{m_0=0}, \Phi^{m_0=0}\}$
Set $n = 1$, $\ell = 0$, and $\varepsilon = \eta$
while $n < T_e$ **do**
    for $k \in \{1, \cdots, C_{n-1}\}$ **do**
        $t_{n-1,k} = t_{n-1} + k\Delta t_s$ ▷ $t_{n-1} < t_{n-1,k} \leq t_n$
        Solve Eq. (2.2) to compute $s(\mathbf{x}, t_{n-1,k})$ ▷ Using the first order upwind method
    end for
    Given $s^n(\mathbf{x})$, update $\kappa^n = \lambda(s^n(\mathbf{x}))$
    if $\varepsilon > \eta$ **then**
        $\ell = \ell + 1$ ▷ Counter for the updates of the BFs
        Compute $p^{n=m_\ell}(\mathbf{x})$ and $\mathbf{u}^{n=m_\ell}(\mathbf{x})$ from Eq. (2.1) by using the MRCM
        Store the updated set of BFs $\{\Psi^{m_\ell}, \Phi^{m_\ell}\}$
        Update $\kappa^{m_\ell} = \lambda(s^{n=m_\ell}(\mathbf{x}))$
    else
        Compute $p^n(\mathbf{x})$ and $\mathbf{u}^n(\mathbf{x})$ from Eq. (2.1) with the MPM, reusing BFs $\{\Psi^{m_\ell}, \Phi^{m_\ell}\}$
    end if
    Compute $\varepsilon = \| \kappa^n - \kappa^{m_\ell} \|_{L^2(\Omega)}$
    $n = n + 1$
end while

$N = N_x \times N_y$ subdomains (2D). In order to find the number of BFs required for each method in the approximation of the two-phase flow problem, let us consider that a total of T_e elliptic solutions need to be computed. Note that:

- *Number of BFs required for an elliptic solution:*

  The number of BFs required by the MRCM in each subdomain is $\hat{N} = 4 \times (k_U + k_P)$ homogeneous BFs for each one of the edges of the subdomain, plus one non-homogeneous basis function. This number may be less for some subdomains due to physical boundary conditions. To compute the total amount of BFs, we multiply $\hat{N} + 1$ by the number of subdomains N (in a serial mode implementation). Note that this estimation considers all subdomains having the same degrees of freedom per interface, but in practice, we allow for local choices of degrees of freedom.

  The MPM requires only the calculation of the basis function for the non-homogeneous part of the solution in each subdomain. Therefore, we have a total of N BFs.

- *Number of BFs for the coupled flow and transport problem:*

  The number of BFs required by the MRCM for two-phase flows is $(\hat{N} + 1) \times N \times T_e$.

  To compute the total of BFs required by the MPM we have to separate the cases when the basis functions are reused from the cases when a full update is required.

1. Let T_m be the total number of updates required by the MPM (associated with the counter ℓ at line 12 of Algorithm 3). If we compute each update with the MRCM (considering the same number of BFs), the total number of BFs required by the updates of the MPM is $(\hat{N}+1)\times N\times T_m$.
2. The total of BFs computed when reusing the basis functions is $(T_e - T_m)\times N$.

Therefore, the total number of BFs computed by the MPM is $[(\hat{N}+1)\times T_m + (T_e - T_m)]\times N$.

To estimate the overall cost of the methods we have to consider the cost of computing the BFs, downscaling, and a global interface problem. Let $\mathscr{C}_{BF}$, $\mathscr{C}_{DS}$ and $\mathscr{C}_I$ be, respectively, the estimated computational cost to compute one basis function, the downscaling in a subdomain, and the global interface problem. We define the cost estimate of the MRCM as follows:

$$\begin{aligned}\text{cost(MRCM)} &= \left[\mathscr{C}_{BF}\times(\hat{N}+1)\times N + \mathscr{C}_{DS}\times N + \mathscr{C}_I\right]\times T_e \\ &\approx \mathscr{C}_{BF}\times(\hat{N}+2)\times N\times T_e.\end{aligned} \tag{5.11}$$

This approximation follows from the fact that the computational cost of the interface problem is typically negligible when compared to the cost of computing BFs (FERRAZ, 2019). Furthermore, the downscaling step has essentially the same cost of computing one basis function at each subdomain ($\mathscr{C}_{DS}\approx\mathscr{C}_{BF}$). Thus, the cost estimate of the MPM is given by:

$$\begin{aligned}\text{cost(MPM)} &= \left[\left(\mathscr{C}_{BF}\times(\hat{N}+1)+\mathscr{C}_{DS}\right)\times T_m + (\mathscr{C}_{BF}+\mathscr{C}_{DS})\times(T_e - T_m)\right]\times N + \mathscr{C}_I\times T_e \\ &\approx \left[\mathscr{C}_{BF}\times(\hat{N}+2)\times T_m + 2\times\mathscr{C}_{BF}\times(T_e - T_m)\right]\times N.\end{aligned} \tag{5.12}$$

We define a quantity to indicate the relation between the computational cost of the methods. The following quantity (referred to as Relative Gain) measures the relative cost reduction accomplished by the MPM-2P when compared with the approximation of two-phase flows directly by the MRCM.

$$\begin{aligned}\text{Relative Gain} &= \frac{\text{cost(MRCM)-cost(MPM)}}{\text{cost(MRCM)}}100\% \\ &= \frac{\left[\left(\mathscr{C}_{BF}\times(\hat{N}+2)\right)\times(T_e - T_m) - 2\times\mathscr{C}_{BF}\times(T_e - T_m)\right]\times N}{\mathscr{C}_{BF}\times(\hat{N}+2)\times N\times T_e}100\% \\ &= \frac{T_e - T_m}{T_e}\left[1 - \frac{2}{\hat{N}+2}\right]100\%.\end{aligned} \tag{5.13}$$

Let us consider as an example a domain decomposition of 11×6 subdomains for the permeability field illustrated in Figure 13 (which contains a high-permeable channel and a low-permeable region), that is used in some of the numerical experiments below. If we consider

the MRCM with linear interface spaces for both flux and pressure, i.e. $k_U = k_P = 2$, the number of homogeneous BFs to be computed is $\hat{N} = 16$ per subdomain. In order to find the Relative Gain for a two-phase flow problem, let us consider that a total of $T_e = 200$ elliptic solutions need to be computed. This is typically the order of the number of elliptic solutions needed to reach water breakthrough in some of our simulations with the permeability field at hand. We find in our numerical experiments that approximately 8 updates are required by the MPM for this type of problem. Therefore, the Relative Gain is given by

$$\text{Relative Gain} \quad = \frac{T_e - T_m}{T_e}\left[1 - \frac{2}{\hat{N}+2}\right]100\% = \frac{200-8}{200}\left[1 - \frac{2}{16+2}\right]100\% \approx 85.33\%. \tag{5.14}$$

We find in our numerical studies that the MPM-2P shows outstanding speed-up. It reduces significantly the cost of the simulation of two-phase flow problems when compared to the traditional operator splitting combined with the MRCM. The Relative Gain of 85.33% is the least value that we find in the numerical studies reported here, since we consider more basis functions in other experiments, that further increases the advantage of using the MPM-2P.

5.2 Numerical experiments

In this section, we present numerical simulations to investigate the accuracy as well as the cost of the MPM-2P. We consider challenging two-phase flow problems, with a high-contrast permeability field (described in subsection 5.2.1), and water-oil finger growth in a homogeneous medium (discussed in subsection 5.2.2). Some of our preliminary results obtained for slightly simpler cases of two-phase flows considering Gaussian permeability fields are reported in (MANKAD, 2020).

In all simulations, we set the same quadratic relative permeabilities considered in the experiments of the previous chapters. The time is considered in PVI, and the results are presented in terms of the number of elliptic solutions.

5.2.1 A high-contrast permeability field

The first experiment considers the high-contrast permeability field containing a high-permeable channel and a low-permeable region illustrated in Figure 13. The domain $\Omega = [0, 33/12] \times [0, 3/2]$ is divided into 11×6 subdomains with 15×15 cells into each one. The flow is established by imposing unit flow at the left boundary and zero pressure at the right boundary along with no-flow at top and bottom. No source terms are considered. We consider that the porous medium is initially filled with oil and water is injected at a constant rate. The viscosity ratio is set to $M = 40$.

Our objective is to compare the approximations provided by the MPM-2P and the MRCM. Concerning the MRCM, we consider the *a*MRCM-PBS discussed in section 4.2, which

corresponds to the adaptive version with physics-based interface spaces. We use the physics-based interface spaces for pressure to accommodate the high-permeable regions and the physics-based interface spaces for flux to accommodate the barriers. Moreover, the adaptivity of the MRCM considers $\alpha_{\text{small}} = 10^{-2}$ for regions of high-permeability and $\alpha_{\text{large}} = 10^{2}$ for the remaining regions (see section 4.2). We remark that the local values of $\alpha(\mathbf{x})$ are set only once in an offline step. Figure 47 shows the map of the permeability variations at the boundaries of the subdomains. The red color refers to regions of high-permeability, where the pressure physics-based interface spaces are used. The cyan color denotes the regions of low-permeability, where we consider the flux physics-based interface spaces. In the remaining subdomain boundaries we consider linear interface spaces. The values of $\alpha_{\text{small}} = 10^{-2}$ are set at the subdomain boundaries in red while $\alpha_{\text{large}} = 10^{2}$ is set in all the remaining subdomain boundaries. The downscaling procedure used is the stitch method, see (GUIRALDELLO *et al.*, 2020) for details about this scheme.

Figure 47 – Map of the permeability variations at the boundaries of the subdomains. The red color identifies regions of high-permeability and the cyan color represents the regions of low-permeability. Note that the channelized structures are well captured by our procedure.

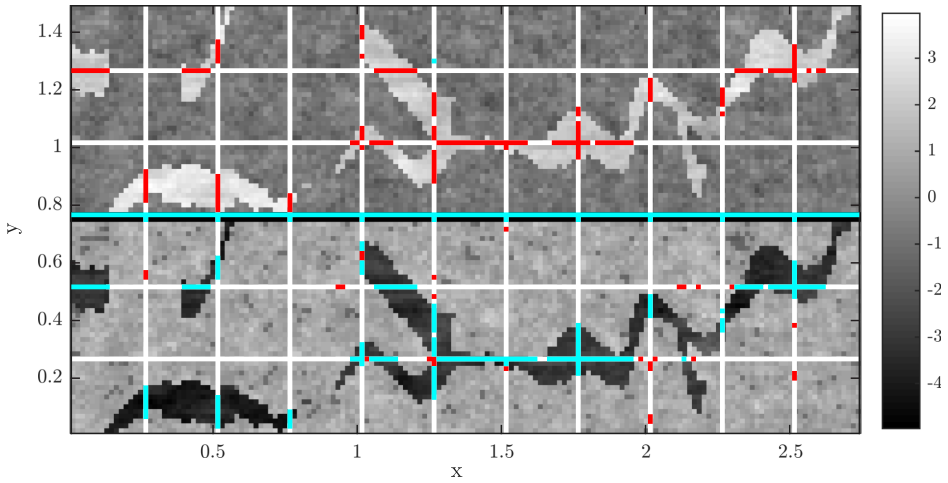

Source: Research data.

In the numerical results we have approximately 20 transport steps between successive elliptic updates for both methods. Figure 48 shows the relative $L^2(\Omega)$ errors for flux (left) and relative $L^1(\Omega)$ errors for saturation (right) as a function of the number of elliptic solutions. The errors are computed with respect to a reference fine grid solution. In this figure, the breakthrough time for the fine grid solution is indicated by a vertical dashed line. We compare the errors of the MRCM and the MPM-2P with a tolerance of $\eta = 10^{-2}$ for the values of ε, in line with (ALSADIG *et al.*, 2020). In both cases (computation directly by the MRCM or the MPM-2P updates) we consider the *a*MRCM-POL and the *a*MRCM-PBS. The nodes on each of the MPM-2P curves indicate the times when the BFs are updated. The set of BFs was computed 10 times by the MPM-2P (the initial set plus 9 updates), that is significantly less than the total of 410 full updates required by the MRCM. As expected, the *a*MRCM-PBS (and respectively the MPM-2P that considers the *a*MRCM-PBS) is more accurate than the *a*MRCM-POL (respectively the

MPM-2P considering the *a*MRCM-POL). Note that the errors of the MPM-2P are equal to the errors of the MRCM at the updates, while the first is more accurate than the MRCM when the BFs are reused. This result indicates that a larger value for the tolerance η can be chosen. The MPM-2P benefits from the physics-based spaces since its advantage over the MRCM is more significant when using these spaces rather than polynomial spaces.

Figure 48 – Relative $L^2(\Omega)$ errors for flux (left) and relative $L^1(\Omega)$ errors for saturation (right) as a function of the number of elliptic solutions. We consider physics-based and polynomial interface spaces and compare the MRCM and the MPM-2P (with $\eta = 10^{-2}$). The nodes on each of the MPM-2P curves indicate the times when the BFs are updated. The breakthrough time is illustrated by a vertical dashed line. Note that the MPM-2P shows improved accuracy using physics-based interface spaces.

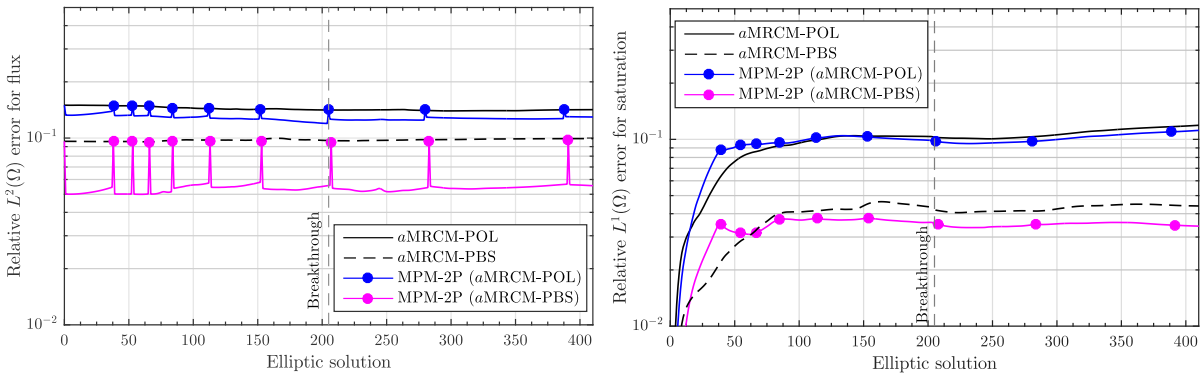

Source: Research data.

In Figure 49 we include two results for the MPM-2P combined with the *a*MRCM-PBS: by considering no tolerance and setting $\eta = 0.05$. If no tolerance is demand, i.e. no updates of the BFs are made, the errors increase and cannot be bounded. In contrast, the tolerance of $\eta = 0.05$ controls the errors without requiring many updates. In this case, only three computations of the set of BFs were needed (the initial set and two updates). The breakthrough could be simulated with only one update, that represents an exceptional speed-up of two-phase flow simulations, without loss of accuracy. Note that the saturation errors of the MPM-2P combined with the *a*MRCM-PBS for $\eta = 0.05$ are smaller than the errors of the *a*MRCM-POL, which is extremely more expensive. The behavior of ε throughout the simulation can be found in Figure 50, where we point out the tolerance criterion controlling its values.

To close this discussion, we compare the methods in terms of their saturation profiles in Figure 51. We show saturation plots for the fine mesh, *a*MRCM-POL, *a*MRCM-PBS, and the MPM-2P considering $\eta = 0.01$ (combined with the *a*MRCM-POL and *a*MRCM-PBS) and $\eta = 0.01$ (combined with the *a*MRCM-PBS). The profiles are taken at time $T_{\mathbf{PVI}} = 0.06$, that corresponds to the breakthrough time, i.e. 205 elliptic solutions. Note that the improvement provided by the *a*MRCM-PBS to the *a*MRCM-POL is reflected by the MPM-2P, that uses these methods for the updates (for $\eta = 0.01$). The procedures that produce a saturation solution closer to the reference are the *a*MRCM-PBS and the MPM-2P that uses the *a*MRCM-PBS and

Figure 49 – Relative $L^2(\Omega)$ errors for flux (left) and relative $L^1(\Omega)$ errors for saturation (right) as a function of the number of elliptic solutions. We consider physics-based interface spaces and compare the MRCM and the MPM-2P (with no tolerance, $\eta = 0.01$, and $\eta = 0.05$). The nodes on each of the MPM-2P curves indicate the times when the BFs are updated. The breakthrough time is illustrated by a vertical dashed line. Note that the MPM-2P does not require many updates, and its errors are controlled by the tolerance criteria for ε.

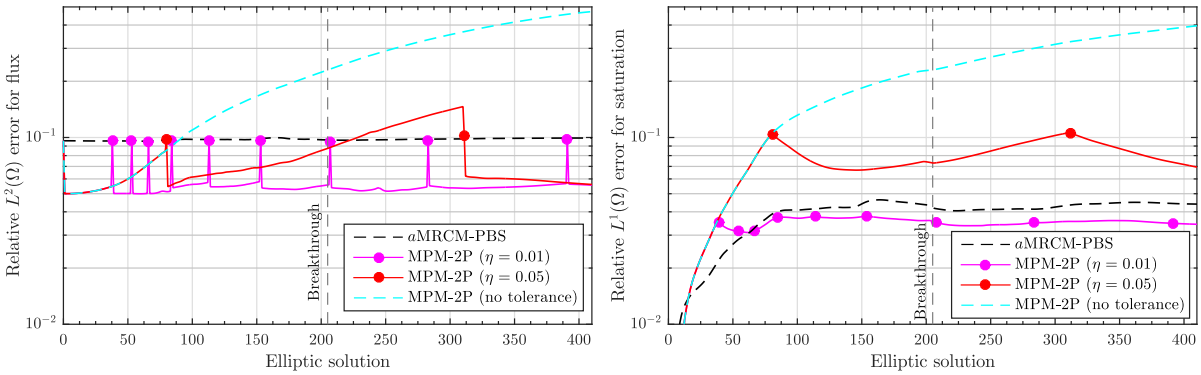

Source: Research data.

Figure 50 – Behavior of ε throughout the simulation controlled by three different tolerance criteria (no tolerance, $\eta = 0.01$, and $\eta = 0.05$).

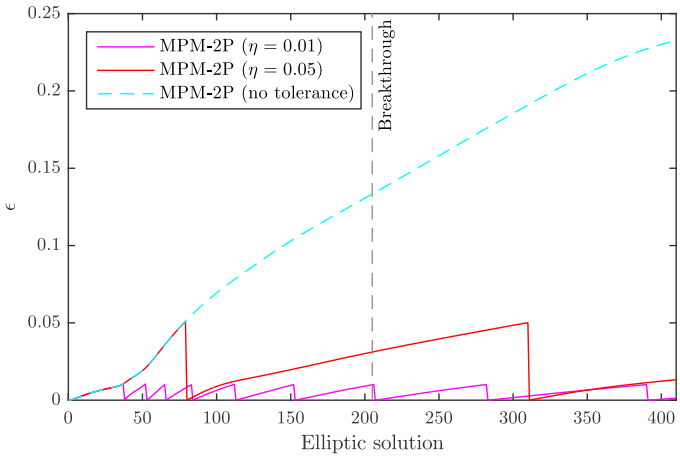

Source: Research data.

considers $\eta = 0.01$. We remark that the latter is much less expensive than the first. The MPM-2P that uses the *a*MRCM-PBS and considers $\eta = 0.05$ is even less expensive, demonstrating only small inaccuracies when compared to the approximation with tolerance $\eta = 0.01$. Therefore, it is possible to produce an approximation of two-phase flows with accuracy controlled by a tolerance criterion for ε in addition to novel, unprecedented reduction of the computational cost.

5.2.2 Water-oil finger growth in a homogeneous medium

In this experiment, we test the MPM-2P in a case with an unstable interface of oil-water in a homogeneous medium. We consider an injection of water at the left boundary of the domain

Figure 51 – Saturation profiles at breakthrough time $T_{\mathbf{PVI}} = 0.06$ (that corresponds to 205 elliptic solutions). First line, left to right: fine grid solution; *a*MRCM-POL; *a*MRCM-PBS. Second line considers the MPM-2P, left to right: using the *a*MRCM-POL for the updates with $\eta = 0.01$; using the *a*MRCM-PBS for the updates with $\eta = 0.01$; using the *a*MRCM-PBS for the updates with $\eta = 0.05$. Note that the improvement provided by the *a*MRCM-PBS to the *a*MRCM-POL is reflected by the MPM-2P.

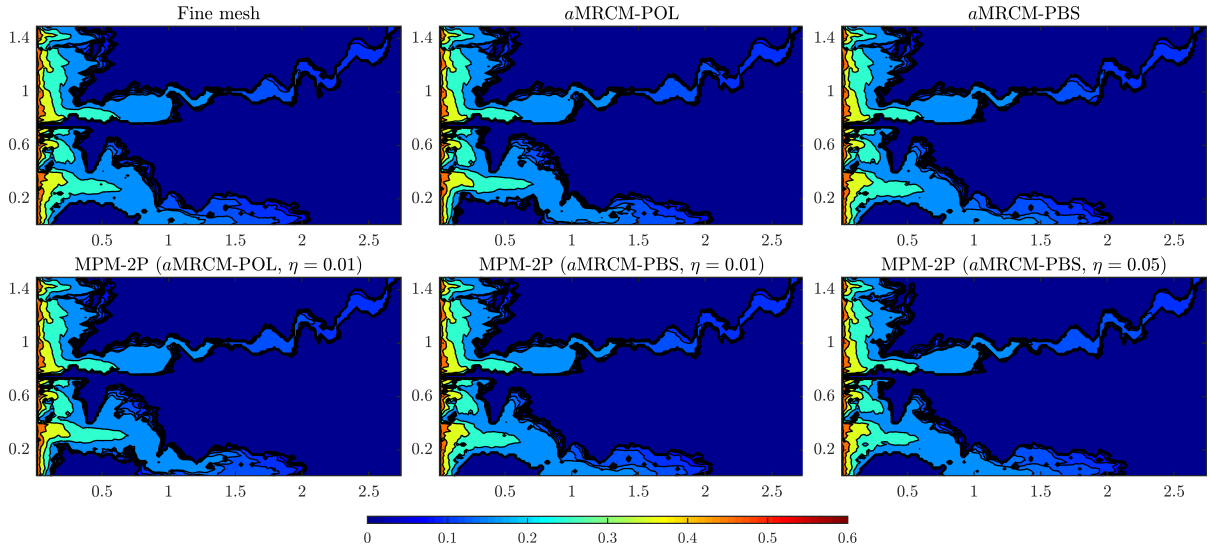

Source: Research data.

$\Omega = [0,3] \times [0,1/2]$, with an initial front fully saturated of water at the left and filled with oil at the right. The water front has a small perturbation at the center of the channel, as shown in Figure 52. This is a 2D Riemann problem with physical instabilities, similar to the studied in (GLIMM; MARCHESIN; MCBRYAN, 1981), where the authors have shown that a finger grows at the center of the channel and evolves in time for a viscosity ratio of $M = 4$. Here we consider the same value $M = 4$, that is close to the critical value for unstable flows ($M \approx 2.657$) as described in (FURTADO; PEREIRA, 2003). The boundary conditions considered are no-flow at the top and bottom along with an imposed pressure $p = 0$ on the left and $p = -10^4$ on the right boundaries. Furthermore, no source terms are considered.

Figure 52 shows the saturation evolution for times $T_{\mathbf{PVI}} = 0.00,\ 0.03,\ 0.19,\ 0.39,\ 0.66$ (corresponding to 1, 100, 600, 1100, and 1600 elliptic solutions, respectively), from top to bottom. The reference fine grid solution (left) and the MPM-2P approximation (right) are compared. The MPM-2P uses a domain decomposition of 15×5 subdomains, with 20×10 cells into each one. A full set of BFs is computed by the MRCM at the update steps required by the MPM-2P, which consider the tolerance of $\eta = 0.01$. Therefore, we do not have multiscale inaccuracies associated with the MRCM in this comparison (the MRCM produces the fine grid pressure solution). Inaccuracies associated with the operator splitting are reduced by setting $C_n = 1,\ \forall n$. We note that the MPM-2P and the fine grid approximations are closely related.

The relative $L^2(\Omega)$ error for flux and relative $L^1(\Omega)$ error for saturation as a function of the number of elliptic solutions can be found in Figure 53. A total of $T_e = 2000$ elliptic solutions

are considered, of which 63 correspond to updates of the BFs (indicated by the nodes). The trend of quickly increasing errors until the breakthrough time (that is illustrated by a dashed line) was controlled by the updates of the BFs. Note that a drop in the error for flux occurs every update. Even for this complex problem with physical instabilities, the MPM-2P decreases the number of full updates of the set of BFs from 2000 to 63. These results confirm the great potential the MPM-2P to reduce drastically the computational cost of two-phase flow simulations, without loss of accuracy.

Figure 52 – Saturation evolution for the Riemann problem with a small perturbation of the initial water-oil interface at the center of the domain. We show the fine grid solution (left) and the MPM-2P approximation (right) at times $T_{\mathbf{PVI}} = 0.00,\ 0.03,\ 0.19,\ 0.39,\ 0.66$ (corresponding to $1,\ 100,\ 600,\ 1100$, and 1600 elliptic solutions, respectively), from top to bottom. Note that the MPM-2P and the fine grid approximations are very close to each other.

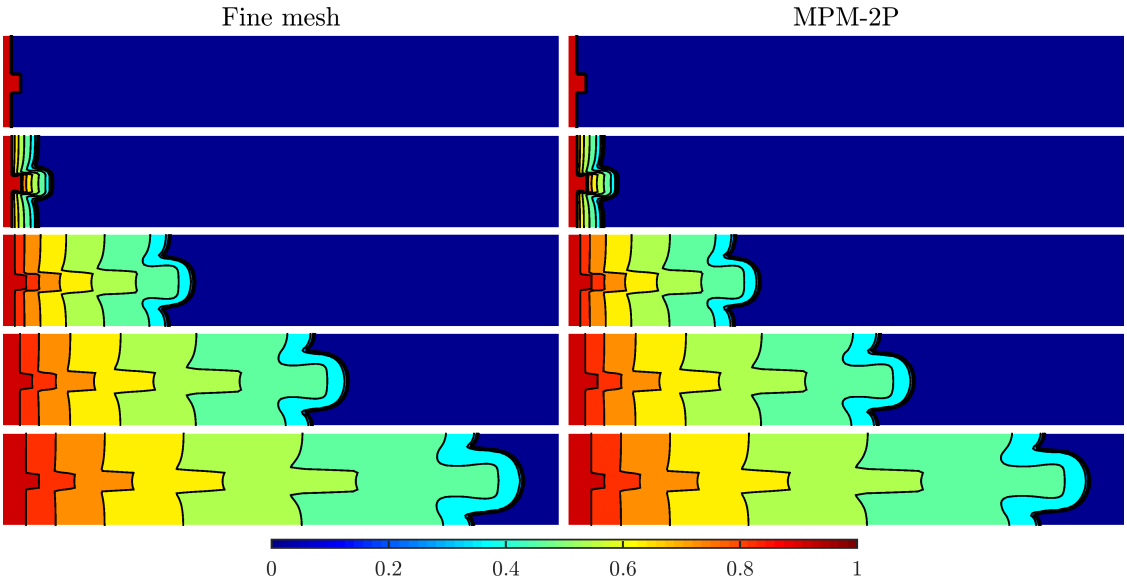

Source: Research data.

5.3 Discussion

The MPM-2P is proposed to speed-up the numerical simulation of two-phase flows in porous media.

Our numerical results are very encouraging. We consider challenging two-phase flow simulations and we find that the MPM-2P can reduce significantly the computational cost of the simulations, without loss of accuracy. The water breakthrough can be simulated with very few updates of the MRCM set of basis functions. The errors produced by the MPM-2P are at least comparable to the typical values of error attained by multiscale methods.

Although the new method is presented for two-phase flows it can also be applied to other types of flows, as well as to the sequential implicit solution of multiphase flows. Other multiscale mixed methods instead of the MRCM can also be considered in a straightforward manner.

Figure 53 – Relative $L^2(\Omega)$ error for flux and relative $L^1(\Omega)$ error for saturation as a function of the number of elliptic solutions for the Riemann problem with a small perturbation at the center of the domain. The trend of quickly increasing errors until the breakthrough time (illustrated by a dashed line) was controlled by the updates of the BFs (indicated by the nodes).

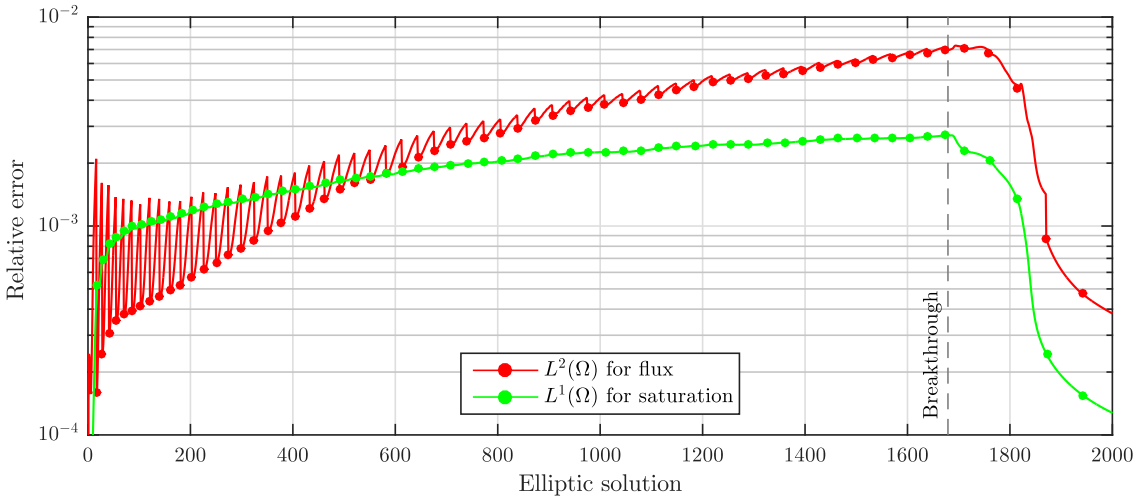

Source: Research data.

CHAPTER

6

A SEQUENTIAL IMPLICIT SOLVER

In all the previous chapters we have considered the approximation of the non-linear two-phase flows model by an operator splitting technique that uses explicit schemes. In this chapter, we consider an implicit scheme in a sequential fashion (WATTS, 1986). The implicit formulations allow for the use of arbitrarily large time steps when compared to explicit time integration approaches, especially in the presence of strong heterogeneities (JENNY; TCHELEPI; LEE, 2009; WANG; TCHELEPI, 2013).

We propose to test the performance of the MRCM combined with the Sequential Implicit (SI) approach for the transport problem (WATTS, 1986). The accuracy and efficiency of the proposed combination are investigated through numerical simulations of two-phase flows in heterogeneous reservoirs.

In the next section, we present the numerical approximations for the SI algorithm to solve the coupled equations (2.1)-(2.2). Then, we show our experimental results and discussions.

6.1 The sequential implicit scheme

In the SI algorithm, each time step consists of a sequential update for the coupled problems of flow and transport, where a (nonlinear) Newton loop is used to solve the transport problem implicitly. We denote by Δt the time step used to update the coupled problems of flow and transport at times $t^n = n\Delta t$, for $n = 0, 1, \ldots$, while ν refers to the iteration levels of the Newton loop for saturation.

Let $p^n(\mathbf{x})$, $\mathbf{u}^n(\mathbf{x})$ and $s^n(\mathbf{x})$ denote the pressure, velocity and saturation approximations for $p(\mathbf{x},t^n)$, $\mathbf{u}(\mathbf{x},t^n)$ and $s(\mathbf{x},t^n)$ respectively, at time t^n. The pressure $p^{n+1}(\mathbf{x})$ and velocity $\mathbf{u}^{n+1}(\mathbf{x})$ are sequentially updated by Eq. (2.1) using the saturation $s^{n+1}(\mathbf{x})$. The saturation $s^{n+1}(\mathbf{x})$ is computed through Eq. (2.2) by using a simple implicit Euler time integration considering $\mathbf{u}$

constant in time as follows

$$\frac{s^{n+1}-s^n}{\Delta t}+\nabla\cdot\left(f(s^{n+1})\mathbf{u}^n\right)=0. \tag{6.1}$$

We solve Eq. (6.1) by the Newton method, where the saturation at the new time level is taken when the maximum absolute change in the saturation between two successive iterations is less than a specified tolerance η. Specifically, we consider $s^{n+1,\nu=0}=s^n$ and compute Newton iterations until the convergence criterion $\max|s^{n+1,\nu+1}-s^{n+1,\nu}|\leq\eta$. Then, we take $s^{n+1}=s^{n+1,\nu+1}$.

To find $s^{n+1,\nu+1}$ through the transport equation

$$\frac{s^{n+1,\nu+1}-s^n}{\Delta t}+\nabla\cdot\left(f(s^{n+1,\nu+1})\mathbf{u}^n\right)=0, \tag{6.2}$$

we consider a finite volume discretization of the form

$$s_I^{n+1,\nu+1}=s_I^n-\frac{\Delta t}{\Delta\mathbf{x}}\left(\mathscr{F}_I^{n+1,\nu+1}\right), \tag{6.3}$$

where I refers to a computational cell of an orthogonal, uniformly spaced (by directions) grid identified as an index ($I=(i,j)$ in 2D and $I=(i,j,k)$ in 3D), and $\Delta\mathbf{x}$ represents the characteristic size of I ($\Delta\mathbf{x}=(\Delta x,\Delta y)$ in 2D and $\Delta\mathbf{x}=(\Delta x,\Delta y,\Delta z)$ in 3D). Here, $\mathscr{F}_I^{n+1,\nu+1}$ is a function of $f(s^{n+1,\nu+1})$ and $\mathbf{u}^n$, that represents the balance of quantities at the faces of cell I. Considering the following linearization

$$\mathscr{F}^{n+1,\nu+1}=\mathscr{F}^{n+1,\nu}+\left(\frac{d\mathscr{F}}{ds}\right)^{n+1,\nu}\left(s^{n+1,\nu+1}-s^{n+1,\nu}\right), \tag{6.4}$$

we have

$$\left[s^{n+1,\nu+1}-s^n+\frac{\Delta t}{\Delta\mathbf{x}}\left(\mathscr{F}^{n+1,\nu}+\left(\frac{d\mathscr{F}}{ds}\right)^{n+1,\nu}\left(s^{n+1,\nu+1}-s^{n+1,\nu}\right)\right)\right]_I=0 \tag{6.5}$$

that leads to

$$\left[\frac{\Delta t}{\Delta\mathbf{x}}\mathscr{F}^{n+1,\nu}+s^{n+1,\nu}-s^n+\left(\frac{\Delta t}{\Delta\mathbf{x}}\left(\frac{d\mathscr{F}}{ds}\right)^{n+1,\nu}+1\right)\left(s^{n+1,\nu+1}-s^{n+1,\nu}\right)=0\right]_I. \tag{6.6}$$

Equation (6.6) can be written as

$$\mathscr{H}(s^{n+1,\nu})+\mathscr{H}'(s^{n+1,\nu})\left(s^{n+1,\nu+1}-s^{n+1,\nu}\right)=0, \tag{6.7}$$

where

$$\mathscr{H}(s^{n+1,\nu})=\left[\frac{\Delta t}{\Delta\mathbf{x}}\mathscr{F}^{n+1,\nu}+s^{n+1,\nu}-s^n\right]_I \tag{6.8}$$

and $\mathscr{H}'(s^{n+1,\nu})$ is the Jacobian matrix. Therefore, the approximation of $s^{n+1,\nu+1}$ can be found by solving the linearized system

$$\mathscr{H}'(s^{n+1,\nu})\,\delta^\nu=-\mathscr{H}(s^{n+1,\nu}), \tag{6.9}$$

where $\delta^{\nu} = s^{n+1,\nu+1} - s^{n+1,\nu}$.

We consider a modification of the Newton iteration scheme proposed in (JENNY; TCHELEPI; LEE, 2009) to ensure the convergence for any time step size. This modification was introduced to deal with Newton initial guesses that are on the opposite side of the saturation inflection-point concerning the saturation solution. To ensure the convergence of the Newton iterative process two successive saturation updates are made on the same side of the saturation inflection-point. Hence, if an update would cross the inflection-point, selective under-relaxation is applied, i.e., if $f''(s^{n+1,\nu+1}) f''(s^{n+1,\nu}) < 0$, then $s^{n+1,\nu+1} = (s^{n+1,\nu+1} + s^{n+1,\nu})/2$. Additionally, it is necessary to enforce the constraint $0 \leq s^{n+1,\nu+1} \leq 1$ after every iteration, that is justified by the physics of the problem (JENNY; TCHELEPI; LEE, 2009).

Other developments of the modified Newton method include the use of trust-regions related to the flux function to guide the Newton iterations (WANG; TCHELEPI, 2013), and the development of a numerical trust-region solver, that is based on the discretized flux function (LI; TCHELEPI, 2015). However, in our context (two-phase flows without gravity and capillary effects) the infection-point strategy can be seen as a particular case of the above cited improvements.

The procedure to compute the approximate solutions for saturation $s^{n+1}(\mathbf{x})$, velocity $\mathbf{u}^{n+1}(\mathbf{x})$ and pressure $p^{n+1}(\mathbf{x})$ from the solutions at time t^n, is described in Algorithm 4.

Algorithm 4 – Solving equations (2.1)-(2.2) by the SI algorithm

Given $s^n(\mathbf{x})$, $p^n(\mathbf{x})$ and $\mathbf{u}^n(\mathbf{x})$ computed from previous time step
$\nu = 0$
$s^{n+1,\nu} = s^n$
step_size $= \eta$
while step_size $\geq \eta$ **do**
    Solve Eq. (6.9) to compute $s^{n+1,\nu+1}$ ▷ Newton linearization
    if $s^{n+1,\nu+1} > 1$ or $s^{n+1,\nu+1} < 0$ **then**
        Fix $s^{n+1,\nu+1} \in [0,1]$
    end if
    if $f''(s^{n+1,\nu+1}) f''(s^{n+1,\nu}) < 0$ **then** ▷ Fixing the saturation inflection-point
        $s^{n+1,\nu+1} = (s^{n+1,\nu+1} + s^{n+1,\nu})/2$
    end if
    step_size $= \max |s^{n+1,\nu+1} - s^{n+1,\nu}|$
    $\nu = \nu + 1$
end while
$s^{n+1} = s^{n+1,\nu+1}$
Given $s^{n+1}(\mathbf{x})$, update $\lambda(s^{n+1}(\mathbf{x}))$
Solve Eq. (2.1) to obtain $p^{n+1}(\mathbf{x})$ and $\mathbf{u}^{n+1}(\mathbf{x})$
Make $n \leftarrow n+1$ and return to step 1

We consider here a first order upwind scheme to define $\mathscr{F}_I^{n+1,\nu}$. For example, in 2D we

have

$$\mathscr{F}_I^{n+1,\nu} = \mathscr{F}_{i,j}^{n+1,\nu} = \frac{\Delta t}{\Delta x}\left(F_{i+1/2,j}^{n+1,\nu} - F_{i-1/2,j}^{n+1,\nu}\right) - \frac{\Delta t}{\Delta y}\left(G_{i,j+1/2}^{n+1,\nu} - G_{i,j-1/2}^{n+1,\nu}\right), \tag{6.10}$$

with discrete fluxes $F_{i-1/2,j}^{n+1,\nu}$ and $G_{i,j-1/2}^{n+1,\nu}$ on respective interfaces $x_{i-1/2}$ and $y_{j-1/2}$ given by

$$F_{i-1/2,j}^{n+1,\nu} = \begin{cases} f_{i-1,j}^{n+1,\nu} u_{i-1/2,j}^{x} & \text{if } u_{i-1/2,j}^{x} > 0 \\ f_{i,j}^{n+1,\nu} u_{i-1/2,j}^{x} & \text{otherwise} \end{cases} \tag{6.11}$$

and

$$G_{i,j-1/2}^{n+1,\nu} = \begin{cases} f_{i,j-1}^{n+1,\nu} u_{i,j-1/2}^{y} & \text{if } u_{i,j-1/2}^{y} > 0 \\ f_{i,j}^{n+1,\nu} u_{i,j-1/2}^{y} & \text{otherwise} \end{cases} \tag{6.12}$$

where $u^x = u^x(x,y)$ and $u^y = u^y(x,y)$ denote the x and y components of the velocity field $\mathbf{u}$, and $f_{i,j}^{n+1,\nu} = f(s_{i,j}^{n+1,\nu})$. The variable $s_{i,j}^{n+1,\nu} = s(x_i, y_j, t^{n+1})$ represents the saturation (assumed to be a piecewise constant over each computational cell) at time $t = t^{n+1}$ and at Newton iteration ν.

6.1.1 Implicit versus explicit

The modified Newton method considered is unconditionally convergent, allowing for arbitrary sizes of time steps. Thus, the choice for the size of the time step is based only on accuracy requirements.

One can take much larger time steps with the implicit method when compared to explicit schemes. This is illustrated in Figure 54, where we compare the convergence of the saturation provided by the modified Newton method (implicit) and by the explicit operator splitting scheme considered in the previous chapters. Here, the explicit approach fixes the same time step size for both elliptic and hyperbolic equations and does not use extrapolations of the velocities. We consider a high-contrast permeability field with a flow established by imposing flux boundary conditions from left to right and no-flow at top and bottom. The domain $\Omega = [0,1] \times [0,1]$ (with 30×30 fine grid cells) is initially filled with oil and water is injected at a constant rate. In this chapter, we set the tolerance of the size of step as $\eta = 10^{-6}$, the viscosity ratio $M = 10$, and the same quadratic relative permeabilities considered in all the experiments of the previous chapters. Figure 54 shows the log-scaled permeability filed (left), the saturation solution at the final time $T_{\mathbf{PVI}} = 0.0625$ (center), and the relative $L^1(\Omega)$ error for saturation as a function of the size of the time step (right). The time steps considered have size varying from $\Delta t = 9.75 \times 10^{-6}$ to $\Delta t = 1.25 \times 10^{-3}$, while the reference solutions consider $\Delta t = 10^{-6}$ (the time is expressed in PVI). We compute the error for the explicit (respectively implicit) scheme considering the explicit (resp. implicit) reference. The L^1 difference between the explicit and implicit references is approximately 10^{-6}. One can note that the errors are essentially the same for the time step sizes smaller than the CFL restriction ($\Delta t \leq \Delta t_{CFL} \approx 7.8 \times 10^{-5}$). The explicit scheme cannot handle $\Delta t > \Delta t_{CFL}$, while the implicit method maintains the same behavior (linear slope) for the

Figure 54 – Log-scaled permeability field (left), saturation reference solution at the final time $T_{\mathbf{PVI}} = 0.0625$, and the relative $L^1(\Omega)$ error for saturation as a function of the size of the time step (right). The convergence behavior of the explicit and implicit schemes is the same for $\Delta t \leq \Delta t_{CFL}$ (linear slope), while only the implicit approximation is possible for larger sizes of time steps. The L^1 difference between the explicit and implicit references is approximately 10^{-6}.

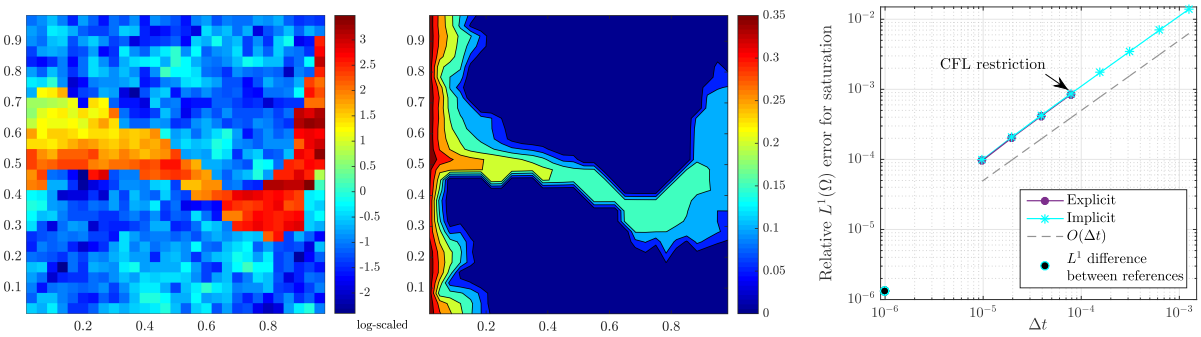

Source: Research data.

larger sizes of time steps. The average number of required Newton iterations per time step for the cases simulated vary from 2.36 for the smallest time step size to 6.5 for the largest one.

We remark that the time step restrictions in explicit discretizations can be avoided for the elliptic problem by using the operator splitting technique with larger time steps for the elliptic equation than those used for the hyperbolic problem, as we have considered in the previous chapters.

6.1.2 Alternatives to the implicit solver

The modified Newton solver described above can bee seen as a trust-region method that defines different saturation regions delineated by the inflection-point. The updates are performed such that two successive iterations cannot cross any trust-region boundary. A more general trust-region Newton method, that adds buoyancy and capillary effects, is presented in (WANG; TCHELEPI, 2013). In this subsection, we investigate trust-region methods based on least-square algorithms (NOCEDAL; WRIGHT, 2006) for the implicit solver.

Nonlinear equations are closely related to nonlinear least-squares problems. We consider trust-region methods to define the iterative step of the implicit solver by minimizing a model function in a selected region (YUAN, 2015). To explain the approach, consider the unconstrained minimization problem

$$\min_{\mathbf{x}\in\mathbb{R}^n} \varphi(\mathbf{x}), \tag{6.13}$$

where $\varphi : \mathbb{R}^n \longmapsto \mathbb{R}$ is the objective function to be minimized. The trust-region algorithm at iteration ν consists in finding a candidate direction of search $\mathbf{d}$ by solving the following subproblem

$$\min_{\mathbf{d}}\{m^{\nu}(\mathbf{d});\ \| \mathbf{d} \| \leq \Delta^{\nu},\ \mathbf{d} \in \mathbb{R}^n\}, \tag{6.14}$$

where m^ν is a model function that represents φ near the current point $\mathbf{x}^\nu$ and Δ^ν is the trust-region radius, that is adjusted every iteration to produce a sufficient decreasing approximation ($\varphi(\mathbf{x}^\nu + \mathbf{d}) < \varphi(\mathbf{x}^\nu)$). The model function is usually defined to be a quadratic function of the form

$$m^\nu(\mathbf{d}) = \frac{1}{2}\mathbf{d}^T \mathbf{B}^\nu \mathbf{d} + \mathbf{d}^T \nabla\varphi(\mathbf{x}^\nu), \tag{6.15}$$

where $\mathbf{B}^\nu$ is the Hessian matrix $\nabla^2\varphi(\mathbf{x}^\nu)$ or an approximation to it (NOCEDAL; WRIGHT, 2006).

We consider a trust-region reflective algorithm, that restricts $\mathbf{d}$ to a two-dimensional trust-region subspace spanned by the gradient direction $\nabla\varphi(\mathbf{x}^\nu)$ and the Newton direction $\mathbf{B}^\nu\mathbf{d} = -\nabla\varphi(\mathbf{x}^\nu)$ (BYRD; SCHNABEL; SHULTZ, 1988). The Newton system is computed by applying the preconditioned conjugate gradient method (BRANCH; COLEMAN; LI, 1999).

In the context of nonlinear system of equations of the form $\mathscr{H}(s) = 0$, the model function is a scalar-valued function obtained by combining the components of the vector $\mathscr{H}$. For example, we have the following trust-region subproblem

$$\min_{\mathbf{d}} \left\{ m^\nu(\mathbf{d}) = \frac{1}{2}\left\| \mathscr{H}(s^\nu) + \mathscr{H}'(s^\nu)\mathbf{d} \right\|_2^2 \; ; \; \| \mathbf{d} \| \leq \Delta^\nu, \; \mathbf{d} \in \mathbb{R}^n \right\}, \tag{6.16}$$

for the Newton iteration of Eq. (6.9) (skipping the time notation) (CONN; GOULD; TOINT, 2000).

We consider a trust-region dogleg algorithm to compute the search direction from a combination of Cauchy and Newton steps, as presented in (POWELL, 1968). The Cauchy step $\tilde{\mathbf{d}}$ minimizes the model function m^ν in Eq. (6.16) along the steepest descent direction (direction of the negative gradient), while the Newton step δ^ν is given by the iteration of Eq. (6.9). The dogleg algorithm chooses $\mathbf{d} = \tilde{\mathbf{d}} + \chi(\delta^\nu - \tilde{\mathbf{d}})$, where χ is the largest value in $[0,1]$ such that $\| \mathbf{d} \| \leq \Delta^\nu$. Additionally, we consider the Newton method with a global under-relaxation factor of 0.5 and refer to the modified Newton method with under-relaxation at the inflection-points as the local under-relaxation scheme. The Newton method with global under-relaxation is stable, but requires significantly more iterations to converge when compared to the Newton method with local under-relaxation (JENNY; TCHELEPI; LEE, 2009).

6.2 Numerical experiments

In this section, we present numerical experiments to study the performance of the implicit solver in the approximation of two-phase flows. Initially, we compare the implicit approximations provided by the trust-region algorithms mentioned above. Then, we consider a multiscale approximation, where we combine the MRCM with the sequential implicit solver.

We consider the same numerical set-up of the experiment in subsection 6.1.1, changing only the permeability field and, consequently, adapting the domain and time step.

6.2.1 A comparison of implicit solutions

We investigate the behavior of the trust-region algorithms for a two-phase flow problem. We consider a permeability field given by $K(\mathbf{x}) = 0.8e^{4.5\xi(\mathbf{x})}$, where $\xi(\mathbf{x})$ is a self similar Gaussian distribution having zero mean and the covariance function given by $C(\mathbf{x},\mathbf{y}) = |\mathbf{x}-\mathbf{y}|^{-1/2}$. For this field, the permeability contrast is $K_{\max}/K_{\min} \approx 10^6$ and the computational grid has 64×64 cells distributed in $\Omega = [0,1] \times [0,1]$. Figure 55 shows the log-scaled permeability field (left) and the convergence histories of one time step of size $\Delta t = 0.008 \approx 40\Delta t_{CFL}$ (right). We note that the number of required iterations for the Newton method with local under-relaxation is the smallest, followed by the trust-region reflective and dogleg schemes, which present a similar performance. The Newton method with global under-relaxation is the procedure that requires more iterations to converge. A related result comparing the Newton method with local and global under-relaxation has been presented in (JENNY; TCHELEPI; LEE, 2009).

Figure 55 – Log-scaled permeability field (left) and convergence histories of one time step of size $\Delta t = 0.008 \approx 40\Delta t_{CFL}$ (right). The Newton method with local under-relaxation is the procedure that requires the smallest number of iteration.

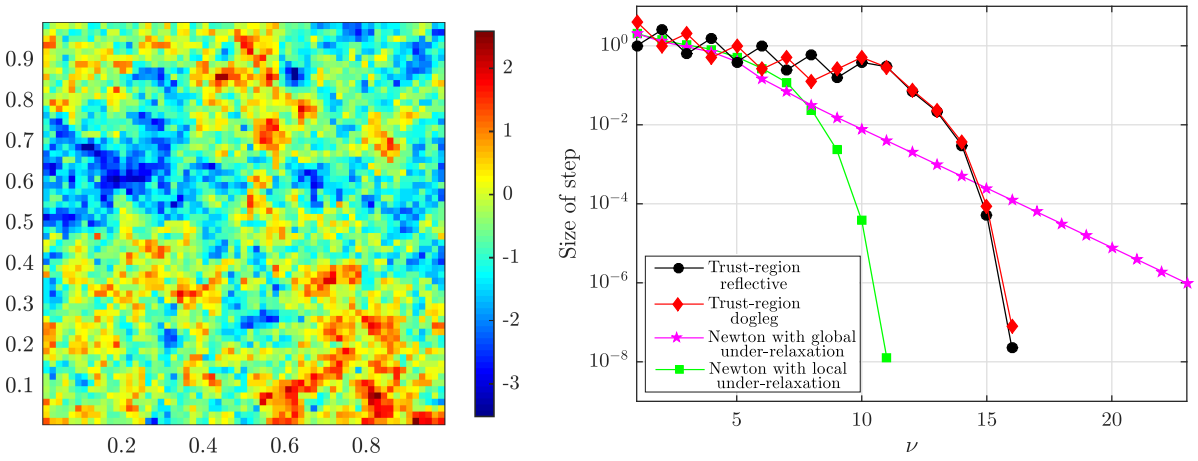

Source: Research data.

In order to investigate the behavior of the methods over time, we show in Figure 56 the number of iterations required in a simulation with final time $T_{\mathbf{PVI}} = 0.5$. Different choices of size of time step (related to $\Delta t_{CFL} \approx 1.9 \times 10^{-4}$) are considered. We present results for Δt chosen as $10\Delta t_{CFL}$, $40\Delta t_{CFL}$, $160\Delta t_{CFL}$ and $640\Delta t_{CFL}$, which generate, respectively, 256, 64, 16 and 4 time steps. Typically, the first time step requires more iterations than the following steps. For small values of Δt, the Newton methods with global and local under-relaxation require more iterations than the trust-region reflective and dogleg schemes. On the other hand, the Newton method with local under-relaxation requires fewer iterations than all the other procedures (that are comparable) for the largest value of Δt. These results are summered in Figure 57, where the total accumulated of iterations is shown.

Next, we consider the layer number 36 of the SPE10 project, that has a high-permeable channel and permeability contrast of $K_{\max}/K_{\min} \approx 10^6$. The domain for this example is $\Omega =$

Figure 56 – Number of iteration required as a function of time (in PVI). Different choices of size of time step as multiples of Δt_{CFL} are shown.

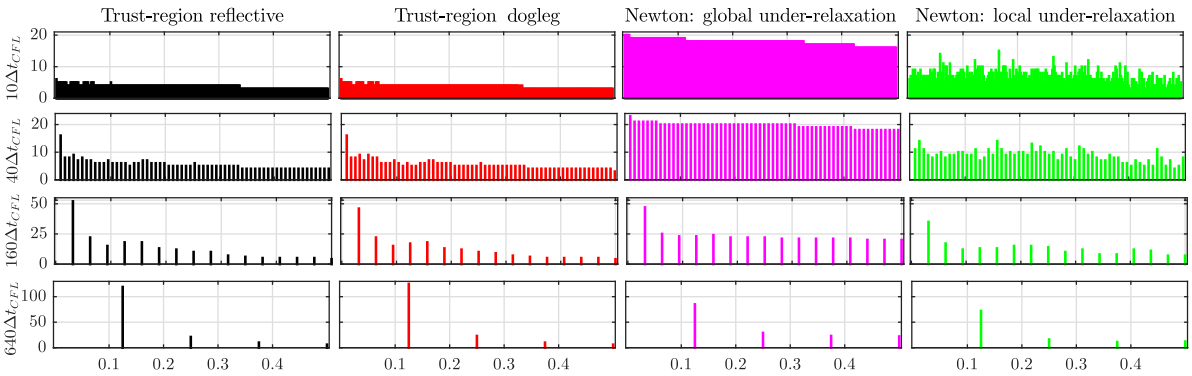

Source: Research data.

Figure 57 – Total accumulated of iterations at the final time $T_{\mathbf{PVI}} = 0.5$ for different choices of size of time step. Note that the Newton method with local under-relaxation is the procedure that requires fewer iterations for the largest Δt considered.

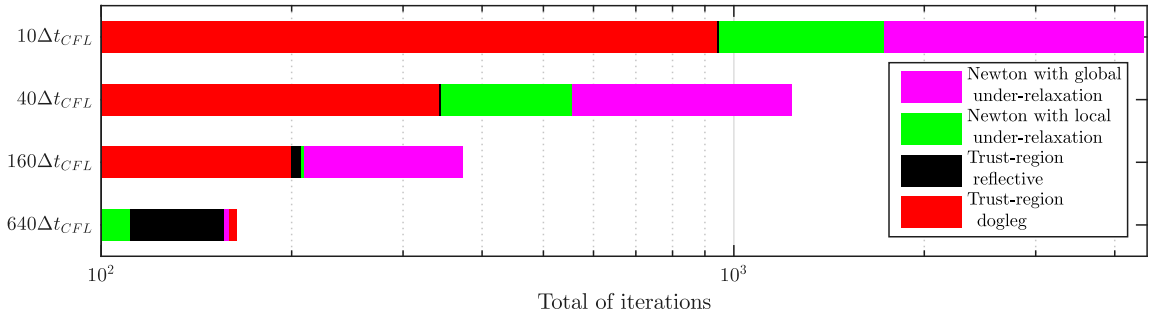

Source: Research data.

$[0, 11/3] \times [0, 1]$ with 220×60 fine grid cells. Figure 58 shows the total accumulated of iterations until time $T_{\mathbf{PVI}} = 0.11$ for different sizes of time step taken as multiples of $\Delta t_{CFL} \approx 1.3 \times 10^{-5}$. We start with $\Delta t = 32\Delta t_{CFL}$ (that corresponds to 256 time steps) and multiply by two until $\Delta t = 4096\Delta t_{CFL}$ (that corresponds to 2 time steps). We note a clear advantage in the number of iterations for the Newton method with local under-relaxation when Δt increases. From the two examples reported, we can conclude that the trust-region reflective and dogleg schemes are more competitive for sizes of time step chosen as tens of Δt_{CFL}, while the Newton method with local under-relaxation is the best choice for sizes of time step selected as hundreds or thousands of Δt_{CFL}. The Newton method with global under-relaxation, as expected, requires more iterations to converge than the Newton method with local under-relaxation. However, it performs better than the trust-region reflective and dogleg algorithms for large sizes of time step.

Figure 59 shows a comparison of the saturation profiles at time $T_{\mathbf{PVI}} = 0.11$ approximated by the Newton method with local under-relaxation. We exhibit saturation maps provided by different sizes of time step. Note that all solutions are consistent with the physics of the problem. Therefore, the choice of the size of the time step is based only on accuracy requirements.

Figure 58 – Total accumulated of iterations until time $T_{\mathbf{PVI}} = 0.11$ for different choices of size of time step. The Newton method with local under-relaxation requires fewer iterations than the other procedures for large sizes of time step.

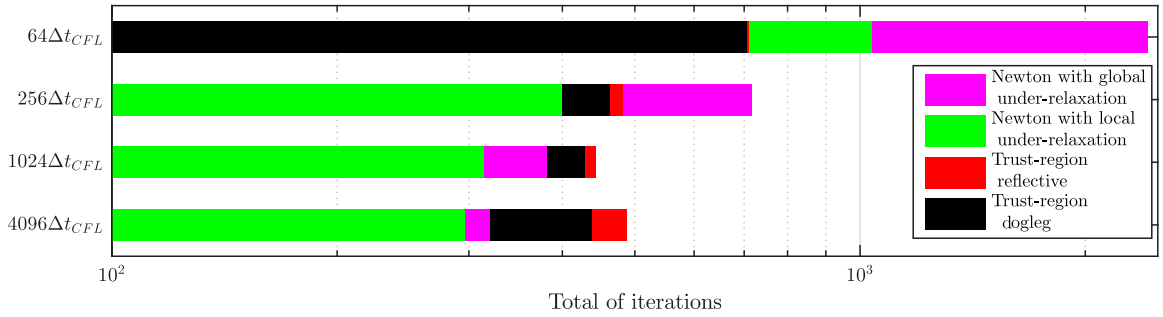

Source: Research data.

To close this discussion, we perform a convergence study by setting the solution computed with $\Delta t = \Delta t_{CFL}$ as reference. We compute the errors of each method considering its own reference solution. Figure 60 shows the convergence of the methods, where we note the same behavior (linear slope) for all of them. We remark that linear is the expected slope, once we compute the time discretization by the first order implicit Euler method.

6.2.2 A multiscale solution

In this section, we consider the MRCM for approximating nonlinear two-phase flows. Since high-contrast channelized formations are challenging for multiscale methods, we repeat the previous experiment on layer number 36 of the SPE10 field. We apply the pressure physics-based interface space presented in Chapter 4 to better represent the solution at the high-permeable structure. We investigate the accuracy of the MRCM combined with the SI approach by using the Newton method with local under-relaxation, that we show to be adequate for large values of size of time step. This choice is based only on terms of the number of iterations since all the algorithms considered provided similar accuracy.

Concerning the MRCM, the flux interface space is linear as well as the pressure space at the interfaces that do not cross the high-permeable channel. We set $\alpha = 10^{-2}$ at the interfaces that cross the channel and $\alpha = 10^2$ at the remaining interfaces by using the adaptive version of the MRCM (ROCHA *et al.*, 2020b). The downscaling procedure used to compute a conservative solution for the MRCM approximation is the stitch method (GUIRALDELLO *et al.*, 2020).

Figure 61 shows the total accumulated of iterations until time $T_{PVI} = 0.11$ for the different choices of size of time step. We present the number of iterations provided by the SI scheme when combined with the MRCM for a domain decomposition of 11×3 subdomains with 20×20 cells into each one. We include the number of iterations of the SI scheme combined with the fine mesh approximation (in space) as presented in the previous subsection. We note that the number of iterations required by the MRCM is comparable to the demanded by the fine mesh

Figure 59 – Saturation profiles at time $T_{\mathbf{PVI}} = 0.11$ approximated by the Newton method with local under-relaxation considering different sizes of time step. The choice of the size of the time step is based only on accuracy requirements.

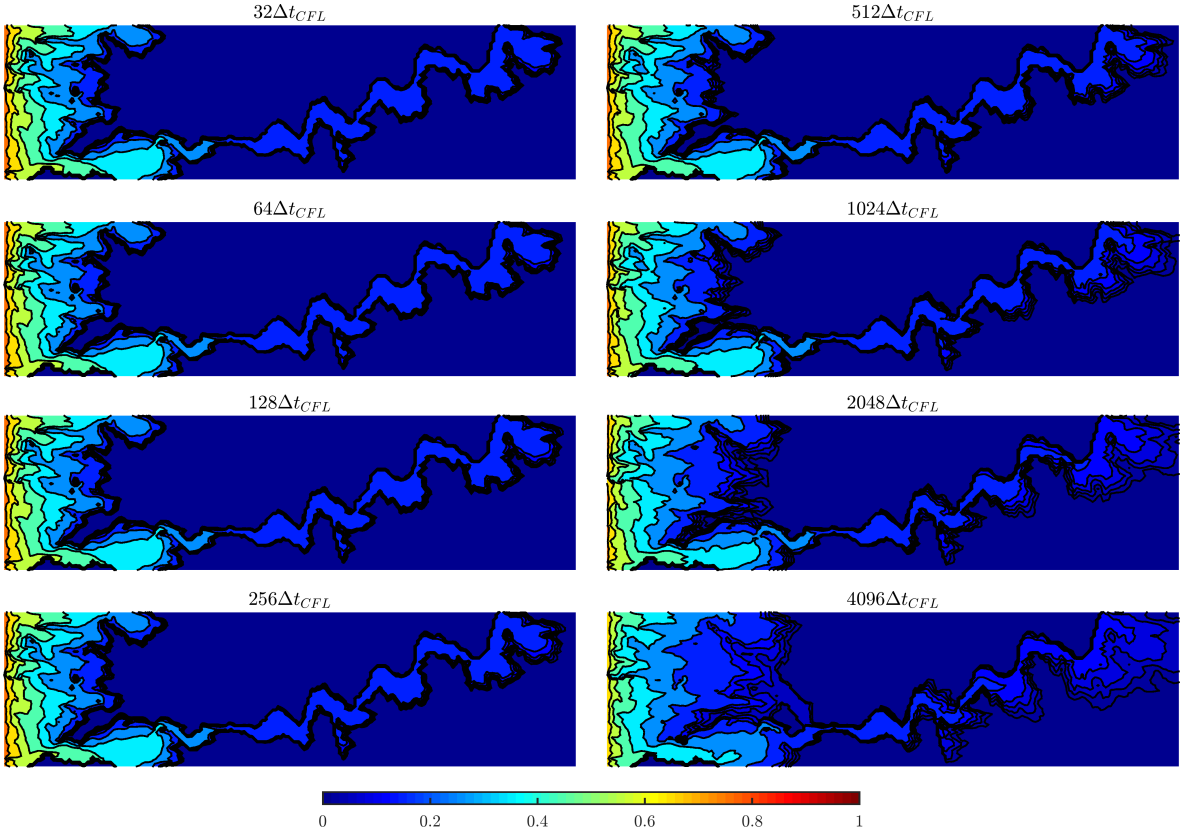

Source: Research data.

procedure. Therefore, the sequential implicit solver does not suffer from an increase in the number of iterations when combined with the MRCM.

A comparison of the saturation profiles at time $T_{\mathbf{PVI}} = 0.11$ approximated by the MRCM and fine mesh procedures is displayed in Figure 62. We present saturation maps provided by different sizes of time step. For each choice of Δt we note that the MRCM and fine mesh approximations are closely related. Note that there are no inaccuracies originated strictly by the multiscale approximation.

The convergence study is reported in Figure 63, where we consider as reference the approximation computed with $\Delta t = 32\Delta t_{CFL}$. The same behavior (linear slope) is attained when the error of each procedure considers its own reference solution. We add the error of the MRCM considering as reference the fine mesh solution with $\Delta t = 32\Delta t_{CFL}$. In this curve, the multiscale imprecisions are relevant when $\Delta t < 512\Delta t_{CFL}$, while the error of the transport procedure is dominant for larger choices of size of time step. If we compute the error of the MRCM approximation considering as reference the respective fine mesh solution with the same time discretization we obtain an error of the order 3×10^{-2} for all Δt, that is consistent with the dominant multiscale error observed on the convergence curve.

Figure 60 – Convergence study by setting the solution computed with $\Delta t = \Delta t_{CFL}$ as reference. Each method considers its own reference solution. We note the same behavior (linear slope) for all methods.

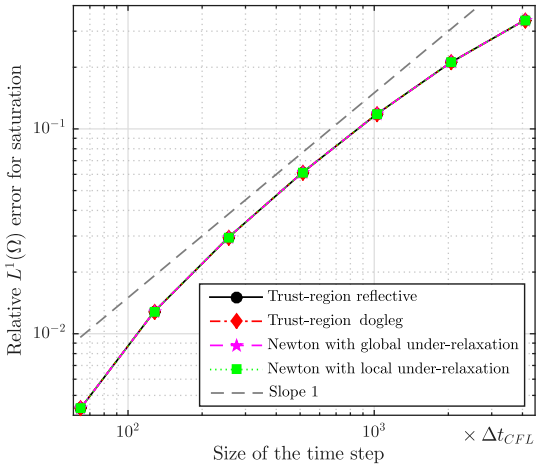

Source: Research data.

Figure 61 – Total accumulated of iterations until time $T_{\mathbf{PVI}} = 0.11$ for the SI scheme combined with the MRCM and fine mesh approximations. The number of iterations required by the MRCM is comparable to the demanded by the fine mesh procedure.

Source: Research data.

To close this section, we report in Figure 64 the errors of the previous experiment as a function of time. We show relative errors of flux and saturation for the MRCM (solid lines) and fine grid (dashed lines) approximations considering different choices of size of time step. The reference is the fine grid solution with $\Delta t = 32\Delta t_{CFL}$. The flux error is computed as usual: at each time we divide the L^2 norm of the difference by the L^2 norm of the reference at the same time. The saturation error (for this plot) divides the L^1 norm of the differences by the maximum absolute of the reference on time, avoiding divisions by very small values at the beginning of the simulation. We note that the error curves do not vary significantly over time. This result shows that the observations from the convergence study for saturation (at time $T_{\mathbf{PVI}} = 0.11$) are maintained throughout the simulation. The flux errors of the MRCM are essentially the same for all Δt, whereas the fine grid errors decrease with the size of the time step.

Figure 62 – Saturation profiles at time $T_{\mathbf{PVI}} = 0.11$ approximated by the MRCM and fine mesh procedures considering different sizes of time step. The approximations provided by the MRCM and fine mesh approaches are closely related for each size of time step.

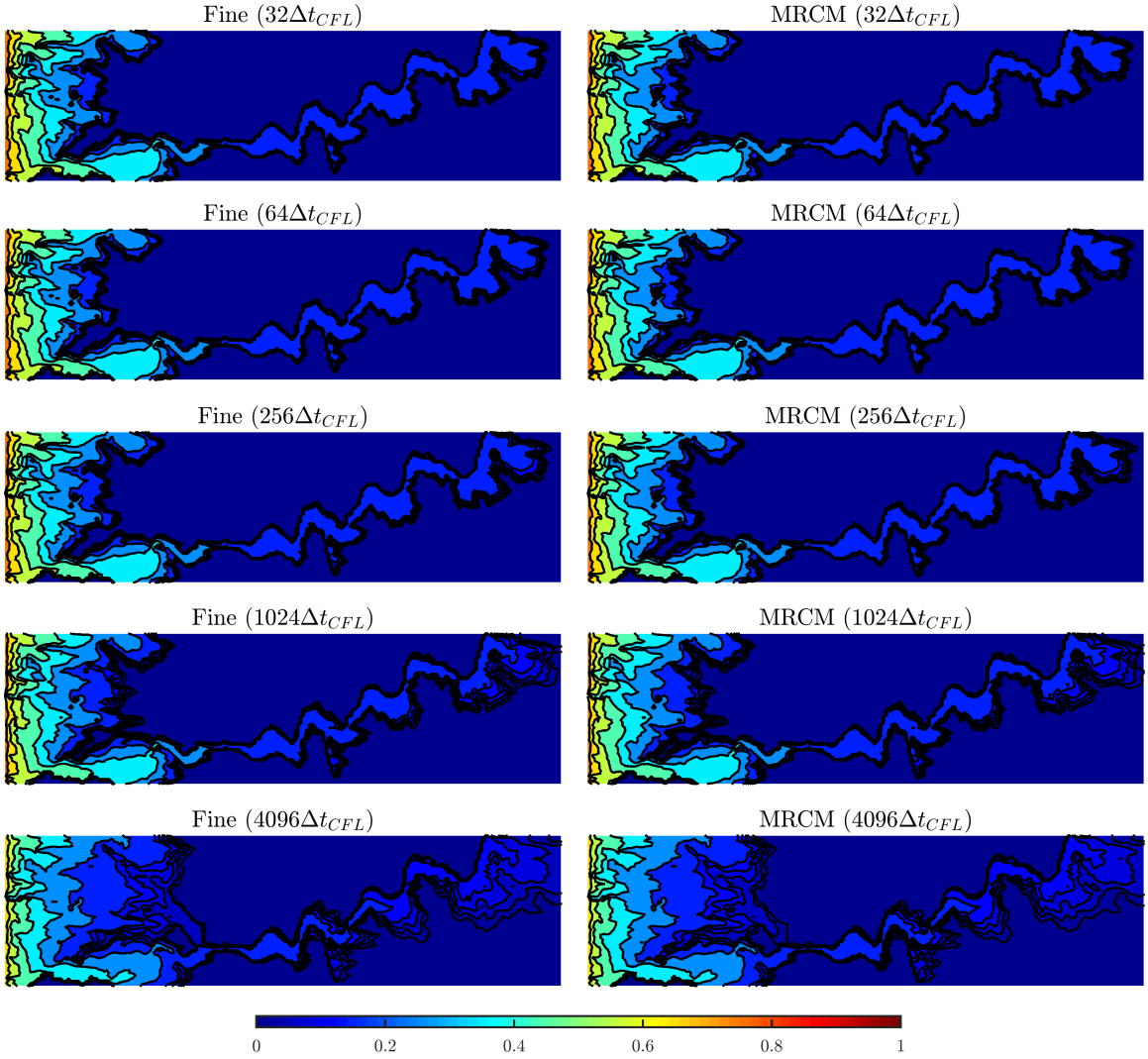

Source: Research data.

6.3 Discussion

We investigate the solution of two-phase, oil-water flows in heterogeneous porous media. Firstly, we tested the SI solver with different trust-region algorithms. We show that the trust-region reflective and dogleg schemes are appropriated when the size of the time step is chosen as tens of the Δt_{CFL}, while the Newton methods with local and global under-relaxation are adequate to handle sizes of time step chosen as hundreds or thousands of the Δt_{CFL}.

Then, we combined the MRCM with the SI solver considering the Newton method with local under-relaxation. The numerical experiments provide that the results produced by the MRCM are accurate and robust for the simulation of two-phase flows when combined with the implicit hyperbolic solver. This is a promising result in terms of computational efficiency since the MRCM can take advantage of state-of-the-art parallel machines and produce two-phase flow

Figure 63 – Convergence study by setting the solution computed with $\Delta t = 32\Delta t_{CFL}$ as reference. We compare the MRCM errors considering its own reference and the fine grid reference solution. The multiscale imprecisions are relevant for choices of $\Delta t < 512\Delta t_{CFL}$, while the error of the transport procedure is dominant for larger choices of size of time step.

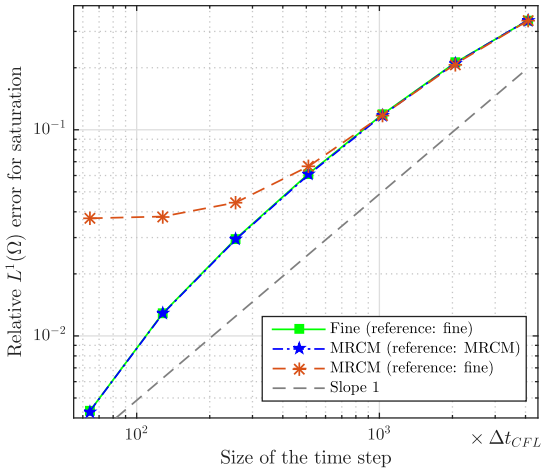

Source: Research data.

Figure 64 – Relative errors of flux (left) and saturation (right) for the MRCM (solid lines) and fine grid (dashed lines) approximations considering different choices of size of time step. The reference solution is the fine grid approximation with $\Delta t = 32\Delta t_{CFL}$. We note that the error curves do not vary significantly over time.

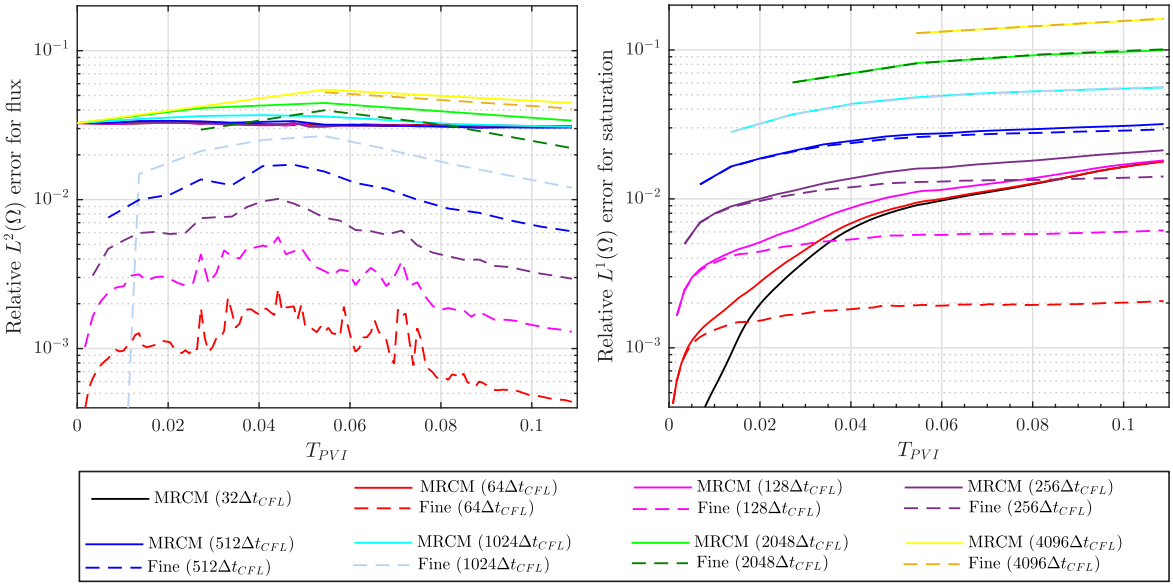

Source: Research data.

simulations with a reduced computational cost.

The SI algorithm produces satisfactory results in the context of two-phase flows without gravity and capillary effects. However, the semi-implicit treatment of the velocity can generate material balance errors in more complex models (AZIZ; SETTARI, 1979). The Sequential Fully Implicit (SFI) scheme, developed in the Multiscale Finite Volume Method framework (JENNY;

LEE; TCHELEPI, 2006) is an option to deal with this issue. See also (JIANG; TCHELEPI, 2019) for developments on nonlinear acceleration techniques. The results provided by the SFI and the SI methods are closely related in the context of this chapter, however, the SFI algorithm should be considered to further apply the MRCM to more complex models.

CHAPTER

7

CONCLUSIONS AND FUTURE WORK

This thesis has addressed a careful assessment of the MRCM for the numerical solution of two-phase, oil-water flows in heterogeneous, high-contrast porous media. Moreover, we have investigated different techniques to enhance the approximation of two-phase flows in terms of accuracy and computational efficiency.

We have shown in Chapter 3 that the improved accuracy of the MRCM for single-phase flow problems in the approximation of velocity and pressure fields is also observed for the saturation field. Thus, the original findings for the MRCM are fully preserved in the approximation of two-phase flows. We have introduced an adaptivity strategy for setting the Robin algorithmic parameter of the MRCM to capture the permeability variations. Our numerical simulations of two-phase flows present an unprecedented accuracy, in that we produce better solutions for problems with high-contrast permeability coefficients when compared to solutions obtained with some standard multiscale mixed methods.

In Chapter 4, the adaptive MRCM has been combined with new interface spaces based on physics for better capturing the high-contrast effects of channelized structures. We have introduced two physics-based interface spaces (one for pressure and other for flux) to deal with permeability fields in the simultaneous presence of high permeability channels and barriers. The features of the proposed approach have been investigated through several numerical simulations of single-phase and two-phase flows, in different heterogeneous porous media. We show that the considered multiscale mixed methods combined with the new interface spaces are significantly more accurate than when combined with polynomial spaces.

The MPM-2P has been proposed in Chapter 5 to speed-up the numerical simulation of two-phase flows in porous media. We formulate a modified operator splitting method, where we replace full updates of local solutions by reusing basis functions computed by the MRCM at an earlier time of the simulation. Our numerical experiments demonstrate a significant reduction of the computational cost in the approximation of challenging two-phase flow problems, while the

accuracy is controlled by a tolerance criterion.

Finally, in Chapter 6, the MRCM has been tested in a sequential implicit scheme for two-phase flow problems. The new approach allows for the use of arbitrarily large time steps when compared to explicit time integration methods, improving the efficiency of the simulation. We show that the MRCM produces accurate solutions when combined with different hyperbolic solvers, including sequential implicit techniques.

The MRCM for two-phase flows as presented here can take advantage of state-of-the-art supercomputers, its computational cost is comparable to existing procedures, and it presents accurate and robust approximations for realistic problems. The contributions of this thesis are summarized in section 7.1, followed by section 7.2, with the plans for future work.

7.1 Contributions

The contributions generated during the doctoral period are listed below.

7.1.1 Main contributions

- *Two-phase flows in porous media with the MRCM: Chapter 2 and Chapter 3.*
  - The first study of the MRCM for two-phase flows;
  - A throughout comparison of multiscale mixed methods for two-phase flows in porous media;
  - New adaptivity strategy for an important algorithmic parameter of the MRCM;
  - Evidence of improved accuracy for two-phase flows in realistic permeability fields.

  These chapters are based on the publication “Multiscale mixed methods for two-phase flows in high-contrast porous media" produced in collaboration with Fabricio S. Sousa, Roberto F. Ausas, Gustavo C. Buscaglia, and Felipe Pereira (ROCHA *et al.*, 2020b).

- *Interface spaces based on physics for multiscale mixed finite element methods: Chapter 4.*
  - New interface spaces to deal with permeability fields in the simultaneous presence of high permeability channels and barriers;
  - Adaptivity of the MRCM is used to set the appropriate pressure and flux spaces at each interface of the decomposition of the domain;
  - Multiscale mixed methods combined with the new interface spaces are significantly more accurate than when combined with polynomial spaces;
  - Evidence of improved accuracy is provided for both single and two-phase flows in high-contrast permeability fields.

This chapter is based on the manuscript “Interface spaces based on physics for multiscale mixed methods applied to flows in channelized porous media" produced in collaboration with Fabricio S. Sousa, Roberto F. Ausas, Felipe Pereira, and Gustavo C. Buscaglia and submitted to a renowned international journal (ROCHA *et al.*, 2020a).

- *Approximation of two-phase flows by the Multiscale Perturbation Method: Chapter 5.*
  - MPM-2P introduced to speed-up the numerical solution of two-phase flow problems;
  - Modified operator splitting method to reduce the computational cost of the simulation of the two-phase flows;
  - Replaces full updates of local solutions by reusing basis functions computed by the MRCM at an earlier time of the simulation;
  - Accuracy controlled by a tolerance criterion;
  - Evidence of improved efficiency for challenging two-phase flow problems.

  This chapter is based on the manuscript “The Multiscale Perturbation Method for Two-Phase Flows in Porous Media" in preparation with the collaboration of Het Mankad, Fabricio S. Sousa, and Felipe Pereira.

- *The MRCM in a sequential implicit scheme for two-phase flow problems: Chapter 6.*
  - A comparison of sequential implicit solvers for two-phase flows in porous media;
  - First study combining the MRCM with a sequential implicit scheme;
  - Evidence of improved accuracy and efficiency for flows in high-contrast, heterogeneous porous media.

  This chapter is based on the manuscript “A sequential implicit solver for two-phase subsurface flows using the Multiscale Robin Coupled Method" in preparation with the collaboration of Fabricio S. Sousa, Roberto F. Ausas, Gustavo C. Buscaglia, and Felipe Pereira.

7.1.2 Other contributions

- “Precisão de métodos de volumes finitos para a solução da equação de Buckley-Leverett" (ROCHA *et al.*, 2018);
- “A trajectory planning model for the manipulation of particles in microfluidics" (MEACCI *et al.*, 2018);
- “Planejamento de trajetória para a manipulação de partículas em microfluídica" (MEACCI *et al.*, 2017).

7.2 Future work

The MRCM for two-phase flows has been presented (ROCHA *et al.*, 2020b; ROCHA *et al.*, 2020a). However, several improvements are still under investigation. The main directions to extend this thesis are summarized as follows.

- *Interface spaces based on physics for 3D reservoir flow problems.*

  The development of interface spaces based on physics for 3D reservoir flow problems is a topic that is currently being considered. We intend to include these spaces in applications of the MRCM for more complex flow models.

- *3D high-performance computing study.*

  The MRCM for two-phase flows has been investigated only in the two-dimensional case (ROCHA *et al.*, 2020b; ROCHA *et al.*, 2020a). Our research group has currently developments on the 3D extension for the MRCM considering high-performance computing. The thesis' author intends to collaborate at this study aiming at solving large size reservoirs.

- *Adaptive time stepping for the coupling of flow and transport.*

  We intend to investigate time-adaptivity strategies for the coupling of flow and transport in porous media. Our research group has recently developed an adaptive time stepping algorithm for an Implicit Pressure Explicit Saturation (IMPES) scheme (PAZ *et al.*, 2020). The thesis' author intends to collaborate at this research aiming at combining the adaptive time stepping strategy with the sequential implicit solver.

BIBLIOGRAPHY

AARNES, J. On the use of a mixed multiscale finite element method for greater flexibility and increased speed or improved accuracy in reservoir simulation. **Multiscale Modeling & Simulation**, SIAM, v. 2, n. 3, p. 421–439, 2006. Citation on page 34.

AARNES, J.; EFENDIEV, Y.; HOU, T.; JIANG, L. Mixed multiscale finite element methods on adaptive unstructured grids using limited global information. **Multiscale Methods: Bridging the Scales in Science and Engineering**, Oxford University Press on Demand, v. 1, 2010. Citations on pages 35 and 36.

AARNES, J.; HOU, T. Y. Multiscale domain decomposition methods for elliptic problems with high aspect ratios. **Acta Mathematicae Applicatae Sinica**, Springer, v. 18, n. 1, p. 63–76, 2002. Citation on page 34.

AARNES, J. E. On the use of a mixed multiscale finite element method for greater flexibility and increased speed or improved accuracy in reservoir simulation. **Multiscale Modeling & Simulation**, SIAM, v. 2, n. 3, p. 421–439, 2004. Citations on pages 35 and 36.

AARNES, J. E.; EFENDIEV, Y. An adaptive multiscale method for simulation of fluid flow in heterogeneous porous media. **Multiscale Modeling & Simulation**, SIAM, v. 5, n. 3, p. 918–939, 2006. Citations on pages 35 and 36.

____. Mixed multiscale finite element methods for stochastic porous media flows. **SIAM Journal on Scientific Computing**, SIAM, v. 30, n. 5, p. 2319–2339, 2008. Citation on page 40.

____. A multiscale method for modeling transport in porous media on unstructured corner-point grids. **Journal of Algorithms & Computational Technology**, SAGE Publications Sage UK: London, England, v. 2, n. 2, p. 299–318, 2008. Citations on pages 35 and 36.

AARNES, J. E.; EFENDIEV, Y.; JIANG, L. Mixed multiscale finite element methods using limited global information. **Multiscale Modeling & Simulation**, SIAM, v. 7, n. 2, p. 655–676, 2008. Citations on pages 35 and 36.

AARNES, J. E.; KIPPE, V.; LIE, K.-A. Mixed multiscale finite elements and streamline methods for reservoir simulation of large geomodels. **Advances in Water Resources**, Elsevier, v. 28, n. 3, p. 257–271, 2005. Citations on pages 35 and 36.

AARNES, J. E.; KROGSTAD, S.; LIE, K.-A. A hierarchical multiscale method for two-phase flow based upon mixed finite elements and nonuniform coarse grids. **Multiscale Modeling & Simulation**, SIAM, v. 5, n. 2, p. 337–363, 2006. Citations on pages 34, 35, 36, 42, and 77.

____. Multiscale mixed/mimetic methods on corner-point grids. **Computational Geosciences**, Springer, v. 12, n. 3, p. 297–315, 2008. Citations on pages 35 and 36.

ABDULLAH, M. A.; PANDA, A.; GUPTA, S.; JOSHI, S.; SINGH, A.; RAO, N. Multi-scale method for modeling and simulation of two phase flow in reservoir using MRST. **Petroleum & Coal**, v. 61, n. 3, 2019. Citation on page 36.

ABREU, E.; PEREIRA, F.; RIBEIRO, S. Central schemes for porous media flows. **Computational & Applied Mathematics**, SciELO Brasil, v. 28, n. 1, p. 87–110, 2009. Citation on page 52.

AHMED, E.; FUMAGALLI, A.; BUDIŠA, A. A multiscale flux basis for mortar mixed discretizations of reduced Darcy–Forchheimer fracture models. **Computer Methods in Applied Mechanics and Engineering**, Elsevier, v. 354, p. 16–36, 2019. Citation on page 41.

AKBARI, H.; ENGSIG-KARUP, A. P.; GINTING, V.; PEREIRA, F. A multiscale direct solver for the approximation of flows in high contrast porous media. **Journal of Computational and Applied Mathematics**, Elsevier, v. 359, p. 88–101, 2019. Citations on pages 38 and 39.

ALPAK, F. O.; PAL, M.; LIE, K.-A. A multiscale adaptive local-global method for modeling flow in stratigraphically complex reservoirs. **SPE Journal**, Society of Petroleum Engineers, v. 17, n. 04, p. 1–056, 2012. Citations on pages 35 and 36.

ALSADIG, A.; MANKAD, H.; PEREIRA, F.; SOUSA, F. S. The multiscale perturbation method for second order elliptic equations. **Applied Mathematics and Computation**, Elsevier, p. 125023, 2020. Citations on pages 38, 39, 42, 101, 102, 104, 105, and 109.

AMBARTSUMYAN, I.; KHATTATOV, E.; WANG, C.; YOTOV, I. Stochastic multiscale flux basis for Stokes-Darcy flows. **Journal of Computational Physics**, Elsevier, p. 109011, 2019. Citation on page 40.

ARAYA, R.; HARDER, C.; PAREDES, D.; VALENTIN, F. Multiscale hybrid-mixed method. **Journal on Numerical Analysis**, SIAM, v. 51, n. 6, p. 3505–3531, 2013. Citations on pages 37, 39, 41, and 48.

ARAYA, R.; HARDER, C.; POZA, A. H.; VALENTIN, F. Multiscale hybrid-mixed method for the Stokes and Brinkman equations – the method. **Computer Methods in Applied Mechanics and Engineering**, Elsevier, v. 324, p. 29–53, 2017. Citations on pages 38 and 39.

ARBOGAST, T. Homogenization-based mixed multiscale finite elements for problems with anisotropy. **Multiscale Modeling & Simulation**, SIAM, v. 9, n. 2, p. 624–653, 2011. Citations on pages 35, 36, and 37.

____. Mixed multiscale methods for heterogeneous elliptic problems. In: **Numerical Analysis of Multiscale Problems**. Berlin, Heidelberg: Springer, 2012. p. 243–283. Citation on page 41.

ARBOGAST, T.; BOYD, K. J. Subgrid upscaling and mixed multiscale finite elements. **SIAM Journal on Numerical Analysis**, SIAM, v. 44, n. 3, p. 1150–1171, 2006. Citations on pages 35 and 36.

ARBOGAST, T.; PENCHEVA, G.; WHEELER, M.; YOTOV, I. A multiscale mortar mixed finite element method. **Multiscale Modeling & Simulation**, SIAM, v. 6, n. 1, p. 319–346, 2007. Citations on pages 34, 41, and 48.

ARBOGAST, T.; PENCHEVA, G.; WHEELER, M. F.; YOTOV, I. A multiscale mortar mixed finite element method. **Multiscale Modeling & Simulation**, SIAM, v. 6, n. 1, p. 319–346, 2007. Citations on pages 36 and 38.

ARBOGAST, T.; TAO, Z.; XIAO, H. Multiscale mortar mixed methods for heterogeneous elliptic problems. **Contemporari Mathematics**, v. 586, p. 9–21, 2013. Citations on pages 37 and 38.

ARBOGAST, T.; XIAO, H. A multiscale mortar mixed space based on homogenization for heterogeneous elliptic problems. **SIAM Journal on Numerical Analysis**, SIAM, v. 51, n. 1, p. 377–399, 2013. Citations on pages 37 and 38.

ARSHAD, M.; PARK, E.-J. Multiscale mortar expanded mixed discretization of nonlinear elliptic problems. **Applied Mathematics and Computation**, Elsevier, v. 371, p. 124932, 2020. Citations on pages 37 and 38.

ARSHAD, M.; PARK, E.-J.; SHIN, D.-W. Analysis of multiscale mortar mixed approximation of nonlinear elliptic equations. **Computers & Mathematics with Applications**, Elsevier, v. 75, n. 2, p. 401–418, 2018. Citations on pages 37 and 38.

AZIZ, K.; SETTARI, A. **Petroleum reservoir simulation**. London: Applied Science Publishers LTD, 1979. Citations on pages 33, 127, and 147.

BAOMIN, Z.; JINGJIANG, L. Classification and characteristics of karst reservoirs in China and related theories. **Petroleum Exploration and Development**, Elsevier, v. 36, n. 1, p. 12–29, 2009. Citations on pages 42 and 78.

BARRENECHEA, G. R.; JAILLET, F.; PAREDES, D.; VALENTIN, F. The multiscale hybrid mixed method in general polygonal meshes. **Numerische Mathematik**, Springer, p. 1–41, 2020. Citations on pages 38 and 39.

BERKOWITZ, B. Characterizing flow and transport in fractured geological media: A review. **Advances in Water Resources**, Elsevier, v. 25, n. 8-12, p. 861–884, 2002. Citation on page 78.

BOSMA, S.; HAJIBEYGI, H.; TENE, M.; TCHELEPI, H. A. Multiscale finite volume method for discrete fracture modeling on unstructured grids (MS-DFM). **Journal of Computational Physics**, Elsevier, v. 351, p. 145–164, 2017. Citation on page 78.

BRANCH, M. A.; COLEMAN, T. F.; LI, Y. A subspace, interior, and conjugate gradient method for large-scale bound-constrained minimization problems. **SIAM Journal on Scientific Computing**, SIAM, v. 21, n. 1, p. 1–23, 1999. Citation on page 120.

BYRD, R. H.; SCHNABEL, R. B.; SHULTZ, G. A. Approximate solution of the trust region problem by minimization over two-dimensional subspaces. **Mathematical programming**, Springer, v. 40, n. 1-3, p. 247–263, 1988. Citation on page 120.

CALO, V. M.; CHUNG, E. T.; EFENDIEV, Y.; LEUNG, W. T. Multiscale stabilization for convection-dominated diffusion in heterogeneous media. **Computer Methods in Applied Mechanics and Engineering**, Elsevier, v. 304, p. 359–377, 2016. Citations on pages 40 and 41.

CHAI, Z.; YAN, B.; KILLOUGH, J.; WANG, Y. An efficient method for fractured shale reservoir history matching: The embedded discrete fracture multi-continuum approach. **Journal of Petroleum Science and Engineering**, Elsevier, v. 160, p. 170–181, 2018. Citation on page 78.

CHAN, H. Y.; CHUNG, E.; EFENDIEV, Y. Adaptive mixed GMsFEM for flows in heterogeneous media. **Numerical Mathematics: Theory, Methods and Applications**, Cambridge University Press, v. 9, n. 4, p. 497–527, 2016. Citations on pages 40 and 41.

CHEN, F.; CHUNG, E.; JIANG, L. Least-squares mixed generalized multiscale finite element method. **Computer Methods in Applied Mechanics and Engineering**, Elsevier, v. 311, p. 764–787, 2016. Citations on pages 40 and 41.

CHEN, J.; CHUNG, E. T.; HE, Z.; SUN, S. Generalized multiscale approximation of mixed finite elements with velocity elimination for subsurface flow. **Journal of Computational Physics**, Elsevier, p. 109133, 2019. Citations on pages 40 and 41.

CHEN, Z.; HOU, T. A mixed multiscale finite element method for elliptic problems with oscillating coefficients. **Mathematics of Computation**, v. 72, n. 242, p. 541–576, 2003. Citations on pages 34, 35, and 36.

CHEN, Z.; HUAN, G.; MA, Y. **Computational methods for multiphase flows in porous media**. Philadelphia, PA, EUA: Society for Industrial and Applied Mathematics, 2006. Citations on pages 33 and 56.

CHRISTIE, M. A.; BLUNT, M. J. Tenth SPE comparative solution project: A comparison of upscaling techniques. In: SOCIETY OF PETROLEUM ENGINEERS. **SPE Reservoir Simulation Symposium**. Houston, TX, EUA, 2001. Citation on page 57.

CHUNG, E.; EFENDIEV, Y.; HOU, T. Y. Adaptive multiscale model reduction with generalized multiscale finite element methods. **Journal of Computational Physics**, Elsevier, v. 320, p. 69–95, 2016. Citations on pages 40 and 41.

CHUNG, E.; EFENDIEV, Y.; LEUNG, W. T. Constraint energy minimizing generalized multiscale finite element method in the mixed formulation. **Computational Geosciences**, Springer, v. 22, n. 3, p. 677–693, 2018. Citations on pages 40 and 41.

____. Generalized multiscale finite element methods with energy minimizing oversampling. **International Journal for Numerical Methods in Engineering**, Wiley Online Library, v. 117, n. 3, p. 316–343, 2019. Citations on pages 40 and 41.

CHUNG, E.; POLLOCK, S.; PUN, S.-M. Goal-oriented adaptivity of mixed GMsFEM for flows in heterogeneous media. **Computer Methods in Applied Mechanics and Engineering**, Elsevier, v. 323, p. 151–173, 2017. Citations on pages 40 and 41.

CHUNG, E. T.; EFENDIEV, Y.; LEE, C. S. Mixed generalized multiscale finite element methods and applications. **Multiscale Modeling & Simulation**, SIAM, v. 13, n. 1, p. 338–366, 2015. Citations on pages 34, 40, 41, and 94.

CHUNG, E. T.; EFENDIEV, Y.; LEUNG, T.; VASILYEVA, M. Coupling of multiscale and multi-continuum approaches. **GEM-International Journal on Geomathematics**, Springer, v. 8, n. 1, p. 9–41, 2017. Citation on page 78.

CHUNG, E. T.; EFENDIEV, Y.; LEUNG, W. T. An online generalized multiscale discontinuous Galerkin method (GMsDGM) for flows in heterogeneous media. **Communications in Computational Physics**, Cambridge University Press, v. 21, n. 2, p. 401–422, 2017. Citations on pages 77 and 94.

CHUNG, E. T.; EFENDIEV, Y.; LI, G. An adaptive GMsFEM for high-contrast flow problems. **Journal of Computational Physics**, Elsevier, v. 273, p. 54–76, 2014. Citations on pages 42, 77, and 94.

CHUNG, E. T.; FU, S.; YANG, Y. An enriched multiscale mortar space for high contrast flow problems. **arXiv preprint arXiv:1609.02610**, 2016. Citations on pages 40, 41, 42, 77, and 94.

CHUNG, E. T.; LEUNG, W. T.; VASILYEVA, M. Mixed GMsFEM for second order elliptic problem in perforated domains. **Journal of Computational and Applied Mathematics**, Elsevier, v. 304, p. 84–99, 2016. Citations on pages 40 and 41.

CHUNG, E. T.; PUN, S.-M. Online adaptive basis enrichment for mixed CEM-GMsFEM. **Multiscale Modeling & Simulation**, SIAM, v. 17, n. 4, p. 1103–1122, 2019. Citations on pages 40, 41, 77, and 94.

COATS, K. H. A note on IMPES and some IMPES-based simulation models. **SPE Journal**, Society of Petroleum Engineers, v. 5, p. 245–251, 2000. Citation on page 46.

CONN, A. R.; GOULD, N. I.; TOINT, P. L. **Trust region methods**. Philadelphia, PA, USA: Society for Industrial and Applied Mathematics, 2000. Citation on page 120.

CORTINOVIS, D.; JENNY, P. Iterative Galerkin-enriched multiscale finite-volume method. **Journal of Computational Physics**, Elsevier, v. 277, p. 248–267, 2014. Citation on page 77.

_____. Zonal multiscale finite-volume framework. **Journal of Computational Physics**, Elsevier, v. 337, p. 84–97, 2017. Citations on pages 34, 42, 56, 66, and 77.

DAMIÁN, S. M.; NIGRO, N. M.; BUSCAGLIA, G. C. A central scheme for advecting scalars by velocity fields obtained from finite volume multiphase incompressible solvers. **Applied Mathematical Modelling**, Elsevier, v. 40, n. 15, p. 6934–6955, 2016. Citation on page 52.

DEVLOO, P.; TENG, W.; ZHANG, C.-S. Multiscale hybrid-mixed finite element method for flow simulation in fractured porous media. **Computer Modeling in Engineering & Sciences**, Tech Science Press, v. 119, n. 1, p. 145–163, 2019. Citations on pages 38, 39, and 78.

DOUGLAS, J.; EWING, R.; WHEELER, M. A time-discretization procedure for a mixed finite element approximation of miscible displacement in porous media. **RAIRO. Analyse Numérique**, Dunod-Gauthier-Villars, v. 17, n. 3, p. 249–265, 1983. Citations on pages 42 and 46.

DOUGLAS, J.; FURTADO, F.; PEREIRA, F. On the numerical simulation of waterflooding of heterogeneous petroleum reservoirs. **Computational Geosciences**, Springer, v. 1, n. 2, p. 155–190, 1997. Citations on pages 34, 42, 46, and 47.

DOUGLAS, J.; PAES-LEME, P.; ROBERTS, J.; WANG, J. A parallel iterative procedure applicable to the approximate solution of second order partial differential equations by mixed finite element methods. **Numerische Mathematik**, v. 65, n. 1, p. 95–108, 1993. Citations on pages 38, 41, and 47.

DOUGLAS, J.; PEREIRA, F.; YEH, L.-M. A locally conservative Eulerian–Lagrangian numerical method and its application to nonlinear transport in porous media. **Computational Geosciences**, Springer, v. 4, n. 1, p. 1–40, 2000. Citations on pages 42 and 46.

DURÁN, O.; DEVLOO, P.; GOMES, S.; VILLEGAS, J. A multiscale mixed method for a two-phase reservoir simulator. **Computer Methods in Applied Mechanics and Engineering**, 2020. Citations on pages 34, 38, and 39.

DURÁN, O.; DEVLOO, P. R.; GOMES, S. M.; VALENTIN, F. A multiscale hybrid method for Darcy's problems using mixed finite element local solvers. **Computer Methods in Applied Mechanics and Engineering**, Elsevier, v. 354, p. 213–244, 2019. Citations on pages 38 and 39.

EDWARDS, M. G. A higher-order Godunov scheme coupled with dynamic local grid refinement for flow in a porous medium. **Computer Methods in Applied Mechanics and Engineering**, Elsevier, v. 131, n. 3-4, p. 287–308, 1996. Citation on page 52.

EFENDIEV, Y.; GALVIS, J.; HOU, T. Y. Generalized multiscale finite element methods (GMsFEM). **Journal of Computational Physics**, Elsevier, v. 251, p. 116–135, 2013. Citations on pages 34, 40, 77, and 94.

EFENDIEV, Y.; GINTING, V.; HOU, T.; EWING, R. Accurate multiscale finite element methods for two-phase flow simulations. **Journal of Computational Physics**, Elsevier, v. 220, n. 1, p. 155–174, 2006. Citation on page 34.

EFENDIEV, Y.; ILIEV, O.; KRONSBEIN, C. Multilevel Monte Carlo methods using ensemble level mixed MsFEM for two-phase flow and transport simulations. **Computational Geosciences**, Springer, v. 17, n. 5, p. 833–850, 2013. Citations on pages 35 and 36.

EFENDIEV, Y.; LEE, S.; LI, G.; YAO, J.; ZHANG, N. Hierarchical multiscale modeling for flows in fractured media using generalized multiscale finite element method. **GEM-International Journal on Geomathematics**, Springer, v. 6, n. 2, p. 141–162, 2015. Citation on page 78.

EWING, R. E. **The mathematics of reservoir simulation**. Philadelphia, PA, USA: Society for Industrial and Applied Mathematics, 1983. Citations on pages 33, 34, 147, 149, and 150.

FERRAZ, P. C. **A novel recursive formulation of multiscale mixed methods and relaxation modeling of flow in porous media**. Phd Thesis (PhD Thesis) — University of Campinas, Campinas, SP, Bazil, 2019. Citations on pages 101 and 107.

FLEMISCH, B.; BERRE, I.; BOON, W.; FUMAGALLI, A.; SCHWENCK, N.; SCOTTI, A.; STEFANSSON, I.; TATOMIR, A. Benchmarks for single-phase flow in fractured porous media. **Advances in Water Resources**, Elsevier, v. 111, p. 239–258, 2018. Citation on page 78.

FORMAGGIA, L.; FUMAGALLI, A.; SCOTTI, A.; RUFFO, P. A reduced model for Darcy's problem in networks of fractures. **ESAIM: Mathematical Modelling and Numerical Analysis**, EDP Sciences, v. 48, n. 4, p. 1089–1116, 2014. Citation on page 78.

FRANCISCO, A.; GINTING, V.; PEREIRA, F.; RIGELO, J. Design and implementation of a multiscale mixed method based on a nonoveralapping domain decomposition procedure. **Mathematics and Computers in Simulation**, v. 99, p. 125–138, 2014. Citations on pages 34, 38, 39, 41, 47, and 51.

FU, S.; CHUNG, E. T. A local-global multiscale mortar mixed finite element method for multiphase transport in heterogeneous media. **Journal of Computational Physics**, Elsevier, v. 399, p. 108906, 2019. Citations on pages 37 and 38.

FURTADO, F.; GINTING, V.; PEREIRA, F.; PRESHO, M. Operator splitting multiscale finite volume element method for two-phase flow with capillary pressure. **Transport in Porous Media**, Springer, v. 90, n. 3, p. 927–947, 2011. Citation on page 34.

FURTADO, F.; PEREIRA, F. Crossover from nonlinearity controlled to heterogeneity controlled mixing in two-phase porous media flows. **Computational Geosciences**, Springer, v. 7, n. 2, p. 115–135, 2003. Citation on page 112.

GANIS, B.; JUNTUNEN, M.; PENCHEVA, G.; WHEELER, M. F.; YOTOV, I. A global Jacobian method for mortar discretizations of nonlinear porous media flows. **SIAM Journal on Scientific Computing**, SIAM, v. 36, n. 2, p. A522–A542, 2014. Citations on pages 37 and 38.

GANIS, B.; KUMAR, K.; PENCHEVA, G.; WHEELER, M. F.; YOTOV, I. A multiscale mortar method and two-stage preconditioner for multiphase flow using a global Jacobian approach. In: SOCIETY OF PETROLEUM ENGINEERS. **SPE Large Scale Computing and Big Data Challenges in Reservoir Simulation Conference and Exhibition**. Istanbul, Turkey, 2014. Citations on pages 37 and 38.

____. A global Jacobian method for mortar discretizations of a fully implicit two-phase flow model. **Multiscale Modeling & Simulation**, SIAM, v. 12, n. 4, p. 1401–1423, 2014. Citations on pages 34, 37, and 38.

GANIS, B.; PENCHEVA, G.; WHEELER, M. F.; WILDEY, T.; YOTOV, I. A frozen Jacobian multiscale mortar preconditioner for nonlinear interface operators. **Multiscale Modeling & Simulation**, SIAM, v. 10, n. 3, p. 853–873, 2012. Citations on pages 37 and 38.

GANIS, B.; VASSILEV, D.; WANG, C.; YOTOV, I. A multiscale flux basis for mortar mixed discretizations of Stokes–Darcy flows. **Computer Methods in Applied Mechanics and Engineering**, Elsevier, v. 313, p. 259–278, 2017. Citations on pages 37 and 38.

GANIS, B.; YOTOV, I. Implementation of a mortar mixed finite element method using a multiscale flux basis. **Computer Methods in Applied Mechanics and Engineering**, Elsevier, v. 198, n. 49-52, p. 3989–3998, 2009. Citations on pages 37, 38, and 41.

GLIMM, J.; MARCHESIN, D.; MCBRYAN, O. A numerical method for two phase flow with an unstable interface. **Journal of Computational Physics**, Elsevier, v. 39, n. 1, p. 179–200, 1981. Citation on page 112.

GOMES, A. T. A.; PEREIRA, W. S.; VALENTIN, F.; PAREDES, D. On the implementation of a scalable simulator for multiscale hybrid-mixed methods. **arXiv preprint arXiv:1703.10435**, 2017. Citations on pages 38 and 39.

GUIRALDELLO, R. T.; AUSAS, R. F.; SOUSA, F. S.; PEREIRA, F.; BUSCAGLIA, G. C. The multiscale Robin coupled method for flows in porous media. **Journal of Computational Physics**, Elsevier, v. 355, p. 1–21, 2018. Citations on pages 34, 38, 39, 41, 48, 49, 50, 56, 57, 78, and 90.

____. Interface spaces for the multiscale Robin coupled method in reservoir simulation. **Mathematics and Computers in Simulation**, Elsevier, v. 164, p. 103–119, 2019. Citations on pages 39, 41, 42, 49, 50, 56, 57, 58, 77, 78, and 90.

____. Velocity postprocessing schemes for multiscale mixed methods applied to contaminant transport in subsurface flows. **Computational Geosciences**, Springer, p. 1–21, 2020. Citations on pages 39, 51, 88, 109, and 123.

GULBRANSEN, A. F.; HAUGE, V. L.; LIE, K.-A. A multiscale mixed finite element method for vuggy and naturally fractured reservoirs. **SPE Journal**, Society of Petroleum Engineers, v. 15, n. 02, p. 395–403, 2010. Citation on page 41.

HAJIBEYGI, H.; KARVOUNIS, D.; JENNY, P. A hierarchical fracture model for the iterative multiscale finite volume method. **Journal of Computational Physics**, Elsevier, v. 230, n. 24, p. 8729–8743, 2011. Citation on page 78.

HARDER, C.; PAREDES, D.; VALENTIN, F. A family of multiscale hybrid-mixed finite element methods for the Darcy equation with rough coefficients. **Journal of Computational Physics**, v. 245, p. 107–130, 2013. Citations on pages 34, 37, 39, 41, and 48.

____. On a multiscale hybrid-mixed method for advective-reactive dominated problems with heterogeneous coefficients. **Multiscale Modeling & Simulation**, SIAM, v. 13, n. 2, p. 491–518, 2015. Citations on pages 37 and 39.

HARDER, C.; VALENTIN, F. Foundations of the MHM method. In: **Barrenechea G., Brezzi F., Cangiani A., Georgoulis E. (eds) Building Bridges: Connections and Challenges in Modern Approaches to Numerical Partial Differential Equations. Lecture Notes in Computational Science and Engineering**. Cham, Switzerland: Springer, 2016. v. 114. Citations on pages 37 and 39.

HOSSEINIMEHR, M.; KOBAISI, M. A.; VUIK, C.; HAJIBEYGI, H. Dynamic multilevel multiscale simulation of naturally fractured reservoirs with generic fracture-matrix conductivity contrasts. In: SOCIETY OF PETROLEUM ENGINEERS. **SPE Reservoir Characterisation and Simulation Conference and Exhibition**. Abu Dhabi, UAE, 2019. Citation on page 77.

HOTEIT, H.; FIROOZABADI, A. An efficient numerical model for incompressible two-phase flow in fractured media. **Advances in Water Resources**, Elsevier, v. 31, n. 6, p. 891–905, 2008. Citation on page 78.

HOU, T.; WU, X.-H. A multiscale finite element method for elliptic problems in composite materials and porous media. **Journal of Computational Physics**, v. 134, p. 169–189, 1997. Citations on pages 34 and 35.

HUANG, Z.-Q.; YAO, J.; WANG, Y.-Y. An efficient numerical model for immiscible two-phase flow in fractured karst reservoirs. **Communications in Computational Physics**, Cambridge University Press, v. 13, n. 2, p. 540–558, 2013. Citations on pages 42 and 78.

HUGHES, T. Multiscale phenomena: Green's functions, the Dirichlet-to-Neumann formulation, subgrid scale models, bubbles and the origins of stabilized methods. **Computer Methods in Applied Mechanics and Engineering**, v. 127, p. 387–401, 1995. Citation on page 40.

HUGHES, T. J.; FEIJÓO, G. R.; MAZZEI, L.; QUINCY, J.-B. The variational multiscale method - a paradigm for computational mechanics. **Computer Methods in Applied Mechanics and Engineering**, Elsevier, v. 166, n. 1-2, p. 3–24, 1998. Citation on page 40.

JENNY, P.; LEE, S.; TCHELEPI, H. A. Multi-scale finite-volume method for elliptic problems in subsurface flow simulation. **Journal of Computational Physics**, Elsevier, v. 187, n. 1, p. 47–67, 2003. Citations on pages 34, 51, 60, and 61.

JENNY, P.; LEE, S. H.; TCHELEPI, H. A. Adaptive multiscale finite-volume method for multiphase flow and transport in porous media. **Multiscale Modeling & Simulation**, v. 3, n. 1, p. 50–64, 2005. Citation on page 34.

____. Adaptive fully implicit multi-scale finite-volume method for multi-phase flow and transport in heterogeneous porous media. **Journal of Computational Physics**, Elsevier, v. 217, n. 2, p. 627–641, 2006. Citations on pages 34 and 128.

JENNY, P.; TCHELEPI, H. A.; LEE, S. H. Unconditionally convergent nonlinear solver for hyperbolic conservation laws with s-shaped flux functions. **Journal of Computational Physics**, Elsevier, v. 228, n. 20, p. 7497–7512, 2009. Citations on pages 115, 117, 120, and 121.

JIANG, J.; TCHELEPI, H. A. Nonlinear acceleration of sequential fully implicit (SFI) method for coupled flow and transport in porous media. **Computer Methods in Applied Mechanics and Engineering**, Elsevier, v. 352, p. 246–275, 2019. Citations on pages 34 and 128.

JIANG, L.; COPELAND, D.; MOULTON, J. D. Expanded mixed multiscale finite element methods and their applications for flows in porous media. **Multiscale Modeling & Simulation**, SIAM, v. 10, n. 2, p. 418–450, 2012. Citation on page 36.

JIANG, L.; EFENDIEV, Y.; MISHEV, I. Mixed multiscale finite element methods using approximate global information based on partial upscaling. **Computational Geosciences**, Springer, v. 14, n. 2, p. 319–341, 2010. Citations on pages 35 and 36.

JIANG, L.; LI, Q. Model's sparse representation based on reduced mixed GMsFE basis methods. **Journal of Computational Physics**, Elsevier, v. 338, p. 285–312, 2017. Citations on pages 40, 91, 94, and 95.

JIANG, L.; MISHEV, I.; LI, Y. Stochastic mixed multiscale finite element methods and their applications in random porous media. **Computer Methods in Applied Mechanics and Engineering**, Elsevier, v. 199, n. 41-44, p. 2721–2740, 2010. Citation on page 40.

JIANG, L.; MOULTON, J. D.; WEI, J. A hybrid HDMR for mixed multiscale finite element methods with application to flows in random porous media. **Multiscale Modeling & Simulation**, SIAM, v. 12, n. 1, p. 119–151, 2014. Citation on page 40.

JUANES, R.; DUB, F.-X. A locally conservative variational multiscale method for the simulation of porous media flow with multiscale source terms. **Computational Geosciences**, Springer, v. 12, n. 3, p. 273–295, 2008. Citation on page 40.

KARIMI-FARD, M.; DURLOFSKY, L. J.; AZIZ, K. An efficient discrete fracture model applicable for general purpose reservoir simulators. In: SOCIETY OF PETROLEUM ENGINEERS. **SPE Reservoir Simulation Symposium**. Houston, TX, EUA, 2003. Citation on page 78.

KIM, J.-G.; DEO, M. D. Finite element, discrete-fracture model for multiphase flow in porous media. **AIChE Journal**, Wiley Online Library, v. 46, n. 6, p. 1120–1130, 2000. Citation on page 78.

KIM, M.-Y.; PARK, E.-J.; THOMAS, S. G.; WHEELER, M. F. A multiscale mortar mixed finite element method for slightly compressible flows in porous media. **Journal of the Korean Mathematical Society**, The Korean Mathematical Society, v. 44, n. 5, p. 1103–1119, 2007. Citations on pages 37 and 38.

KIPPE, V.; AARNES, J.; LIE, K. A comparison of multiscale methods for elliptic problems in porous media flow. **Computational Geosciences**, v. 12, n. 3, p. 377–398, 2008. Citations on pages 34 and 58.

KLEMETSDAL, Ø. S.; MØYNER, O.; LIE, K.-A. Accelerating multiscale simulation of complex geomodels by use of dynamically adapted basis functions. **Computational Geosciences**, Springer, p. 1–18, 2019. Citation on page 77.

KROGSTAD, S. A sparse basis POD for model reduction of multiphase compressible flow. In: SOCIETY OF PETROLEUM ENGINEERS. **SPE Reservoir Simulation Symposium**. The Woodlands, TX, USA, 2011. Citations on pages 35 and 36.

KROGSTAD, S.; DURLOFSKY, L. J. Multiscale mixed-finite-element modeling of coupled wellbore/near-well flow. In: SOCIETY OF PETROLEUM ENGINEERS. **SPE Reservoir Simulation Symposium**. Houston, TX, EUA, 2007. Citations on pages 35 and 36.

KROGSTAD, S.; HAUGE, V. L.; GULBRANSEN, A. Adjoint multiscale mixed finite elements. **SPE Journal**, Society of Petroleum Engineers, v. 16, n. 01, p. 162–171, 2011. Citations on pages 35 and 36.

KROGSTAD, S.; LIE, K.; SKAFLESTAD, B. Mixed multiscale methods for compressible flow. In: EUROPEAN ASSOCIATION OF GEOSCIENTISTS & ENGINEERS. **Proceedings of ECMOR XIII–13th European Conference on the Mathematics of Oil Recovery**. Biarritz, France, 2012. Citations on pages 35 and 36.

KROGSTAD, S.; LIE, K.-A.; NILSEN, H. M.; NATVIG, J. R.; SKAFLESTAD, B.; AARNES, J. E. A multiscale mixed finite element solver for three phase black oil flow. In: SOCIETY OF PETROLEUM ENGINEERS. **SPE Reservoir Simulation Symposium**. The Woodlands, TX, EUA, 2009. Citations on pages 35 and 36.

KURGANOV, A.; TADMOR, E. New high-resolution central schemes for nonlinear conservation laws and convection–diffusion equations. **Journal of Computational Physics**, Elsevier, v. 160, n. 1, p. 241–282, 2000. Citation on page 52.

LARSON, M. G.; MÅLQVIST, A. A mixed adaptive variational multiscale method with applications in oil reservoir simulation. **Mathematical Models and Methods in Applied Sciences**, World Scientific, v. 19, n. 07, p. 1017–1042, 2009. Citation on page 40.

LEVEQUE, R. J. **Finite volume methods for hyperbolic problems**. Cambridge, UK: Cambridge University Press, 2002. Citations on pages 52 and 57.

LI, B.; TCHELEPI, H. A. Nonlinear analysis of multiphase transport in porous media in the presence of viscous, buoyancy, and capillary forces. **Journal of Computational Physics**, Elsevier, v. 297, p. 104–131, 2015. Citation on page 117.

LI, L.; LEE, S. H. Efficient field-scale simulation of black oil in a naturally fractured reservoir through discrete fracture networks and homogenized media. **SPE Reservoir Evaluation & Engineering**, Society of Petroleum Engineers, v. 11, n. 04, p. 750–758, 2008. Citation on page 78.

LIE, K.-A. **An introduction to reservoir simulation using MATLAB/GNU Octave: User guide for the MATLAB Reservoir Simulation Toolbox (MRST)**. Cambridge, UK: Cambridge University Press, 2019. Citations on pages 33, 147, and 148.

LIE, K.-A.; NATVIG, J. R.; KROGSTAD, S.; YANG, Y.; WU, X.-H. Grid adaptation for the Dirichlet–Neumann representation method and the multiscale mixed finite-element method. **Computational Geosciences**, Springer, v. 18, n. 3-4, p. 357–372, 2014. Citation on page 36.

LOPES, T. V.; ROCHA, A. C.; MURAD, M. A.; GARCIA, E. L.; PEREIRA, P. A.; CAZARIN, C. L. A new computational model for flow in karst-carbonates containing solution-collapse breccias. **Computational Geosciences**, Springer, p. 1–27, 2019. Citations on pages 42 and 78.

LUNATI, I.; LEE, S. H. An operator formulation of the multiscale finite-volume method with correction function. **Multiscale Modeling & Simulation**, SIAM, v. 8, n. 1, p. 96–109, 2009. Citations on pages 60 and 61.

MA, X.; ZABARAS, N. A stochastic mixed finite element heterogeneous multiscale method for flow in porous media. **Journal of Computational Physics**, Elsevier, v. 230, n. 12, p. 4696–4722, 2011. Citation on page 40.

MADUREIRA, A. L. Abstract multiscale-hybrid-mixed methods. **Calcolo**, Springer, v. 52, n. 4, p. 543–557, 2015. Citations on pages 37 and 39.

MADUREIRA, A. L.; SARKIS, M. Hybrid localized spectral decomposition for multiscale problems. **arXiv preprint arXiv:1706.08941**, 2017. Citation on page 77.

MÅLQVIST, A. Multiscale methods for elliptic problems. **Multiscale Modeling & Simulation**, SIAM, v. 9, n. 3, p. 1064–1086, 2011. Citation on page 40.

MÅLQVIST, A.; PETERSEIM, D. Localization of elliptic multiscale problems. **Mathematics of Computation**, v. 83, n. 290, p. 2583–2603, 2014. Citation on page 40.

MANKAD, H. Y. **The Multiscale Perturbation Method for Two-Phase Flows**. Phd Thesis (PhD Thesis) — The University of Texas at Dallas, Dallas, TX, USA, 2020. Citations on pages 105 and 108.

MARTIN, V.; JAFFRÉ, J.; ROBERTS, J. E. Modeling fractures and barriers as interfaces for flow in porous media. **SIAM Journal on Scientific Computing**, SIAM, v. 26, n. 5, p. 1667–1691, 2005. Citation on page 78.

MEACCI, L.; ROCHA, F. F.; SILVA, A. A.; PRAMIU, P. V.; BUSCAGLIA, G. C. Planejamento de trajetória para a manipulação de partículas em microfluídica. **C.Q.D. - Revista Eletrônica Paulista de Matemática (Bauru)**, C.Q.D., v. 10, p. 19–37, 2017. Citation on page 131.

____. A trajectory planning model for the manipulation of particles in microfluidics. **TEMA (São Carlos)**, SciELO Brasil, v. 19, n. 3, p. 509–523, 2018. Citation on page 131.

MØYNER, O.; LIE, K.-A. A multiscale restriction-smoothed basis method for high contrast porous media represented on unstructured grids. **Journal of Computational Physics**, Elsevier, v. 304, p. 46–71, 2016. Citations on pages 34, 42, and 77.

NAKSHATRALA, K.; TURNER, D.; HJELMSTAD, K.; MASUD, A. A stabilized mixed finite element method for Darcy flow based on a multiscale decomposition of the solution. **Computer Methods in Applied Mechanics and Engineering**, Elsevier, v. 195, n. 33-36, p. 4036–4049, 2006. Citation on page 40.

NATVIG, J. R.; SKAFLESTAD, B.; BRATVEDT, F.; BRATVEDT, K.; LIE, K.-A.; LAPTEV, V.; KHATANIAR, S. Multiscale mimetic solvers for efficient streamline simulation of fractured reservoirs. **SPE Journal**, Society of Petroleum Engineers, v. 16, n. 04, p. 880–888, 2011. Citation on page 41.

NOCEDAL, J.; WRIGHT, S. **Numerical optimization**. 2. ed. New York, NY, USA: Springer Science & Business Media, 2006. Citations on pages 119 and 120.

OVAYSI, S.; WHEELER, M. F.; BALHOFF, M. Quantifying the representative size in porous media. **Transport in porous media**, Springer, v. 104, n. 2, p. 349–362, 2014. Citation on page 148.

PAL, M.; LAMINE, S.; LIE, K.-A.; KROGSTAD, S. Validation of the multiscale mixed finite-element method. **International Journal for Numerical Methods in Fluids**, Wiley Online Library, v. 77, n. 4, p. 206–223, 2015. Citation on page 36.

PAREDES, D.; VALENTIN, F.; VERSIEUX, H. On the robustness of multiscale hybrid-mixed methods. **Mathematics of Computation**, v. 86, n. 304, p. 525–548, 2017. Citations on pages 38 and 39.

PAZ, S.; JARAMILLO, A.; GUIRALDELLO, R. T.; AUSAS, R. F.; SOUSA, F. S.; PEREIRA, F.; BUSCAGLIA, G. C. An adaptive time stepping algorithm for IMPES with high order polynomial extrapolation. **Submitted**, 2020. Citation on page 132.

PEACEMAN, D. W. **Fundamentals of numerical reservoir simulation**. Amsterdam, Netherlands: Elsevier, 2000. Citation on page 34.

PENCHEVA, G. V.; VOHRALÍK, M.; WHEELER, M. F.; WILDEY, T. Robust a posteriori error control and adaptivity for multiscale, multinumerics, and mortar coupling. **SIAM Journal on Numerical Analysis**, SIAM, v. 51, n. 1, p. 526–554, 2013. Citations on pages 37 and 38.

PESZYŃSKA, M.; WHEELER, M. F.; YOTOV, I. Mortar upscaling for multiphase flow in porous media. **Computational Geosciences**, Springer, v. 6, n. 1, p. 73–100, 2002. Citation on page 77.

POPOV, P.; QIN, G.; BI, L.; EFENDIEV, Y.; KANG, Z.; LI, J. Multiphysics and multiscale methods for modeling fluid flow through naturally fractured carbonate karst reservoirs. **SPE Reservoir Evaluation & Engineering**, Society of Petroleum Engineers, v. 12, n. 02, p. 218–231, 2009. Citations on pages 42 and 78.

POWELL, M. J. **A Fortran subroutine for solving systems of nonlinear algebraic equations**. [S.l.], 1968. Citation on page 120.

PRESHO, M.; GALVIS, J. A mass conservative generalized multiscale finite element method applied to two-phase flow in heterogeneous porous media. **Journal of Computational and Applied Mathematics**, Elsevier, v. 296, p. 376–388, 2016. Citation on page 34.

PRESHO, M.; HILL, M. A conservative generalized multiscale finite volume/element method for modeling two-phase flow with capillary pressure. **Journal of Computational and Applied Mathematics**, Elsevier, p. 113026, 2020. Citation on page 34.

PUSCAS, M. A.; ENCHÉRY, G.; DESROZIERS, S. Application of the mixed multiscale finite element method to parallel simulations of two-phase flows in porous media. **Oil & Gas Science and Technology–Revue d'IFP Energies nouvelles**, EDP Sciences, v. 73, p. 38, 2018. Citation on page 36.

REICHENBERGER, V.; JAKOBS, H.; BASTIAN, P.; HELMIG, R. A mixed-dimensional finite volume method for two-phase flow in fractured porous media. **Advances in Water Resources**, Elsevier, v. 29, n. 7, p. 1020–1036, 2006. Citation on page 78.

ROCHA, F. F.; PIRES, V. A.; SOUSA, F. S. de; BUSCAGLIA, G. C. Precisão de métodos de volumes finitos para a solução da equação de Buckley-Leverett. In: SBMAC. **Proceeding Series of the Brazilian Society of Computational and Applied Mathematics–XXXVIII CNMAC**. Campinas, SP, Brazil, 2018. v. 6, n. 2, p. 1–7. Citation on page 131.

ROCHA, F. F.; SOUSA, F. S.; AUSAS, R. F.; PEREIRA, F.; BUSCAGLIA, G. C. Interface spaces based on physics for multiscale mixed methods applied to flows in channelized porous media. **Submitted**, 2020. Citations on pages 39, 42, 131, and 132.

ROCHA, F. F.; SOUSA, F. S.; AUSAS, R. F.; BUSCAGLIA, G. C.; PEREIRA, F. Multiscale mixed methods for two-phase flows in high-contrast porous media. **Journal of Computational Physics**, Elsevier, p. 109316, 2020. Citations on pages 39, 41, 55, 90, 123, 130, and 132.

RUSANOV, V. V. The calculation of the interaction of non-stationary shock waves and obstacles. **USSR Computational Mathematics and Mathematical Physics**, Elsevier, v. 1, n. 2, p. 304–320, 1962. Citation on page 53.

SCHWENCK, N.; FLEMISCH, B.; HELMIG, R.; WOHLMUTH, B. I. Dimensionally reduced flow models in fractured porous media: crossings and boundaries. **Computational Geosciences**, Springer, v. 19, n. 6, p. 1219–1230, 2015. Citation on page 78.

SINGH, G.; LEUNG, W.; WHEELER, M. F. Multiscale methods for model order reduction of non-linear multiphase flow problems. **Computational Geosciences**, Springer, v. 23, n. 2, p. 305–323, 2019. Citations on pages 40 and 41.

SONG, X.; JIANG, L.; ZHENG, G.-H. Implicit sampling for hierarchical Bayesian inversion and applications in fractional multiscale diffusion models. **Journal of Computational and Applied Mathematics**, Elsevier, p. 112826, 2020. Citations on pages 40 and 41.

SPIRIDONOV, D.; HUANG, J.; VASILYEVA, M.; HUANG, Y.; CHUNG, E. T. Mixed generalized multiscale finite element method for Darcy-Forchheimer model. **Mathematics**, Multidisciplinary Digital Publishing Institute, v. 7, n. 12, p. 1212, 2019. Citations on pages 40 and 41.

SPIRIDONOV, D.; VASILYEVA, M. Multiscale model reduction of the flow problem in fractured porous media using mixed generalized multiscale finite element method. In: AIP PUBLISHING LLC. **AIP Conference Proceedings**. Albena, Bulgaria, 2018. v. 2025, n. 1, p. 100008. Citation on page 41.

TENE, M.; KOBAISI, M. S. A.; HAJIBEYGI, H. Algebraic multiscale method for flow in heterogeneous porous media with embedded discrete fractures (F-AMS). **Journal of Computational Physics**, Elsevier, v. 321, p. 819–845, 2016. Citation on page 78.

WANG, M.; CHEUNG, S. W.; CHUNG, E. T.; VASILYEVA, M.; WANG, Y. Generalized multiscale multicontinuum model for fractured vuggy carbonate reservoirs. **Journal of Computational and Applied Mathematics**, Elsevier, v. 366, p. 112370, 2020. Citation on page 78.

WANG, X.; TCHELEPI, H. A. Trust-region based solver for nonlinear transport in heterogeneous porous media. **Journal of Computational Physics**, Elsevier, v. 253, p. 114–137, 2013. Citations on pages 115, 117, and 119.

WANG, Y.; HAJIBEYGI, H.; TCHELEPI, H. A. Monotone multiscale finite volume method. **Computational Geosciences**, Springer, v. 20, n. 3, p. 509–524, 2016. Citation on page 34.

WATTS, J. W. A compositional formulation of the pressure and saturation equations. **SPE Reservoir Engineering**, Society of Petroleum Engineers, v. 1, n. 03, p. 243–252, 1986. Citations on pages 43 and 115.

WEI, J.; LIN, G.; JIANG, L.; EFENDIEV, Y. Analysis of variance-based mixed multiscale finite element method and applications in stochastic two-phase flows. **International Journal for Uncertainty Quantification**, Begel House Inc., v. 4, n. 6, 2014. Citation on page 40.

WHEELER, M. F.; WILDEY, T.; YOTOV, I. A multiscale preconditioner for stochastic mortar mixed finite elements. **Computer Methods in Applied Mechanics and Engineering**, Elsevier, v. 200, n. 9-12, p. 1251–1262, 2011. Citation on page 40.

WHEELER, M. F.; XUE, G.; YOTOV, I. A multiscale mortar multipoint flux mixed finite element method. **ESAIM: Mathematical Modelling and Numerical Analysis**, EDP Sciences, v. 46, n. 4, p. 759–796, 2012. Citations on pages 37 and 38.

XIA, Y.; JIN, Y.; CHEN, M.; CHEN, K. P. An enriched approach for modeling multiscale discrete-fracture/matrix interaction for unconventional-reservoir simulations. **SPE Journal**, Society of Petroleum Engineers, 2018. Citation on page 78.

XIE, H.; XU, X. Domain decomposition preconditioners for mixed finite-element discretization of high-contrast elliptic problems. **Communications on Applied Mathematics and Computation**, Springer, v. 1, n. 1, p. 141–165, 2019. Citation on page 40.

YANG, Y.; CHUNG, E. T.; FU, S. Residual driven online mortar mixed finite element methods and applications. **Journal of Computational and Applied Mathematics**, Elsevier, v. 340, p. 318–333, 2018. Citations on pages 40 and 41.

YANG, Y.; FU, S.; CHUNG, E. T. A two-grid preconditioner with an adaptive coarse space for flow simulations in highly heterogeneous media. **Journal of Computational Physics**, Elsevier, v. 391, p. 1–13, 2019. Citations on pages 40 and 41.

____. Online mixed multiscale finite element method with oversampling and its applications. **Journal of Scientific Computing**, Springer, v. 82, n. 2, p. 31, 2020. Citations on pages 40 and 41.

YUAN, Y.-X. Recent advances in trust region algorithms. **Mathematical Programming**, Springer, v. 151, n. 1, p. 249–281, 2015. Citation on page 119.

ZHANG, N.; YAN, B.; SUN, Q.; WANG, Y. Improving multiscale mixed finite element method for flow simulation in highly heterogeneous reservoir using adaptivity. **Journal of Petroleum Science and Engineering**, Elsevier, v. 154, p. 382–388, 2017. Citation on page 36.

ZHANG, N.; YAO, J.; XUE, S.; HUANG, Z. Multiscale mixed finite element, discrete fracture–vug model for fluid flow in fractured vuggy porous media. **International Journal of Heat and Mass Transfer**, Elsevier, v. 96, p. 396–405, 2016. Citation on page 41.

ZHANG, N.; ZENG, W.; WANG, Y.; SUN, Q. Beyond multiple-continuum modeling for the simulation of complex flow mechanisms in multiscale shale porous media. **Journal of Computational and Applied Mathematics**, Elsevier, p. 112854, 2020. Citation on page 36.

ZHANG, Q.; HUANG, Z.; YAO, J.; WANG, Y.; LI, Y. A multiscale mixed finite element method with oversampling for modeling flow in fractured reservoirs using discrete fracture model. **Journal of Computational and Applied Mathematics**, Elsevier, v. 323, p. 95–110, 2017. Citations on pages 41 and 78.

APPENDIX

A

EQUATIONS FOR FLOWS IN POROUS MEDIA

Flows in porous media are induced by pressure or flux imposition at the boundaries of the domain that contains the fluid. The fundamental principles that describe this type of flows reflect the conservation of fluid mass, the relation between pressure and velocity (given by the Darcy's law), and the transport for the saturation of the fluids. In the next subsections, we present the model problem for single and two-phase flows.

A.1 Single-phase flows

The relation between pressure and velocity of a phase in a porous medium is described by Darcy's law, established experimentally by Henry Darcy in 1856 (AZIZ; SETTARI, 1979) as follows:

$$\mathbf{u} = -\frac{K}{\mu}(\nabla p - \rho \mathscr{G} \nabla Z), \tag{A.1}$$

where $\mathbf{u} = \mathbf{u}(\mathbf{x})$ is the velocity of the phase; $p = p(\mathbf{x})$ is the pressure of the phase; $K = K(\mathbf{x})$ is the absolute permeability of the medium; μ is the viscosity of the phase; $\rho(\mathbf{x})$ is the density of the phase; $\mathscr{G}$ is the magnitude of the acceleration due to gravity; and $Z = Z(\mathbf{x})$ is the depth vector pointing in the direction of gravity.

The permeability represents the heterogeneity of the medium. It can be interpreted as the ability of the porous medium to transmit a fluid when the empty spaces are filled by it (LIE, 2019). Reservoirs with very connected pores, where the fluid is easily transmitted are considered highly-permeable. The absolute permeability K is a symmetric, uniformly positive definite tensor (EWING, 1983). By assuming that it is a diagonal tensor or it can be diagonalized, we have

$$K = \begin{bmatrix} k_x & 0 & 0 \\ 0 & k_y & 0 \\ 0 & 0 & k_z \end{bmatrix}, \tag{A.2}$$

where k_x, k_y, and k_z are the permeability values in the directions x, y, and z, respectively. It means, for example, that k_x represents the flow in x direction caused by a change in pressure in x direction. When $k_x = k_y = k_z$, the medium is called isotropic, i.e., its physical properties are independent on the direction considered, otherwise the medium is called anisotropic.

The velocity in equation (A.1) is studied in Darcy's scale (typically between 10^{-2} and 10^{1} meters) and considers an average of the flux within the Representative Elementary Volumes (REVs). The REVs are volumes where the petrophysical properties can be considered constant, which are usually between the scale of the pores of the rock (from 10^{-6} to 10^{-3} meters) and the Darcy scale (OVAYSI; WHEELER; BALHOFF, 2014). In Figure 65, a representation of a REV is shown, considering the porosity (fraction of the volume available for flow), that is equal to one at the pores and zero at the rock (LIE, 2019). Figure 66 illustrates the Darcy velocity in a REV.

Figure 65 – Representation of a REV, taking into account the porosity. The REV is defined when the porosity presents low variations, and hence, it can be considered constant.

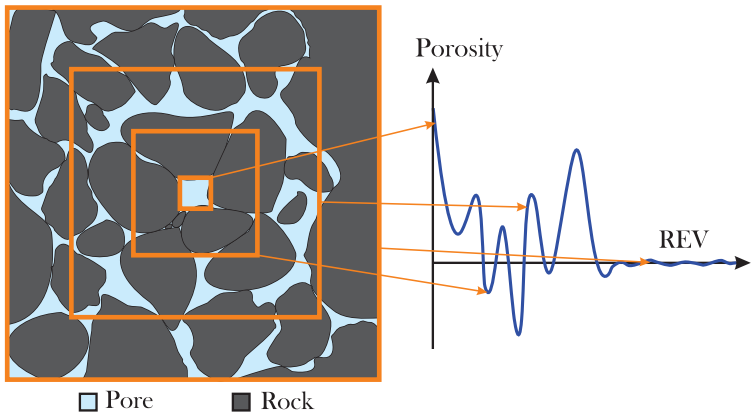

Source: Adapted from Lie (2019).

Figure 66 – Representation of the Darcy velocity in a REV, that is an average of the flux within the REV.

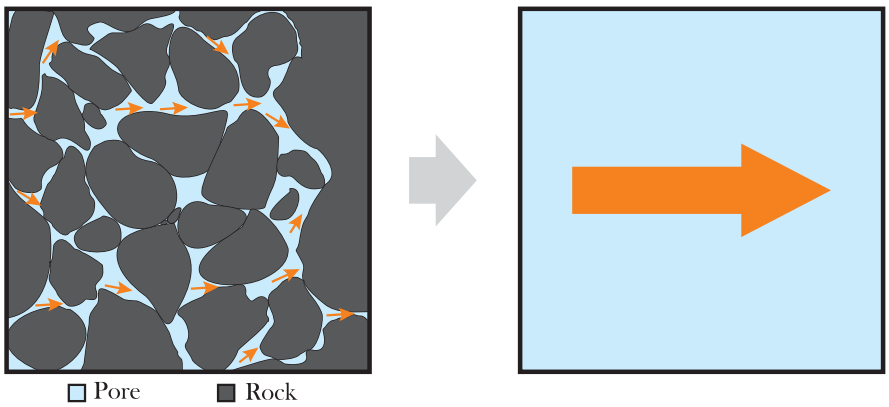

Source: Lie (2019).

To derive the flow equations, we consider the conservation of mass for a REV (denoted

by V), given by

$$\frac{\partial}{\partial t}\int_V \phi\rho(\mathbf{x},t)\,d\mathbf{x}+\int_{\partial V}\rho(\mathbf{x},t)\mathbf{u}\cdot\mathbf{n}\,dS=\int_V \tilde{q}\,d\mathbf{x}, \tag{A.3}$$

where ϕ is the porosity, ∂V is the boundary of V with the outward unit normal $\mathbf{n}$, and $\tilde{q}$ is the mass flow rate injected into V (EWING, 1983). By applying the divergence theorem in Eq. (A.3) we obtain

$$\frac{\partial}{\partial t}\int_V \phi\rho\,d\mathbf{x}+\int_V \nabla\cdot(\rho\mathbf{u})d\mathbf{x}=\int_V \tilde{q}\,d\mathbf{x}, \tag{A.4}$$

that can be written as

$$\int_V\left(\frac{\partial}{\partial t}(\phi\rho)+\nabla\cdot(\rho\mathbf{u})\right)d\mathbf{x}=\int_V \tilde{q}\,d\mathbf{x}. \tag{A.5}$$

Equation (A.5) must hold for any volume element V, and hence, we find the partial differential equation

$$\frac{\partial}{\partial t}(\phi\rho)+\nabla\cdot(\rho\mathbf{u})=\tilde{q}. \tag{A.6}$$

By using Eq. (A.1) in Eq. (A.6) we get

$$\frac{\partial}{\partial t}(\phi\rho)-\nabla\cdot\left(\frac{\rho K}{\mu}(\nabla p-\rho\mathscr{G}\nabla Z)\right)=\tilde{q}. \tag{A.7}$$

We consider an incompressible, isothermal flow, without gravitational effects. The phase considered has constant density, and the porous medium is incompressible. Therefore, Eq. (A.7) can be simplified to

$$-\nabla\cdot\left(\frac{K}{\mu}\nabla p\right)=\frac{\tilde{q}}{\rho}. \tag{A.8}$$

Finally, the elliptic model equation for single-phase flows that we consider is given by

$$\nabla\cdot\mathbf{u}=q,\qquad \mathbf{u}=-\lambda K\nabla p, \tag{A.9}$$

where $q=\tilde{q}/\rho$ and $\lambda=1/\mu$. To complete the mathematical model, boundary data for pressure or normal fluxes are required.

A.2 Two-phase flows

Our model for two-phase flows considers an immiscible flow of water and oil (denoted by w and o, respectively). The new unknowns, the saturations $s_j\in[0,1]$ of each phase $j\in\{w,o\}$, are the fractions of the domain that are occupied, respectively, by each phase j. We consider a fully saturated medium, i.e. $s_w+s_o=1$. The conservation of mass for each phase is given by

$$\frac{\partial}{\partial t}(\phi\rho_j s_j)+\nabla\cdot(\rho_j\mathbf{u}_j)=\tilde{q}_j,\qquad j\in\{w,o\}, \tag{A.10}$$

while the Darcy's law for each phase is given by

$$\mathbf{u}_j=-\lambda_j K(\nabla p_j-\rho_j\mathscr{G}\nabla Z), \tag{A.11}$$

where $\lambda_j = k_{rj}/\mu_j$ is the mobility of phase j, and k_{rj} is the given relative permeability function of phase j (EWING, 1983).

We consider an incompressible, isothermal flow, without gravitational effects. The densities of each phase are constant, and the porous medium is incompressible. Furthermore, we neglect the effects of capillary pressure, and hence, the global pressure is given by $p = p_w = p_o$. The Darcy's law in Eq. (A.11) can be simplified to

$$\mathbf{u} = -\lambda K \nabla p, \tag{A.12}$$

where $\mathbf{u} = \mathbf{u}_w + \mathbf{u}_o$ and $\lambda = \lambda_w + \lambda_o$. Thus, the elliptic model equation corresponding to two-phase flows is given by

$$\nabla \cdot \mathbf{u} = q, \qquad \mathbf{u} = -\lambda K \nabla p, \tag{A.13}$$

where $q = \dfrac{\tilde{q}_w}{\rho_w} + \dfrac{\tilde{q}_o}{\rho_o}$. By introducing the fractional flow of water function

$$f(s_w) = \frac{\lambda_w(s_w)}{\lambda(s_w)}, \tag{A.14}$$

we can rewrite Eq. (A.10) for the water saturation as

$$\phi \frac{\partial s_w}{\partial t} + \nabla \cdot (f(s_w)\mathbf{u}) = \frac{\tilde{q}_w}{\rho_w}. \tag{A.15}$$

The source term of Eq. (A.15) usually takes into account injection and production wells and can be converted into a suitable boundary condition (EWING, 1983). Thus, we finally get the following hyperbolic equation

$$\phi \frac{\partial s}{\partial t} + \nabla \cdot (f(s)\mathbf{u}) = 0, \tag{A.16}$$

where $s = s_w$. The model for two-phase flows that we consider is given by the coupling of Eq. (A.13) and Eq. (A.16), along with initial and injection conditions for saturation, and boundary data for pressure or normal fluxes.


ICMC
USP
SÃO CARLOS